TKK Dissertations 106
Espoo 2008

INHOMOGENEOUS COMPRESSION OF PEMFC GAS DIFFUSION LAYERS

Doctoral Dissertation

Iwao Nitta

Helsinki University of Technology
Faculty of Information and Natural Sciences
Department of Engineering Physics

TKK Dissertations 106
Espoo 2008

INHOMOGENEOUS COMPRESSION OF PEMFC GAS DIFFUSION LAYERS

Doctoral Dissertation

Iwao Nitta

Dissertation for the degree of Doctor of Science in Technology to be presented with due permission of the Faculty of Information and Natural Sciences for public examination and debate in Auditorium AS1 at Helsinki University of Technology (Espoo, Finland) on the 14th of March, 2008, at 12 noon.

Helsinki University of Technology
Faculty of Information and Natural Sciences
Department of Engineering Physics

Teknillinen korkeakoulu
Informaatio- ja luonnontieteiden tiedekunta
Teknillisen fysiikan laitos

Distribution:
Helsinki University of Technology
Faculty of Information and Natural Sciences
Department of Engineering Physics
P.O. Box 4100
FI - 02015 TKK
FINLAND
URL: http://www.tkk.fi/Units/AES/
Tel. +358-9-451 3198
Fax +358-9-451 3195
E-mail: iwao.nitta@tkk.fi

ISBN 978-951-22-9232-5
ISBN 978-951-22-9233-2 (PDF)
ISSN 1795-2239
ISSN 1795-4584 (PDF)
URL: http://lib.tkk.fi/Diss/2008/isbn9789512292332/

TKK-DISS-2432

Multiprint Oy
Espoo 2008

Preface

The doctoral work presented in this thesis was carried out between 2005 and 2008 at the Laboratory of Advanced Energy Systems, Helsinki University of Technology.

I firstly would like to express my deep and sincere gratitude to my supervisor, Professor Peter Lund for giving me this great opportunity to work on this fascinating subject in pleasant environment. D.Sc. Pertti Kauranen and Ph.D. Jari Ihonen deserve my appreciation for taking their precious time to act as pre-examiners for my thesis. Their comments, suggestions and corrections helped improve the quality of this work.

My co-workers in the fuel cell group, D.Sc. Mikko Mikkola, Ms. Suvi Karvonen, Ms. Sonja Jokimies and Ms. Saara Tuurala, and former co-workers D.Sc. Olli Himanen, D.Sc. Matti Noponen, D.Sc. Tero Hottinen, Mr. Jaakko Saarinen and Mr. Timo Lehtinen constantly gave me valuable advice related to the work and made my life in Finland more joyful. I can not find any words to express my thanks to you all. I am really glad that I have come to get to know you in my life.

I would also like to thank professor Maarit Karppinen at Laboratory of Inorganic and Analytical Chemistry, Helsinki University of Technology and professor Hisao Yamaguchi at Materials and Structures Laboratory, Tokyo Institute of Technology for introducing this great university to me and encouraging me to study abroad. I would also like to thank my supervisors in Japan, professor Yoshitaka Kitamoto and professor Yohtaro Yamazaki, Mr. Yohichi Matsuo and Mr. Yasuto Honma, who ignited my interest in science and my curiosity of exploring new worlds, and gave me invaluable advice not only on scientific research but also on life in general.

Finally special thanks to my parents for all their support that has kept me going.

The main financing for the work was provided by Fortumin Säätiö (Fortum Foundation) and the Center of International Mobility (CIMO). I would also like to thank the Scandinavia-Japan Sasakawa Foundation and the Finnish Funding Agency for Technology and Innovation.

Espoo, March 2008

Iwao Takemori Nitta

ABSTRACT OF DOCTORAL DISSERTATION	HELSINKI UNIVERSITY OF TECHNOLOGY P.O. BOX 1000, FI-02015 TKK http://www.tkk.fi

Author Iwao Nitta

Name of the dissertation	Inhomogeneous Compression of PEMFC Gas Diffusion Layers		
Manuscript submitted	11.12.2007	Manuscript revised	6.2.2008
Date of the defense	14.3.2008		
☐ Monograph		☒ Article dissertation (summary + original articles)	
Department	Engineering Physics and Mathematics		
Laboratory	Advanced Energy Systems		
Field of research	Fuel cells		
Opponent(s)	Professor Jon Pharoah		
Supervisor	Professor Peter Lund		
Instructor	D.Sc. Mikko Mikkola		

Abstract

Proton exchange membrane fuel cells (PEMFCs) are electrochemical devices which convert the chemical energy of reactants directly into electrical energy. This technology enables high efficiency and high energy density compared to internal combustion engines and current batteries, thereby making the technology attractive for broad range of applications. Furthermore, the only exhaust from PEMFCs is water, which makes them favorable from the environmental point of view.

Gas diffusion layer (GDL) is one of the most important components in a fuel cell, whose functions cover a wide range of operations: to provide a passage for reactant access and product water removal, to conduct electricity and heat between adjacent components, and to provide mechanical support for the MEA. The properties of GDL are strongly dependent on compression pressure. Of particular importance is the fact that the compression pressure on GDL is inhomogeneous because of the rib/channel structure of bipolar plate. However, previous theoretical studies have typically neglected this effect, and thus they inherently contained errors in the modeled results. Therefore, the aim of this study is to obtain insight into the actual effects of the inhomogeneous compression of GDL using experimental and theoretical approaches.

The experimentally evaluated properties are GDL mechanical properties, gas permeability, in-plane and through-plane electric conductivities, electric contact resistances between fuel cell components, thermal bulk conductivity and thermal contact resistance. All parameters are evaluated as a function of compressed GDL thickness. It was found that compression increases electric GDL conductivities but does not affect the thermal conductivity. Both electric and thermal contact resistances and gas permeability are decreased nonlinearly by the compression.

The modeling study was performed by applying the experimentally evaluated parameters for the systematic investigation of the effect of inhomogeneous compression. It was found that the inhomogeneous compression does not significantly affect the polarization behavior and gas-phase mass transport. However, the effects on the current density distribution were evident. This was caused by the changes in the selective current path, which is determined by the combinations of conductivities of components and contact resistance between them. Despite the highly uneven current distribution and variation in material parameters by the inhomogeneous compression, the temperature profile was fairly even over the active area, contrary to the predictions in previous studies.

This study suggests that high current density distribution caused by the inhomogeneous compression of GDL has a significant effect on the local cell performance and cell durability. The insight obtained from this study is highly beneficial for development and construction of fuel cells, as well as predicting their performance and life time.

Keywords PEMFC, gas diffusion layer, inhomogeneous compression, mathematical modeling, contact resistance, conductivity

ISBN (printed)	978-951-22-9232-5	ISSN (printed)	1795-2239
ISBN (pdf)	978-951-22-9233-2	ISSN (pdf)	1795-4584
Language	English	Number of pages	88 + app. 81

Publisher Department of Engineering Physics, Helsinki University of Technology

Print distribution Laboratory of Advanced Energy Systems, P.O. Box 4100, 02015 TKK, Finland

☒ The dissertation can be read at http://lib.tkk.fi/Diss/2008/isbn9789512292332/

Table of Contents

List of publications and author's contribution

[I] I. Nitta, T. Hottinen, O. Himanen, M. Mikkola, J. Power Sources 171 (2007) 26–36. *Inhomogeneous compression of PEMFC gas diffusion layer: Part I. Experimental*

[II] T. Hottinen, O. Himanen, S. Karvonen, I. Nitta, J. Power Sources 171 (2007) 113–121. *Inhomogeneous compression of PEMFC gas diffusion layer: Part II. Modeling the effect*

[III] I. Nitta, O. Himanen, M. Mikkola, Electrochem. Commun. 10 (2008) 47–51. *Contact resistance between gas diffusion layer and catalyst layer of PEM fuel cell*

[IV] I. Nitta, O. Himanen, M. Mikkola, TKK, Otaniemi, Finland, February 2008. 20 p. Helsinki University of Technology Publications in Engineering Physics TKK-F-A853. ISBN 978-951-22-9215-8 (print) 978-951-22-9216-5 (electronic). (Fuel Cells, submitted for publication, 4th October, 2007.) *Thermal conductivity and contact resistance of compressed gas diffusion layer of PEM fuel cell*

[V] I. Nitta, S. Karvonen, O. Himanen, M. Mikkola, TKK, Otaniemi, Finland, February 2008. 23 p. Helsinki University of Technology Publications in Engineering Physics TKK-F-A854. ISBN 978-951-22-9217-2 (print) 978-951-22-9218-9 (electronic). (Fuel Cells, submitted for publication, 8th November, 2007.) *Modeling the Effect of Inhomogeneous Compression of GDL on Local Transport Phenomena in a PEM Fuel Cell*

For publications I, III, IV and V, the author was mainly responsible for all parts of the publications. For publication II, the author participated in the parameters fitting process and writing process.

1. Introduction

1.1. General

Fuel cells are electrochemical devices which convert the chemical energy of reactants directly into electrical energy, and as such they are not subject to Carnot cycle limitations like heat engines. This process enables achieving high efficiently compared to the conventional internal combustion engines. Another favorable characteristic of fuel cells is their very low environmental impact since fuel cells generate electricity without burning fuel. In addition, because there are fewer moving mechanical parts or vibrations, noise due to the operation is also reduced. All these characteristics drive a great interest for both terrestrial and space applications, such as automobiles, trains, stationary electric power plants, airplanes, submarines and space shuttles.

A reduced dependence on crude oil is also a strong motivator for the effort of fuel cell development all over the world. The fuel of fuel cell, hydrogen, can be produced by numerous processes, such as steam reforming of natural gas, electrolysis, or as a byproduct of petroleum refining and chemicals production [1,2]. Hydrogen can be also available at such sites as for instance chlor-alkali factories or coke oven plants where hydrogen can be produced as a by-product. Furthermore, hydrogen production is expected to be a potential process for increasing the fuel economy of conventional technologies, by utilizing the waste heat of electricity generation process such as in nuclear energy [3]. A number of advanced processes of hydrogen production have also been studied, the examples include biological water splitting, photoelectrochemical water splitting, reforming of biomass and wastes, solar thermal water splitting and renewable electrolysis. Although fossil fuels will be used to produce hydrogen in the medium term, in the long term hydrogen can be derived largely from renewable sources. Once the renewable-based hydrogen production process is established, a CO_2-neutral energy society, which is widely considered as the best overall solution in the long run for the global environment, may be realized with the use of fuel cells.

Over the past 20 years, the focus in terms of research and development on fuel cells has shifted dramatically. Because of a surge in oil price in the 1970s, more focus was on large scale power generation using molten carbonate fuel cell (MCFC) and phosphoric acid fuel cell (PAFC). In the 1990s, transport, in particular light duty vehicles, gained more attention, leading to greater research and development on polymer electrolyte membrane fuel cell (PEMFC). Since 2000, there has been increasing interest in small-to-medium scale generation of power, using SOFC and PEMFC. Furthermore, direct methanol fuel cell (DMFC) development has also accelerated recently.

Above six fuel cell systems, namely AFC, DMFC, MCFC, PAFC, PEMFC and SOFC, are classified according to the type of electrolyte, system requirements, and temperature of operation. DMFC is considered to be a variant of PEM technology. The major differences between various fuel cells are summarized in Table 1. The requirement of noble metal for catalyst and fuel conditioning options are varied according to the type of fuel cell. In general, fuel cells operating at relatively low temperature require a platinum based catalyst and complicated fuel conditioners, which add cost and complexity to the system. On the other hand, fuel cells operating at higher temperature achieve high reaction rates without the need for expensive catalysts and gases such as natural gas can be internally reformed. However, the high operating temperature limits the materials selection and placement possibilities, and the relatively fast degradation of components and difficult fabrication processes are problematic.

Table 1 also includes the possible applications of fuel cell types. Depending on the system output and operation temperature, the examples of implemented applications may be varied for each fuel cell type. Small scale applications such as vehicle and portable applications are

attractive for PEMFC, DMFC, PAFC and AFC, while the large utility applications and combined heat and power (CHP) plants are envisioned as belonging to the MCFC and SOFC. Any kinds of fuel cell may be applied for stationary applications, depending on meeting the requirements and preferences of purchasers.

Table 1 Comparison of fuel cell type and characteristics

	PEMFC	DMFC	AFC	PAFC	SOFC	MCFC
Electrolyte Type	Proton Exchange Membrane	Proton Exchange Membrane	Potassium Hydroxide	Liquid Phosphoric Acid	Solid Zirconium Oxide	Liquid Molten Carbonate
Catalyst	Platinum	Platinum/ Ruthenium	Platinum/ Palladium	Platinum	(Perovskites)	(Nickel)
Operating temperature	Room temp. to 100 ˚C	Room temp. to 90 ˚C	Room temp. to 150 ˚C	150-200 ˚C	650-1000˚C	600-700 ˚C
Electric efficiency (LHV)	25-60%	>50%	50-60%	32-45%	35-55%	45-55%
Typical system output	<1kW-250kW	1W-100W	10kW-100kW	50kW-1MW	5kW-3MW	<1kW-1MW
Applications						
Passenger vehicle	√	√	√		(√)	
Cogeneration	√		√	√	√	√
Potable power	√	√	√			
Utility power			√	√	√	√
Distribute power	√		√	√	√	√
Heavy duty vehicles	√	√	√	√	√	
Specialty power	√	√	√			

PEMFC operates at a relatively low temperature range between the freezing and boiling points of water, which contributes to its quick start-up and shut-down. In addition, they are smaller in volume and lighter in weight compared to other fuel cell types and the electrolyte is solid material, thereby making the technology attractive for portable and automotive applications. That is why most major automobile and electronics companies are competing in fuel cell development and why approximately 90% of fuel cell research and development work involves PEMFCs [4,5].

Although PEMFC is the type under the most active development in the industry, its implementation is beset with formidable technical difficulties. The major obstacles ahead of us include the high initial cost of manufacturing the fuel cell and cost of hydrogen. The cost target of a fuel cell system is around 30 €/kW, currently two orders of magnitude higher than the target [6]. Furthermore, the lack of an infrastructure to supply fuels to the cells, and the lack of familiarity in industry and general public with the fuel cells are also challenging hurdles to overcome [7]. From the engineering point of view, the insufficient durability and stability of fuel cell, arising from factors such as cathode catalyst oxidation, catalyst migration, catalyst agglomeration, corrosion of the carbon support and membrane degradation, are the main concerns. Real-life operation conditions such as numerous start-ups and shutdowns and impurities in fuel and air may cause unexpected performance drop after a long operation period. Therefore, thorough understanding of in-situ phenomena both from experiment and modeling points of view are necessary.

1.2. Background and motivation for this study

The overall fuel cell performance is governed by a complicated interplay of transport phenomena, including reactant, product, charge and heat transport. A mathematical model is a powerful tool for studying the various phenomena occurring in a fuel cell from local to system level, predicting the fuel cell performance under different operating conditions and optimizing the design of fuel cell systems. However, any model generally requires a number of assumptions and/or simplifications due to the limitation of the numerical techniques and experimentally evaluated data, which may then lead into significant error in the modeled results and does not represent the physically realistic situation.

One of the most common shortcomings of previous studies is disregarding the effect of compression on the physical properties of the cell components. Gas diffusion layers (GDLs), in fact, are deformed when assembly pressure is applied, resulting in changes in their morphology and physical properties. Of particular importance is the fact that the compression pressure over GDL is inhomogeneous because of the rib/channel structure of neighboring bipolar plate. In an actual fuel cell assembly, the compression force is in practice exerted only on the GDL under the rib area of bipolar plate but not under the channel. This inhomogeneous compression leads into thickness variation of GDL, which significantly affects local transport phenomena, cell performance and cell life-time. However, typical published fuel cell models do not take into account the inhomogeneous compression of the GDL and its effects, but instead assume the geometric and physical parameters of GDL constant over the cell area.

The right choice of modeling parameters is essential for accurate prediction of local phenomena, which can not be easily interpreted by only superficial modeled results, such as the polarization curves. So far, however, information on experimentally evaluated modeling parameters has been limited and further investigation of physical properties of GDLs is essential, especially paying attention to the effect of compression. Therefore, the aim of this study is to present a method for determining the physical properties of GDL and to provide reliable data. The experimental work includes on the subjects of the GDL's mechanical properties, electric conductivity, electric contact resistance, gas permeability, thermal conductivity and thermal contact resistance. Furthermore, theoretical study based on the achieved experimental results was also conducted to study the effect of physical properties change on local transport phenomena inside the fuel cell.

1.3. Outline of thesis

This thesis begins with a short introduction to the operation principles and components of a PEM fuel cell in Chapter 2. Chapter 3 addresses experimentally evaluated GDL characteristics as introduced in Publication I, III and IV and theoretical analysis introduced in Publication II and V. Chapter 3 also includes additional results which are not included in the published articles and suggestions for further studies. Summary of this thesis is given in Chapter 4. Manuscripts of Publication I, II, III, IV and V are included as appendices.

2. Proton Exchange Membrane Fuel Cell

2.1. Principles of Operation

PEM fuel cell uses hydrogen as fuel at anode side and oxygen (from air) as oxidant at cathode side. Hydrogen is split into protons and electrons according to:

$$H_2 \rightarrow 2H^+ + 2e^- \quad (1)$$

Driven by an electric field, the protons migrate through the polymer electrolyte membrane and electrons via an external electric circuit to the cathode. The oxygen in the cathode side reacts with the protons and electrons to form water according to:

$$\frac{1}{2} O_2 + 2H^+ + 2e^- \rightarrow H_2O \quad (2)$$

The overall reaction is exothermic and can be written as:

$$H_2 + \frac{1}{2} O_2 \rightarrow H_2O \quad (3)$$

The operational principle of a PEM fuel cell is illustrated in Fig. 1.

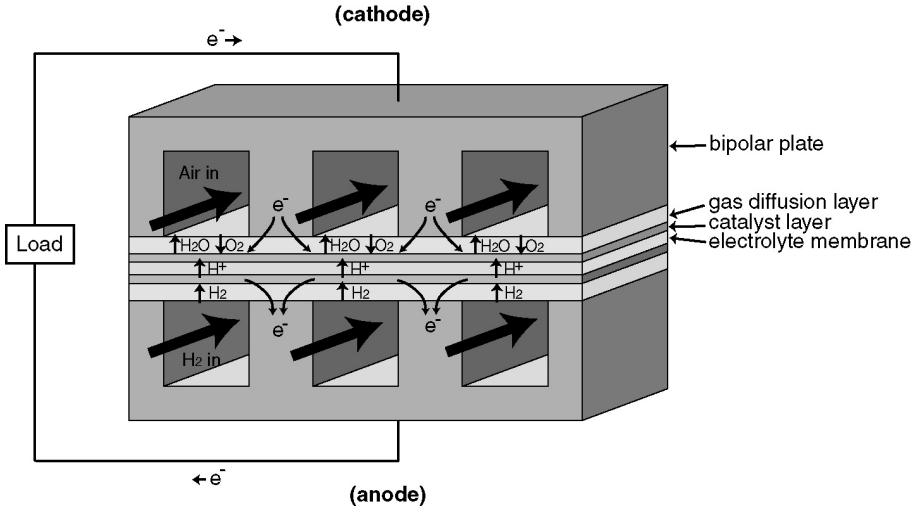

Fig. 1 Schematic illustration of an individual fuel cell

The maximum electric power, W_{el}, obtained in fuel cell operation at constant temperature and pressure is expressed by the change in Gibbs free energy ΔG of the electrochemical reaction:

$$W_{el} = \Delta G = -nFE \quad (4)$$

Where n is the number of electrons participating in the reaction, F is Faraday's constant (96485 coulombs/mol), and the E is theoretical equilibrium potential of the cell. For reactants and products in their standard states conditions (298 K and 1 atm), represented by the superscript $^\circ$,

$$\Delta G^\circ = -nFE^\circ \quad (5)$$

The theoretical standard potential, E°, at 298K for a fuel cell in which hydrogen and oxygen react is 1.229 V with liquid water product, or 1.18 V with gaseous water product. The difference in ideal standard potential stems from Gibbs free energy change of vaporization of water at standard conditions.

The relationship between the theoretical standard potential, E°, for the cell reaction and the theoretical equilibrium potential, E, at various partial pressures of reactants is given by the Nernst equation:

$$E = E^{\circ} + \frac{\Re T}{2F}\ln\left[\frac{P_{H_2}}{P_{H_2O}}\right] + \frac{\Re T}{2F}\ln\left[P_{O_2}\right]^{\frac{1}{2}} \tag{6}$$

The actual cell voltage is decreased from the theoretical equilibrium potential because of 1) crossover losses, 2) activation overpotential, 3) ohmic overpotential and 4) concentration overpotential.

Even though the polymer membrane is impermeable to the reactant gases, some small amount of reactant gases diffuse through the electrolyte membrane. This fuel crossover is essentially equivalent to the so-called internal currents since each hydrogen molecule contains two electrons. Because of the current losses due to this internal current, the open circuit voltage is significantly lower than the theoretical voltage, usually less than 1 V. Hydrogen crossover is a function of membrane permeability, membrane thickness, operating conditions and hydrogen partial pressure. A very low open circuit voltage may indicate either hydrogen leak or electrical short.

The activation overpotential, η_{act}, arises from sluggish reaction kinetics and is dominant at low current density. The activation overpotential is expressed with Butler-Volmer equation as:

$$i = i_0\left\{\exp\left(\frac{-\alpha z F \eta_{act}}{\Re T}\right) - \exp\left(\frac{(1-\alpha) z F \eta_{act}}{\Re T}\right)\right\} \tag{7}$$

where R is the gas constant, T the temperature, α the electron transfer coefficient of the reaction, i the current density, and i_0 the exchange current density.

Exchange current density is a measure of an electrode's readiness to proceed with the electrochemical reaction. Thus, the lower the activation overpotential is, the higher the exchange current density becomes. The activation overpotential of hydrogen oxidation reaction is much lower than that of oxygen reduction reaction, and thus the anode exchange current density is several orders of magnitudes larger than that at cathode ($\sim 10^{-4}$ vs $\sim 10^{-9}$ A cm^{-2} at 25 $^{\circ}$C and 101.25 kPa). The exchange current density is dependent on reactant concentration, temperature and electrode catalyst loading and catalyst specific surface area. Because of its concentration dependence, the exchange current density inherently entails the correlativity to the concentration overpotential.

The ohmic overpotential, η_{ohm}, arises from ionic and electronic resistance of fuel cell components. The resistive losses obey the Ohm's law:

$$\eta_{ohm} = iR_{cell} \tag{8}$$

where R_{cell} is the area-specific total resistance of the fuel cell, which includes electronic, ionic, and contact resistance:

$$R_{cell} = R_{electric} + R_{ionic} + R_{contact} \tag{9}$$

It has been thought that the dominant part of ohmic loss is ionic resistance of membrane. However, the electric contact resistance between catalyst layer (CL) and membrane was found to be quite comparable to ionic resistance of membrane as discussed in sub-chapter 3.2.5. The ohmic loss depends on cell geometry, the materials used, and the operating temperature. This is a key performance parameter especially in high-temperature fuel cells, where the ohmic losses often dominate the overall polarization of the cell.

As reactants are consumed at the CL by the electrochemical reaction, concentration gradients are established and the concentration overpotential occurs. The concentration overpotential contributes significantly to loss of cell potential at high current density, where the reactant is

rapidly consumed. Furthermore, in low operating temperature fuel cell such as PEMFC and DMFC, hindrance of gas-phase reactant transport by produced liquid water in the GDL and CL can significantly increase the concentration overpotential.

The typical shape of the polarization curve is illustrated in Fig. 2. The three separate regions indicate where the different loss mechanisms, i.e. overpotentials, are dominant. The processes in the fuel cells are very complicated because of the tight coupling between electrochemical and transport processes. Thus rigorous theoretical analysis is required to obtain the accurate picture of the occurring phenomena in the fuel cells. There, the detailed knowledge of the embedded parameters of electrochemical kinetics, fluid flow, charge transfer, mass transfer and heat transfer is highly important and sufficient experimental assessments of them are necessary.

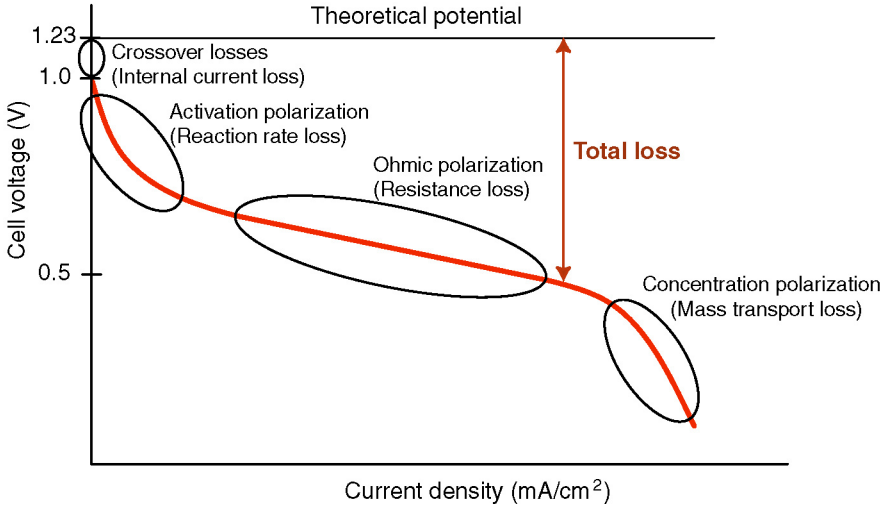

Fig. 2 Ideal and actual cell voltage/current characteristic for a PEMFC

2.2. Water and Heat Management

Because of the low operating temperature of PEMFC, some of the byproduct water does not evaporate and remains in liquid form within the components as well as in DMFC [8,9]. At the cathode of a fuel cell, water is generated through electrochemical reactions and exists as a vapor and/or liquid phase depending on local temperature. The excess liquid water fills the pores of the GDL, which significantly hinders oxygen access towards the catalyst [10-15], a phenomenon referred to as 'flooding'. This is typically the origin of the limiting current for PEM fuel cells. At subzero temperatures, the liquid water forms ice or frost. Once the pores of GDL and CL are filled with the ice or frost, reactant transport to the reaction sites is significantly blocked, and the fuel cell performance is suddenly degraded [16,17]. In addition, the resulting clogging of flow channels by liquid water droplets shuts down the entire electrochemical reaction in those channels and has recently been implicated in cell durability problems [18,19]. The driving force of liquid water transport is created by the local capillary pressure gradient, which is a strong function of water saturation [20]. Therefore, once liquid water is present in the channel, the channel/GDL interface is no longer dry and this reduces the water saturation gradient in the GDL downstream, which consequently reduces the rate of water transport by capillary action [13].

The capacity of liquid water retention depends strongly on the material properties. Therefore, the wettability characteristics of the GDL, its surface and CL are of paramount importance. Typically GDLs are tailored by addition of hydrophobic agent to increase the hydrophobicity

and to enhance the liquid water removal. Unlike the hydrophilic pore where liquid water is preferentially adsorbed by the fiber surface as depicted in Fig. 3(a), the hydrophobic pore surface distorts the molecular force balance at the line of contact, which results in forcing the liquid water to move towards an unstable state (see Fig. 3(b)), and leads into a higher capillary pressure within the pore. Obviously, the degree of hydrophobic agent loading plays a determining role in the capillary transport mechanism. The hydrophobic treatment, however, reduces the porosity of the GDL simultaneously, and thus an optimum loading must be carefully determined considering the desired operating conditions [21-24]. Recently, Kumber et al. discussed that the compression pressure and operating temperature also affects the capillary pressure [25,26].

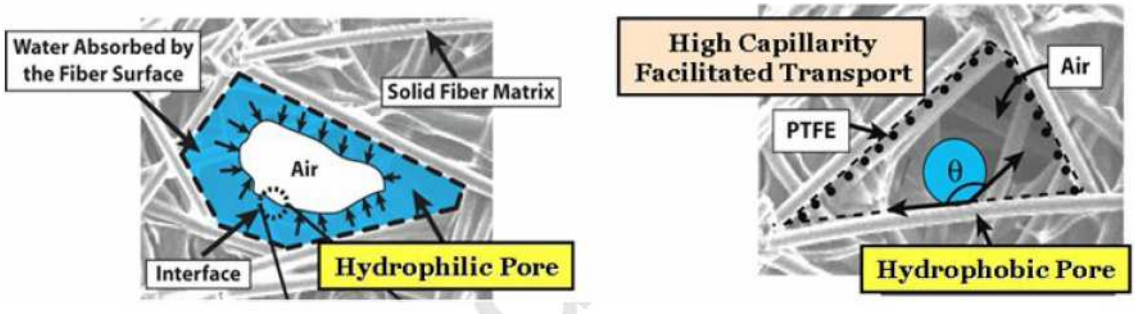

Fig. 3 Schematic illustration of liquid water droplets inside a pore of a GDL with different hydrophobicities (Figures: Kumbur et al. [27]).

On the other hand, deficiency of water decreases the proton conductivity of the membrane and severely impacts membrane lifetime, and thus humidification of reactants is typically needed. Ideal humidity conditions exist for each set of operating conditions, and clearly, understanding the formation, behavior and movement of liquid water inside the components of the cell is of great importance. Water content in membrane is determined not only by the operation conditions but also by membrane characteristics. The electro-osmotic drag coefficient of water, defined as the number of water molecules dragged per proton, is an important factor. During operation, 1-3 water molecules are dragged with each proton [28,29]. As a result, a concentration gradient of water will be formed through the membrane where the anode is drier than the cathode. Under these conditions, the back-diffusion of water from the cathode to anode will occur and also the membrane thickness becomes important. Furthermore, water can be pushed hydraulically from one side of the membrane to the other if there is a pressure difference between the anode and the cathode. A net water exchange through the membrane should be optimized according to the system. Adherence of the membrane and CL is also important especially at subzero temperature [30]. Intimate contacts between them avoid creating a space where liquid water is trapped [4].

The effect of operational and material parameters to the water management and consequent fuel cell performance has been energetically discussed, see, e.g. [31-37]. Mathematical models suggest that liquid water is prone to condensing under the rib [12] and water management would be difficult especially when the GDL is thin [11,12]. During fuel cell operation, it is essential to diagnose either flooding or drying inside the fuel cell stack and thus diagnostic methods have been developed [38-40]. Quantification of liquid water in GDL has been attempted by numerous methods, such as optical visualization using transparent fuel cell [19], neutron radiography [40,41], magnetic resonance imaging and X-ray microtomography, see, e.g. [42].

Water transport inside the fuel cell has a close link to temperature distribution since water and oxygen diffusivity, the phase change of water, saturation parameters, and reaction kinetics are all temperature dependent, see, e.g. [43]. Therefore, extensive modeling studies have been devoted to obtaining an accurate picture of the combined thermal and water transport

phenomena, see e.g. [44-46]. Furthermore, accurate prediction of the temperature distribution is of vital importance for achieving better and more stable fuel cell performance. This is because the temperature distribution caused by inadequate thermal and water management may lead into formation of local hotspots in the cell, which may degrade the cell components and drop the life-time of the cell [47-49].

2.3. Fuel Cell Structure

A typical PEM fuel cell consists of 1) bipolar plates with channels machined on either side for reactant distribution over the electrode surface, 2) a membrane electrode assembly (MEA) where the electro-chemical reactions and proton transport take place, and 3) porous gas diffusion layers (GDL) sandwiching the MEA (see Fig. 1).

2.3.1. Membrane

It is often mentioned that the proton-conductive polymer electrolyte membrane is the heart of a fuel cell, and significant efforts have been devoted for development of better ionic conductive membrane, see, e.g. [50,51]. Typically, the membrane consists of a perfluorinated polymer backbone with sulfonic acid side chains. Fig. 4 shows the chemical structure of the best-known membrane material, Nafion ™.

The polymer electrolyte membrane is required to exhibit high proton conductivity, to present an adequate barrier to mixing of fuel and reactant gases, and to be chemically and mechanically stable under the fuel cell operation environment.

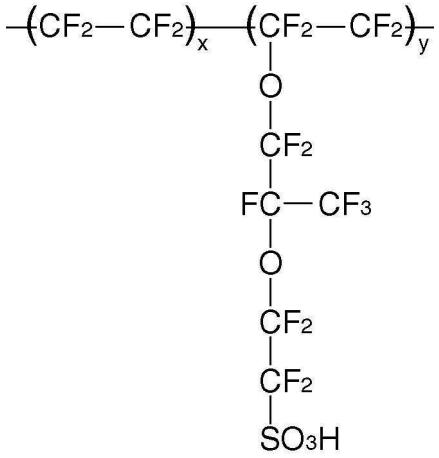

Fig. 4 Structure of perfluorocarbon-sulfonic acid polymer (Nafion™).

The perfluorinated polymer backbone is highly hydrophobic and the sulphonic acid at the end of the side chain is highly hydrophilic. The hydrophilic regions absorb relatively large amounts of water (in some case up to 50% by weight), through which the proton can travel. Therefore, the ionic conductivity of the membrane is strongly dependent on its water content, λ (mol H_2O/ mol $SO_3^-H^+$). The maximum amount of water in membrane depends on the state of water used to equilibrate the membrane, e.g. λ =22 for a Nafion membrane when it is equilibrated in boiled water and λ =14 when water is taken from water vapor [28,52]. Furthermore, the water uptake was reported to be also dependent on temperature [51,53]. Water uptake results in membrane swelling, which is a significant matter for cell design and

assembly and should be carefully taken into account. It has been reported that the dimensional change can be up to 10% [29,54].

2.3.2. Catalyst layer

The electrochemical reactions take place in the CL. The CL typically consists of carbon supported platinum catalyst and ionomer (see Fig. 5(a)). Because of slow oxygen reduction reaction (ORR), typically much more Pt catalyst is required in the cathode CL than for the faster hydrogen oxidation at the anode. The ionomer content and characteristics of the solvent used to disperse the catalyst and ionomer are also important parameters to achieve the optimum morphology and microstructure of CLs [55]. The CL is deposited onto either electrolyte membrane or GDL by spreading, spraying, sputtering, painting, screen printing decaling, evaporative deposition and impregnation reduction, followed by a hot-pressing process.

Since there are three kinds of species, i.e. gas, electron and proton, which participate in the electrochemical reactions, the reactions take place only where all three species have access (three-phase boundary). One of the major cell performance-limiting factors is the blocking of reaction sites by liquid water [10] (see Fig. 5(b)), which prevents the reactant from reaching the active reaction site particularly at low air pressure. Therefore, hydraulic permeability as well as ionic conductivity are important parameters of CL [56]. In order to expand the three-phase boundary area, the CL is formed as a porous structure. Furthermore, it is important that the platinum particles are small enough (typically 4 nm or smaller) to expand the surface area and evenly dispersed on the surface of carbon support (ca 40 nm). In order to elucidate such complicated transport phenomena, various mathematical models have been developed for the CL, for example, pseudo-homogeneous model, see, e.g [56], heterogeneous models using such as thin film-agglomerate approach, see, e.g. [10]. However, there are still a lot of uncertainties in the design parameters.

In addition to the flooding problem, research areas such as the catalyst degradation [57], the carbon support [58], the morphology of CL [59], the development of CO-tolerant catalysts [60] and non precious metal catalysts [61] are also actively studied to reduce cost and improve durability.

(a) 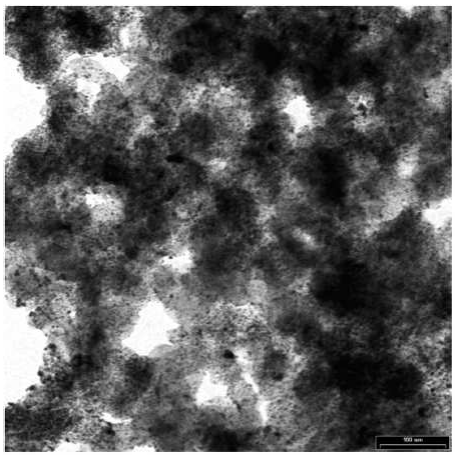 (b) 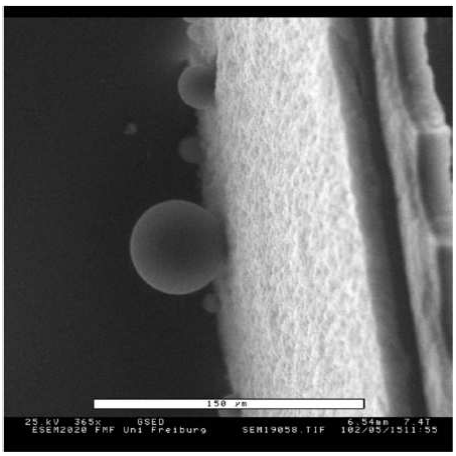

Fig. 5(a) TEM image of catalyst layer. The small black dots are the catalyst particles, the larger circular features are the carbon black support and the ionomer appears light gray (b) ESEM image of catalyst layer with water droplet with a radius below 100 µm (Figures: Ziegler et al. [62]).

2.3.3. Gas Diffusion Layer

GDLs typically consist of randomly aligned carbon fibers or woven spun yarns to have high porosity. Examples of carbon type GDLs are shown in Fig. 6(a) and (b). In addition to the carbon GDLs, metallic GDLs or metal mesh diffusers have also been proposed as GDL [63]. Although the carbon cloth-type GDLs may present higher power performance than that of paper-type GDL [64], there are considerable academic and industrial interests in using paper-type since there is a cost advantage with non-woven substrate and it is more convenient to fabricate a micro-porous layer (MPL) or catalyst layer directly onto them.

(a) 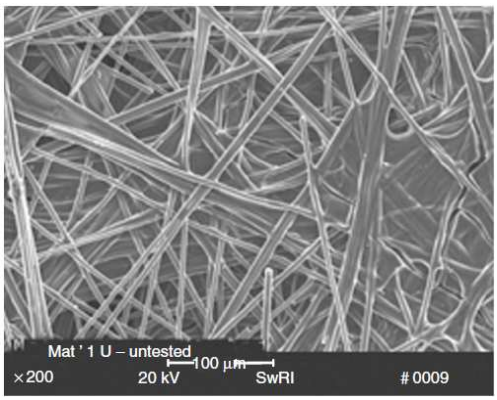

(b) 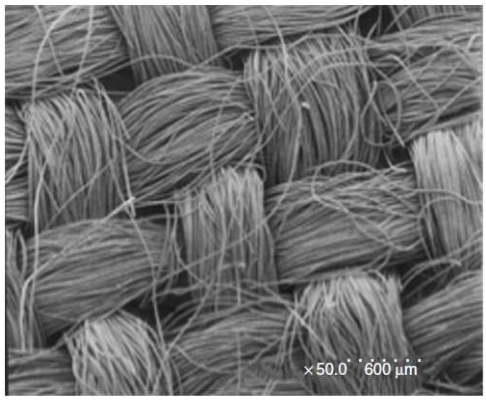

Fig. 6(a) Carbon paper consisted of randomly aligned carbon fibers,
(b) Carbon cloth woven the spun yarns (Figures: Mathias et al. [65]).

Until recently, less attention has been paid to the GDL even though it plays a crucial role in fuel cell operation. The GDL covers a wide range of functions in fuel cell operation:

1. It provides a passage for reactant access from the flow field channel to CL
2. It provides a passage for product water removal from CL to flow field channel
3. It conducts electrons between CL and flow field rib
4. It conducts heat generated in the electrochemical reaction in the CL to the flow field ribs
5. It provides mechanical support to the CL and membrane

These functions impose requirements on the morphological, electric, thermal and mechanical properties of GDLs, i.e. high porosity, suitable water management properties, high electric and thermal conductivity, and chemical and physical durability. Comprehensive details are provided by Mathias et al. [65].

GDLs have a large impact to the optimum humidification level and liquid water distribution in the CL. This is required in order to minimize the ohmic resistance of the ionomer and to prevent the appearance of local hot spots in the catalyst coated membrane. Depending on the specific operating conditions, a variety of aspects of the GDL come into play.

Alike in CLs, flooding in GDL is often stated as a problematic issue. Limited gas-phase transport in GDL by condensed liquid water (see Fig. 7(a)) determines the cell limiting current and also affects the slope of the polarization curve in the medium current density domain [56]. Therefore, the GDLs are generally made hydrophobic to enhance liquid water removal. Typically, GDLs are impregnated with polytetrafluoroethylene (PTFE) or fluorinated ethylene propylene (FEP) by e.g. dipping the GDL in to the PTFE solution followed by drying and sintering. The amount of the hydrophobic agent is a sensitive issue, since some amount is certainly required to alleviate the flooding but excessive impregnation results in blockage of surface pores and reduction of porosity, see, e.g. [21,34].

Depending on the specific operating conditions, an additional layer can be coated on the GDL (see Fig. 7(b)). The commonly used layer is MPL, which consists of carbon or graphite particles mixed with polymeric binder such as PTFE. Since the pore size of the MPL (100-500 nm) is orders of magnitude smaller than that of the GDL (10-100 µm), the electric contact resistance with the adjacent CL can be reduced. In terms of hydrophobicity, the MPL contains considerably fewer hydrophilic pores, and thus it is almost exclusively hydrophobic in nature [69]. Therefore, the MPL provides effective wicking of liquid water from CL, resulting in much smaller water droplets less likely to clog and flood inside the CL [20,66]. In addition, the MPL keeps the membrane hydrated by pushing water away from the GDL [11]. Adding a MPL on cathode GDL may be more important than on anode GDL since more severe flooding occurs at cathode [67].

The bulk and interfacial properties of GDL depend strongly on compression. The changes in the physical properties have critical consequences on transport phenomena, which are key point of this study and described in chapter 3.

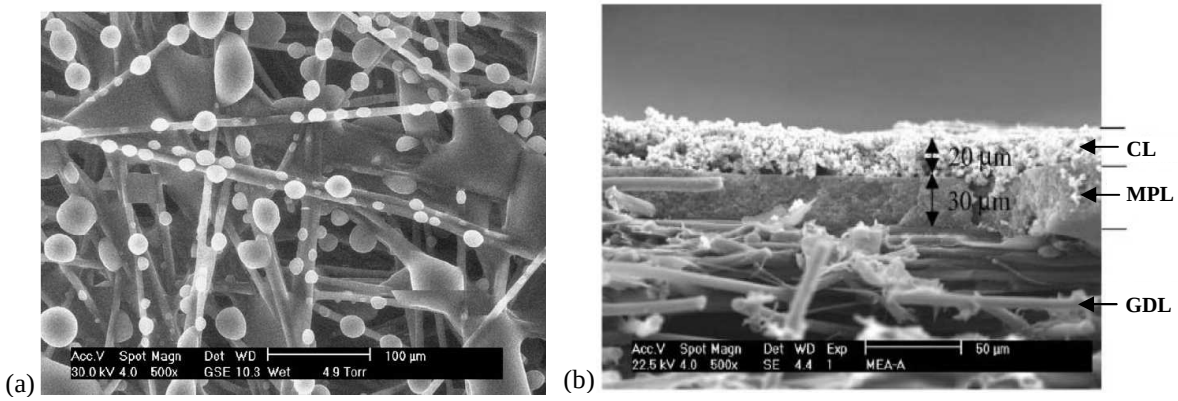

Fig. 7(a) Water droplets formed on the GDL fibers (Figure: Gurau et al [68])
(b) GDL with MPL, the white dense layer is CL (Gostick et al. [69]).

2.3.4. Bipolar plate (flow field plate)

The bipolar/flow field plate is one of the most expensive components of the fuel cell stack and accounts for more than 80% of the total weight of the stack. The bipolar plate provides a separation between the individual fuel cells and forms a series of electrical connections across different cells in the fuel cell stack. The channels grooved onto it supply fuel and oxidant gas streams to individual cells.

At high current density and/or low flow rate of reactants, the accumulation of liquid water in the gas channels becomes problematic. If water droplets appearing on the channel surface clog the channel (see Fig. 8), the entire electrochemical reaction in the channel downstream from the water blockage is shut down, and thus the cell's active area is reduced drastically. Furthermore, this water clogging increases parasitic pressure loss and provides facilitated transport of ionic impurities, which can accelerate the ionomer degradation. On the anode, liquid blockage can cause voltage reduction and fuel starvation in the CL, which can lead to oxidation of carbon support and accelerated degradation. Therefore, this phenomenon can be much more critical than the flooding of the GDL or CL for a better and more stable fuel cell operation. Obviously, the water clogging in the channel has to be avoided by e.g. hydrophilic treatment of the channel walls, improving the surface properties of GDL such as the roughness and hydrophobicity, employing purging procedures of liquid water and improvement of flow field geometry. The complicated mechanisms of the liquid water growth and its movement have been discussed in literature, see, e.g. [41,70].

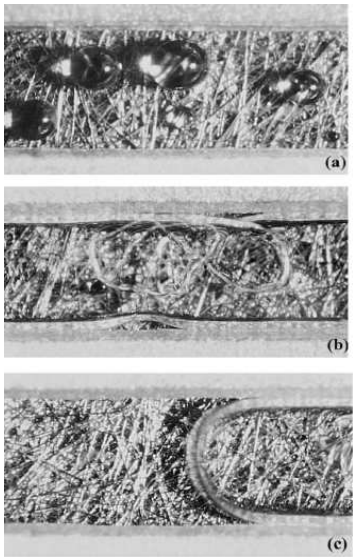

Fig. 8 Snapshots of dynamic process of water droplet formation process. The water droplets start to appear on the preferential location (a), coalesce to the channel walls (b), and finally clog the channel (c). (Figures; Zhang et al. [19]).

Conventionally, bipolar plates are made out of graphite with machined gas flow-field channels. However, the machining process is tedious and expensive. Furthermore, a graphite based bipolar plate is brittle, and therefore alternative materials and design concepts are under active study, see, e.g. [71-75]. Instead of the graphite bipolar plates, metallic plates have been gaining attention because of its advantages such as suitability for mass manufacturing, high electric and thermal conductivity, mechanical rigidity which can makes the plate very thin (e.g. less than 1 mm) resulting in compact and lightweight stacks. However, the metal plates are easily corroded when they are exposed to a fuel cell operating environment (pH 2 to 4 and temperature 60 to 80 ˚C). The metal ions from corroded metallic bipolar plates would diffuse into the cell, and contaminate the CL and membrane [84]. To avoid this corrosion problem, the metallic bipolar plate is given a passive treatment, which, in turn, increases the ohmic resistance. Several ideas have been proposed to overcome these persistent problems, e.g. highly electrically conductive metallic inclusions are dispersed on a stainless steel base, which is then given an oxidized coating see, e.g. [76,195]. This prevents corrosion while establishing a compulsory electrical pathway, to achieve good electrical and thermal conductivity (see Fig. 9).

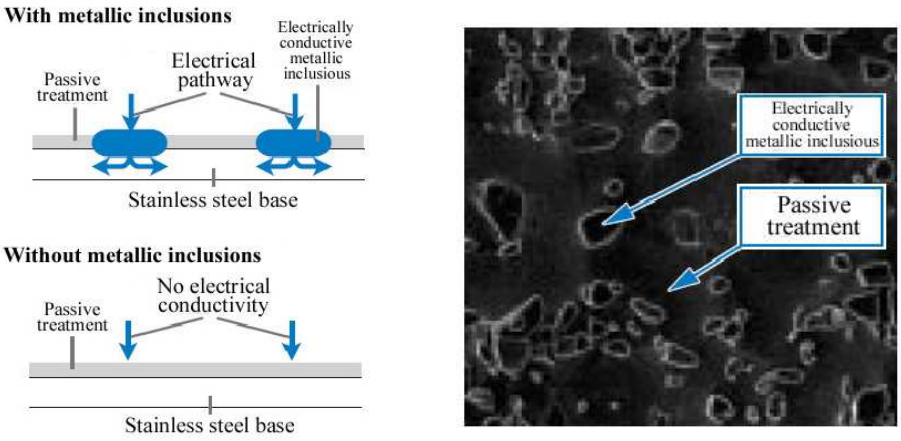

Fig. 9 An example of application of metallic bipolar plate
(Figures: Honda press information [76]).

2.3.5. Other components

In addition to the components discussed in the previous chapters, a PEM fuel cell requires also other components such as gaskets, endplates, clamps and gas manifolds. At system level, a variety of auxiliary components such as temperature controllers, mass flow regulators, gas humidifiers, compressors and gas purification systems are required for proper operation.

2.4. Applications of PEM fuel cells

The applications of fuel cells vary depending of the type of fuel cell to be used. Since fuel cells are capable of producing power anywhere in the 100 mW to 10 MW range they can be applied to almost any application that requires power. In the smaller range they can be used in mobile phones, PCs, and any other type of personal electronic equipment. In the 100 mW–100 kW range a fuel cell can be used to power vehicles, stationary, military purpose, as well as any auxiliary power unit application. In the large scale applications, e.g. the 1–10 MW range, fuel cells can be used for distributed power generation. In the following, main targets, obstacles, potential benefits and future prospects for key applications are briefly described.

Vehicles application

Fuel cell vehicles (FCVs) are one of the most promising applications of PEM fuel cell because of its high fuel efficiency and environmental-friendly characteristics, as well as potential to cut the dependence of foreign energy sources. Even though hydrogen is more expensive than conventional fuel by weight or volume, FCVs are much more efficient than internal combustion engine vehicles (ICV); the driving efficiency of FCVs is close to 50%, compared to about 15% for gasoline combustion engines. On this basis, the per-km costs for FCVs are comparable to gasoline vehicles even with today's prototypes. Relatively fewer moving parts in FCV is also favorable since it may dramatically decrease the likelihood of failure. FCVs have a great advantage over even electric vehicles (EVs), they do not need long recharging time like EVs, only fuel, and they have much higher power densities than current commercialized batteries, which enables longer driving range than EVs. There has been steady progress in the development of fuel cell stack and the technology of hydrogen storage on board. More than hundred FCV prototypes are announced every year by car manufactures.

The main technological hurdles of FCV development are

1. Cost

Based on current best technology, production cost of FCV engine is $225 per kW, which is still far too expensive compared to conventional ICV engine for private cars ($60 to $100 per kW) [77,78]. The major high-cost contributing components are the catalyst (precious metal such as Pt or Pt-alloys), electrolyte membrane and bipolar plate. Several studies conducted by major car manufactures have shown that the FCVs could be produced cost-competitively, if mass production manufacturing techniques are applied [79].

2. Driving range

An approximately 500 km range is used as reference of targeted drive range. In order to extend the driving range of FCV, other components such as hydrogen storage tank, secondary battery and power control unit are subjects of urgent development.

3. Reliability

FCV must survive and operate in various weather conditions, e.g. -40 to 40 ˚C. In start-up and operation in extremely cold climate, the residual and product water becomes ice or frost, which significantly hinders the electrochemical reactions and may damage the cell components such as membrane [17,80]. Obviously, temperature dependent water retention characteristic of components such as GDL, MPL and membrane is an important parameter

[16,81], and the proper purging process and start-up current density must be carefully designed for proper cold start-up operation [82]. Furthermore, the real-life operation conditions such as numerous start-ups and shutdowns, and impurities in fuel and air can affect the durability of cell components and must be considered in sufficient detail to improve the reliability [83,84].

The power density of fuel cell system is still lower than that of conventional ICVs engines, making the fuel cell drive train much heavier and bulkier. Thus, the further technology development still focused on the size reduction including hydrogen storage system and performance improvement.

Although fuel cell reaction itself does not produce harmful gases such as NO_X and CO_2 (tank-to-wheel path), they are produced during the hydrogen production process (well-to-tank path). Therefore, total energy efficiency and greenhouse gas emission through the well-to-wheel path are important evaluation criteria.

The development of hydrogen infrastructure including storage, distribution and production issues remain an integral part of the fuel cell commercialization process, therefore, car manufactures, energy companies and government agencies need to work together in joint development programs and to share their knowledge [5,85]. At the same time, it is necessary to develop standardization, safety codes, and regulations for production, distribution and storage of the fuels, and to educate the industries and end-users to let fuel cell as more common energy form.

Fuel type remains an important consideration for development of FCV [79]. To date, compressed hydrogen gaseous system yields the best overall technical performance and shows the highest maturity for automotive applications. Although the liquid form of hydrogen has a very high energy density, this system has lots of drawbacks including difficult thermal insulation, evaporation loss, and system complexity. Another alternative for hydrogen storage is the use of metal hydrides. The engineering burden of this system is its long refueling time, the requirement of operating pressure above 10 MPa and the limit of operating temperature to 70 ˚C.

Stationary applications

Although vehicle applications of fuel cells are gaining more attention, the applications for stationary power generation may offer even greater market opportunities. The advantage of stationary fuel cell applications is that the system cost targets are much less demanding than in automotive applications, fuel is more easily available, fuel storage is not so problematic and typically the size and weight constraints are not critical, which all allow the fuel cell to be operated at favorable conditions.

Hydrogen can be produced from natural gas whose infrastructure is already in place. The fuel conversion is done by methods such as steam reforming with separate units using special catalysts operating at high temperatures [2]. In this process, the sulfur-containing compounds which are used to give an odor to natural gas in case of leakage are removed. It can also be done by operating the fuel cells at such high temperatures that their own catalysts can convert the fuel to hydrogen at the electrodes.

Fuel cell power generation systems in operation today achieve more than 35% fuel-to-electricity efficiency utilizing hydrocarbon fuels [86]. When the fuel cell is sited within or near the facility where the electricity is to be used, its waste heat produced during the electricity generation can be captured and recovered for useful purposes. In residential systems, these fuel cell cogeneration systems improve the total system efficiency drastically, even up to 80% [86,87].

Stationary fuel cells may be used in different applications, namely,

1. Grid parallel and grid interconnected
The fuel cell systems provide electricity when needed, and the grid is used to cover short-term demand peaks (grid-parallel). The fuel cell system can be designed to export the excess power to grid (grid-interconnected).
2. Stand-alone
The fuel cell system provides power without a grid. This application is conceivable in areas such as remote entities, where the grid connection is not practical or does not offer reliable power. Typically, secondary battery is also added to this system in order to follow the load changes, and the dynamic behavior of fuel cell systems under various load conditions must be considered [88].
3. Backup or emergency generator
This system may be equipped with an electrolyzer-hydrogen generator and a hydrogen storage, with which the unit generates its own fuel when electricity from the grid is available.

The key to the commercial implementation of stationary fuel cell systems is the lifetime. It is generally recognized that a cost-effective stationary fuel cell power plant is required to operate 40,000 to 80,000 hours (5 to 10 years), whereas 3000 to 5000 hours is enough for automotive systems. The most critical component of the fuel cell which limits stack life is typically the MEA [89].

Mobile and portable applications
The driving forces for fuel cell applications in the portable sector are very different from those for vehicle or stationary applications. Here, environmental issues are not the key driver and the main advantage of fuel cells is instead high energy density, which allows portable devices to run for longer periods than those with batteries.

Small-scale fuel cells can be used as battery replacements in the most attractive high-volume consumer markets. A number of prototypes have already been demonstrated for e.g. mobile phones, laptop computers, music players, PDAs, gaming consoles and flashlights [90]. Other applications for micro fuel cells include low power remote devices such as hearing aids, smoke detectors, burglar alarms, hotel locks and meter readers.

Obviously, the reduction of size and weight is important for these small fuel cell applications. Another critical issue is the fuel and its storage. Gaseous hydrogen is not a good option due to bulkiness and weight of its storage. Therefore, most portable fuel cells use methanol as fuel, either directly or via microreformers [91]. Furthermore, simplicity of the system is also important. A cell or a stack whose power density is below 100 mW cm^{-1} typically operates in a dead-end mode, and air is often supplied passively. In such systems the cell dimensions, inter-cell spacing and the gap between the array and the bottom substrate must be optimized to achieve the best air flow patterns in the stack [92].

Military applications
Portable fuel cells are also used in military applications. They are lighter than secondary batteries and last longer, which is especially important to soldiers carrying heavy equipment in the field and carrying out long missions. Furthermore, the silent operation of fuel cells, unlike a diesel fueled generator, is of course favored in military operations.

One of the critical barriers to the fuel cell use in the military is the absence of an acceptable hydrogen delivery and storage system. Logistic fuels, defined as easily transportable and stored, and compatible with military uses, are difficult to convert to hydrogen for fuel cell use.

Furthermore, the current technologies such as compressed hydrogen tanks or metal hydrides do not meet the military's tactical requirements, since the energy density is still too low.

Therefore, more energy dense sources of hydrogen are being investigated, such as hydrogen storage in carbon nanotubes and microchannel reformers for hydrocarbon based fuels [93].

Closed environment and other applications

Since only exhaust from fuel cell reaction is water, the applications of fuel cells in closed environment have been favorable and studied since 1960s.

The first application of PEM fuel cell in a space mission was demonstrated in the Gemini missions in 1962. After that, alkaline electrolyte fuel cells were used in the Apollo and space shuttle missions. Fuel cell applications for submarines in place of nuclear energy source have been studied since 1970's throughout the world, due to their advantages of low noise and infrared signatures, high efficiency and low maintenance requirements. Such qualities are essential for submarines since they are expected to serve well into the future.

Furthermore, it has been suggested that fuel cells could be employed in marine applications to provide propulsion or auxiliary power for cruise ships, powered barges, ferry boats, offshore supply boats, push-tow boats, oceangoing tugs, and even submarine tankers. Fuel cells have also been suggested for use as power sources for offshore oil platforms, underwater facilities, and refrigerated containers on containerships. Some of these possible applications may be technically feasible and cost-effective in a decade or so.

3. Inhomogeneous compression of GDL

3.1. Effect of inhomogeneous compression

When the fuel cell is assembled, a certain compression pressure must be exerted to achieve adequate contact between the components and to ensure proper gas sealing. This assembling pressure affects significantly the fuel cell performance as suggested by e.g. Lee et al. [94], Ge et al. [95], Ihonen et al. [96], Lim et al. [97] and Chang et al. [98]. This is mainly because the soft and flexible GDL, typically made of highly porous carbon-fiber based paper or cloth, are deformed under the compression pressure, resulting in changes in their morphological and physical properties. A flowchart of the effects of increasing compression is presented in Fig. 10.

Generally speaking, increasing compression improves the electric and thermal conductivity of GDL and decreases the contact resistance at the interfaces. While a certain compression pressure is necessary, excessive compression impedes reactant transport by decreasing GDL porosity and may also damage typical paper type GDLs and other components. These interrelations are highly complicated, however, an optimum compression pressure and compressed thickness (more concretely, gasket thickness), which trades off these competing issues, has to be identified for each fuel cell system.

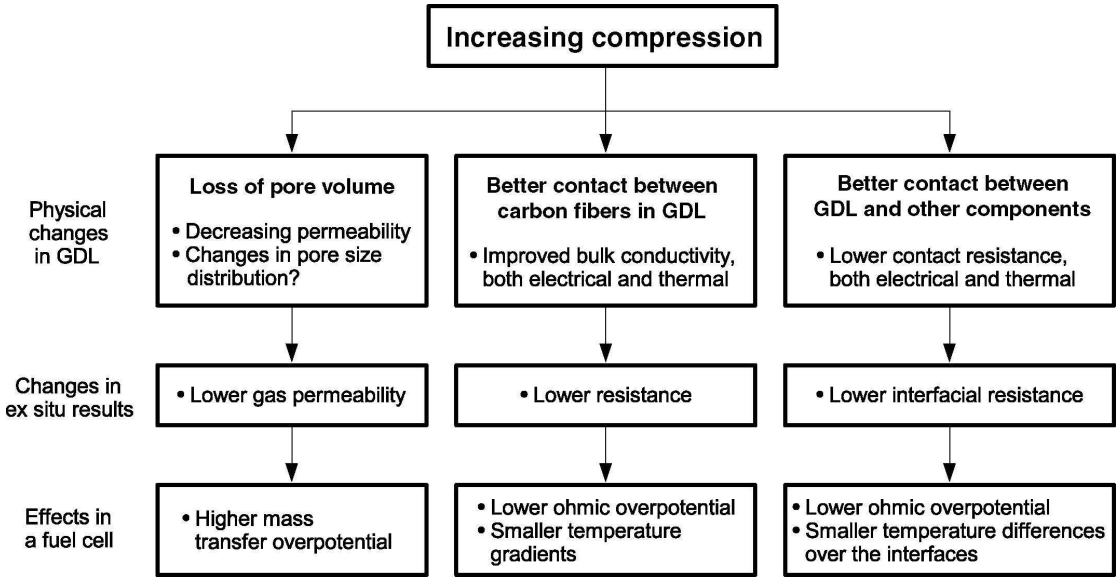

Fig. 10 Flow chart of effects of compression on GDL.

So far, a number of experimental studies on the GDL properties have been conducted on subjects such as production process [99-101], gas and fluid permeability [102-109], electric conductivity [110-114], thermal properties [96,115,116], water transport properties [24-27,67-69,117-119], contact resistance at the interfaces [98,112,113,120-125]. Relating to compression, it has been observed that excessive compression damages the carbon fibers in GDL materials, see, e.g. [122,126,127] as shown in Fig. 11.

However, in previous studies, the electric conductivities have been roughly estimated based on the initial thickness, see, e.g. [112,113]. In electric contact resistance evaluation, the effect of compression on bulk conductivity was neglected, see, e.g. [112,121]. Contact resistance between the GDL and CL, to the authors' knowledge, has not yet been adequately evaluated experimentally and typically estimated with rough assumption or simply overlooked, see, e.g.

[128,129]. As for thermal properties of GDL, very limited experimental data compared to electric properties have been reported in the literature and further studies are necessary. Gas permeability of GDL has been typically measured as a function of external compression pressure. Here it should be noted that the effect of compression on the physical properties of the GDL should be discussed in the light of compressed GDL thickness, although previous experimental studies commonly characterized the physical properties of GDL as a function of compression pressure. This is because correlating any data expressed as a function of compression pressure to conditions inside a fuel cell assembly is not straightforward since the compression pressure exerted onto the GDL depends on the thickness of neighboring gaskets and is different from the cell assembling pressure. In fact, it is the thickness of the GDL compressed to gasket thickness under the rib as well as uncompressed thickness under the channel that are the only parameters one can set in a realistic fuel cell construction, and that determine the GDL's characteristics. Expressions of physical properties as a function of compressed thickness are also convenient for model construction, since one just needs to change the parameters according to the model geometry when the effect of compression is considered. Therefore, the physical properties of GDL were evaluated as a function of its thickness in this study.

In accordance with the experimental studies, significant efforts on modeling studies have also been devoted to exploring the impact of these parameters on the transport mechanisms and fuel cell performance. Examples of the systematic parametric study are found on the electric anisotropy of GDL [130-132], the thickness and porosity of the GDL [12,133-135], pore size distribution [136-138], gas permeability [130,139,140], water transport parameters [20,141,142] geometric parameter of flow field [143-146], operation parameters [10,13,43,146,147] and the effect of compression [144,148-151].

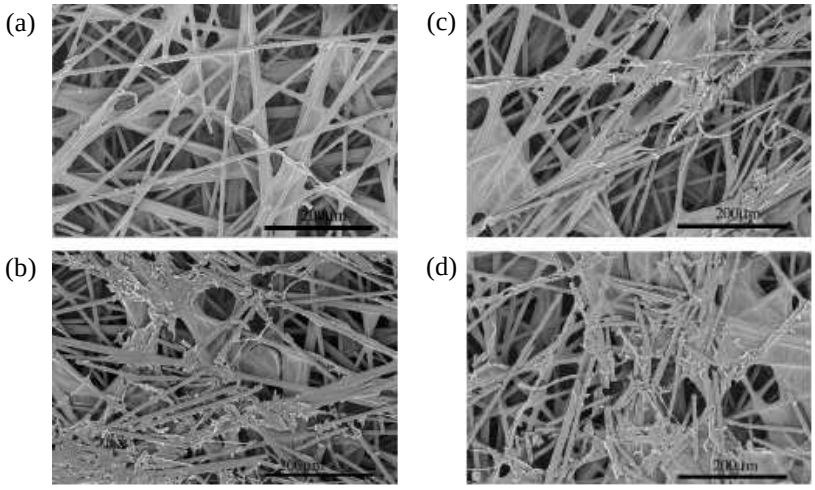

Fig. 11 SEM images of the GDL after it has been compressed for 5 minutes. The carbon fibers are damaged more as higher compression is applied. (a) 0.18 MPa, (b) 0.36 MPa, (c) 0.68 MPa, (d) 1.37 MPa (Figure: taken by Bazylak et al. [118]).

In an actual fuel cell assembly, the compression pressure over the GDL is not homogeneous since the compression force is practically not exerted on the GDL under the channel of bipolar plate. As a consequence, thickness of the GDL varies, i.e. the GDL under the rib is deformed and becomes thinner and the GDL under the channel partially intrudes into the channel as seen in Fig. 12(a). The compressed regions of GDL do not recover to their initial thickness when load is removed because of a residual strain of GDL as seen in Fig. 12(b).

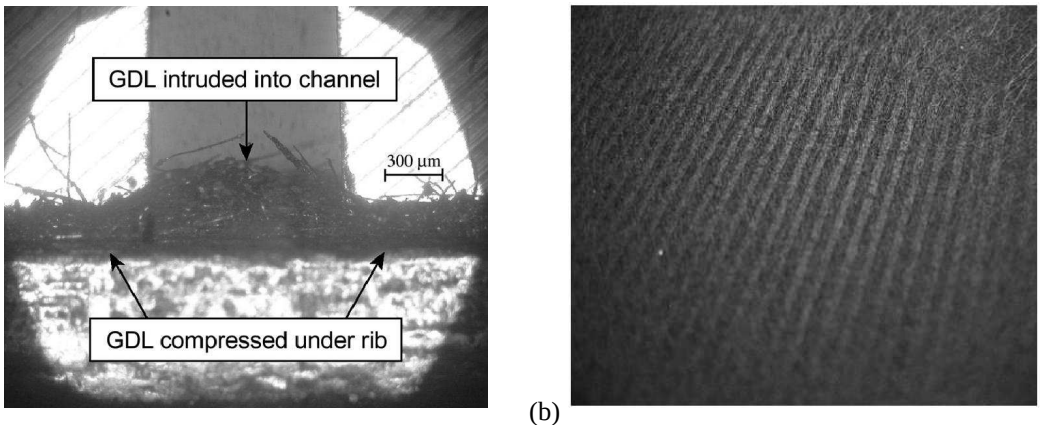

Fig. 12(a) Photograph of inhomogeneous compression distribution of GDL under rib/channel structure (b) Photograph of a GDL after compression (dark striations correspond to GDL under the rib area under compression pressure) (photograph taken by Pharoah et al. [130]).

The inhomogeneous compression pressure leads into spatial variation of GDL and, bulk and interfacial properties. In region under the rib of flow field plate, the gas permeability of GDL becomes lower due to loss of porosity, while its electric and thermal bulk conductivities are improved and cell components have a better contact to each other by the compression, resulting into the decrease of bulk and contact resistance. On the other hand, region under the channel where practically no compression pressure is applied, the gas permeability remains high but both electric and thermal bulk and contact resistance are also higher than those under the rib. These variations in GDL properties significantly affect local transport phenomena, most probably also the water transport, and consequent cell performance and life-time, and therefore, need to be study in sufficient detail.

Partial intrusion of GDL into the channel is also problematic because it causes reactant flow-field pressure drop to increase over that obtained with a carbon-fiber paper, resulting in higher air compressor power requirements. Furthermore, excessive compression and deformation of GDL may result in local delamination of GDL under the channel because of cantilever mechanism as discussed by Lim et al. [97]. If this happens, current and temperature distribution over the active area would be extremely uneven because of significant variation of contact resistance between the GDL and CL.

However, to the authors' knowledge, only a few studies which consider the inhomogeneous compression of GDL can be found in literature, see, e.g. [110,129,149,152,153]. Although their findings are enlightening, many of the adopted modeling parameters are subject to a large uncertainty, i.e. the spatial variations in values of the parameters due to inhomogeneous compression were not properly taken into account. This may cause significant errors in the prediction of modeled results, such as current density distribution and temperature profile.

The effects of inhomogeneous compression exist in all fuel cells with normal flow field plates but are difficult to measured directly due to small scale of the phenomena. Thus, the only available option is to characterize the GDLs *ex situ* and model the effect. In the following, experimentally evaluated GDL parameters as a function of compressed thickness and modeled predictions of the local phenomena are presented.

3.2. Experimental evaluation of GDL properties

A commercial gas diffusion media, SGL SIGRACET® 10 BA carbon paper (made by SGL Carbon Group), was used in the measurements. This media has uncompressed thickness of 380 μm, is treated with 5 %wt PTFE for wet proofing, has no microporous layer, and has relatively high porosity of 88% [154]. Also, a commercial MEA (Gore™ Primea® Series 5510) and isotropic graphite (ISEM-3 grade, Svenska Tanso Ab) were used in all measurements.

3.2.1. Mechanical properties of GDL

The amount of GDL intrusion was measured to know the shape change of GDL under compression. The experimental setup, as illustrated in Fig. 13 consists of steel gages, GDL and two aluminum plates. The thickness of the GDL having area of 1.6 cm^2 was controlled by the neighboring steel gages whose thickness was varied from 150 to 300 μm. A channel was machined into the bottom aluminum plate. The width of channel ranged from 0.6 to 2 mm. The two aluminum plates were clamped together with four 8 mm bolts, using a torque from 0.8 to 1.5 Nm, depending on the desired thickness. GDL intrusion was measured with a dial indicator (ND 221B by Heidenhain Corporation). The measurements were conducted more than ten times for each GDL compressed thickness and measured results were averaged out.

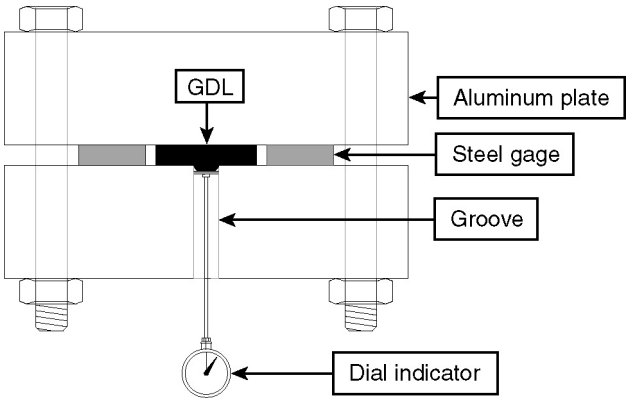

Fig. 13 Schematic illustration of GDL intrusion measurement setup.

The thickness of GDL under the channel, i.e. the sum of the measured GDL intrusion and steel gage thickness, are shown in Fig. 14. It was expected that the channel width may cause a change in GDL intrusion since the mechanical force applied onto GDL is dependent on the geometry of adjacent components (channels and ribs). However, the results indicated that the thickness of GDL under the channel is not strongly dependent on the channel width and/or the thickness of the steel gages, and it remains almost uncompressed. For example, if a 250 μm thick gasket having low compressibility is used, the thickness change of GDL is less than 10 μm under the channel regardless of the channel width.

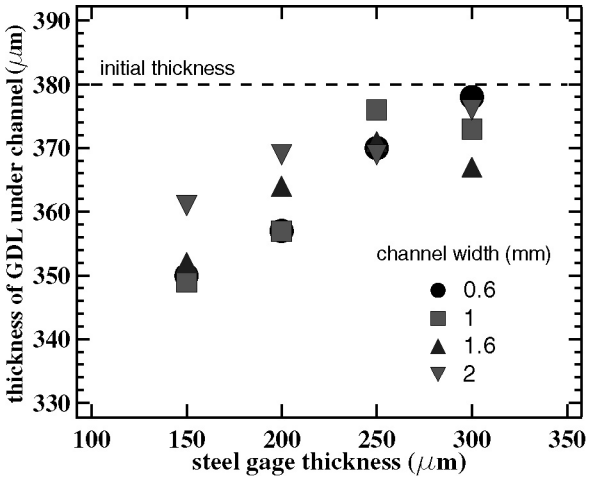

Fig. 14 Thickness of GDL under channel.

The stress-strain behavior of the GDL was measured with the experimental setup illustrated in Fig. 15. Measurements were conducted using 1 to 4 stacked GDLs. Various compression forces were exerted onto the GDL by increasing the loading weight at 0.5 kg steps up to 82 kg, with which the maximum compression pressure was approximately 5.5 MPa. It was found that the more GDLs stacked the longer the interval required to achieve the steady state conditions after the weights were loaded. Therefore, the load was increased at 5 to 20 minute intervals, depending on the number of GDL samples under test. Measurements were repeated five times for each sample area and number of stacked GDLs. The initial deflection of the GDL was found to be fairly susceptible to low compression pressures, probably because of the rough surface of the GDL. Therefore, an additional measurement applying low compression pressures was conducted using a smaller steel rod and lighter weights up to approximately 5 kg (~ 0.1 MPa).

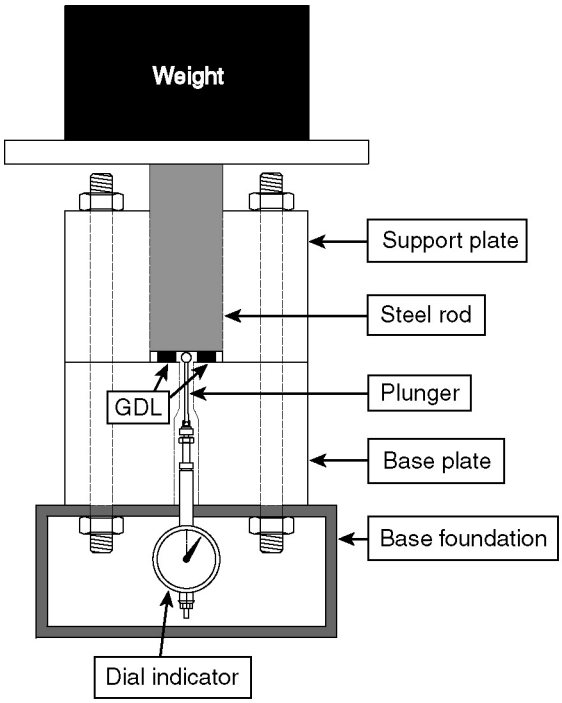

Fig. 15 Schematic of experimental setup for measuring the stress-strain behavior of GDL.

The thickness of uncompressed GDL, which was 380 µm reported by the manufacturer, was determined to be 370 ± 10 µm in a separate measurement with a low compression pressure. This thickness was set as a base point and the stress-strain curve was calculated from the measured thickness-pressure pairs. Fig. 16 shows the stress-strain curves of a GDL, calculated from measurement results with 1 to 4 GDLs. The results from the two separate measurements using low (up to 0.1 MPa) and high compression pressure (0.1 to 5.5 MPa) were ascertained to coincide well. The area of the GDL sample was found not to affect the stress-stain curve as long as the compression pressure was the same.

The most noticeable variations in GDL strain were found with the low compression pressure (~ 0.2 MPa), as reported in literature, see, e.g. [65,106,112,126]. This is most probably due to the smoothening of the rough surface of the GDL. At a compression pressure above 1 MPa, two piecewise linear regions were identified in the range from 1 to 3.5 MPa, and from 3.5 to 5.5 MPa. This was probably because of the nature of the GDL. Typical paper type GDLs have two different pore diameter regions, namely, hydrophobic pores and hydrophilic pores, see e.g. [69,96,119,155]. The first linear region may be associated to the crushing of hydrophobic pores, and the second to the crushing of hydrophilic pores.

Although the curves obtained with different number of GDLs indicated almost identical compressive behavior, the strain of each GDL decreased as more GDLs were stacked. This was most probably due to the fact that stress-strain behavior of the interface of two rough GDL surfaces is different from that of the GDL/graphite interface or bulk GDL. However, the properties of the bulk GDL or interface between the GDL and graphite do not depend on the number of the stacked GDLs. For the purposes of evaluating the thermal properties, when more than one GDLs were used each GDL was assumed to follow the same stress-strain curve.

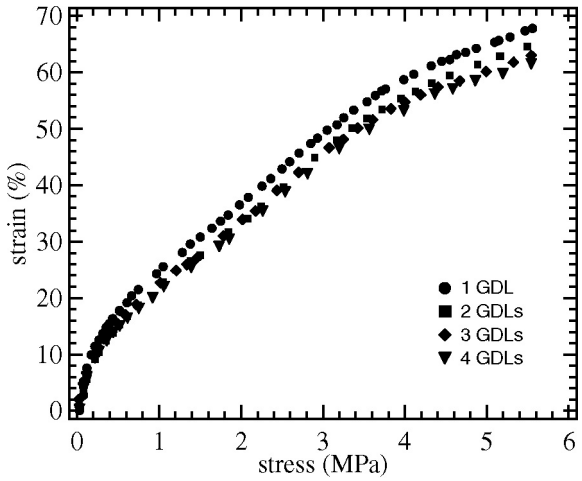

Fig. 16 Stress-strain curve of the GDL measured with different number of GDLs.

3.2.2. In-plane gas permeability

The gas permeability measurement setup allows measuring the pressure drop through GDL with controlling the thickness of GDL. The top view of the measurement device is illustrated in Fig. 17(a), and its cross-section is illustrated in Fig. 17(b) and (c). A circular GDL piece of 30 mm diameter was mounted concentrically on top of the inlet in the steel base plate. Four steel gages were situated in each corner of the base plate in order to enable the precise control of the GDL thickness. The radii of air inlets, r_1, and of GDL, r_2, were 8 mm and 15 mm, respectively. Gas pressure at inlet r_1 was p_1 and the gas pressure p_2 at r_2 was ambient pressure since air was discharged freely to the surroundings.

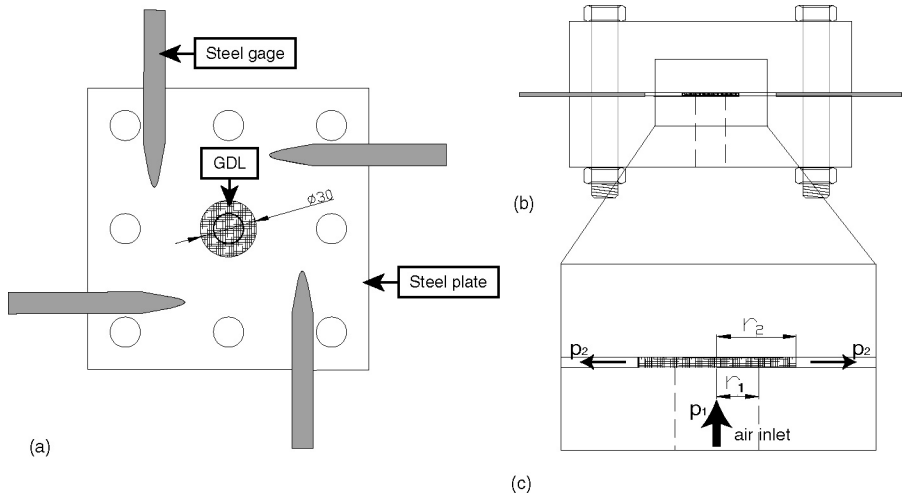

Fig. 17 Gas permeability measurement setup:
(a) top view, (b) cross-section view, (c) enlarged cross-section view.

The measurements were conducted by varying the compressed thickness of GDL from 150 to 350 µm with 50 µm steps controlled by steel gages. The flow rate of flowing fluid: dry air, was varied in the range of 10 to 310 cm^3/min controlled by a mass flow controller (Model 5850S by Brooks Instruments).

The porosity loss in GDL under compression increases the pressure drop and reduces mass transfer. The flow resistance is characterized by the gas permeability, which can be estimated by measuring pressure difference between inlet and atmosphere and by applying Darcy's law:

$$v = -\frac{k}{\eta}\nabla p \tag{9}$$

Where v is flow velocity, k is gas permeability, η is dynamic viscosity and p is pressure. In cylindrical measurement geometry the flow can be assumed to be radially symmetric. By applying conservation of mass and ideal gas law, one can deduce the permeability from Equation (9):

$$k = \frac{\Re T}{\pi V_0}\frac{\eta}{h}\frac{\dot{V}_1}{p_1^2 - p_2^2}\cdot\ln\left(\frac{r_2}{r_1}\right) = \frac{\Re T}{\pi V_0}\frac{\eta}{h}\frac{\dot{V}_1}{(p_m + p_2)^2 - p_2^2}\cdot\ln\left(\frac{r_2}{r_1}\right) \tag{10}$$

where $\dot{V}_1$ is the source volume flow rate, R is the gas constant, T is the temperature, h is the cylinder height (here equivalent to compressed GDL thickness), and V_0 is standard molar volume. The pressure difference was measured with a manometer (Type MM3K by HK Instruments Oy).

Fig. 18 shows the calculated in-plane gas permeability of GDL as a function of compressed thickness. The gas permeability decreased nonlinearly when the thickness of GDL was decreased by compression. The reduction in the permeability was as much as one order of magnitude when the GDL was compressed to approximately 65% (250 µm) of the initial thickness (380 µm). The range of results is in good agreement with those published in literature for typical carbon paper type GDLs.

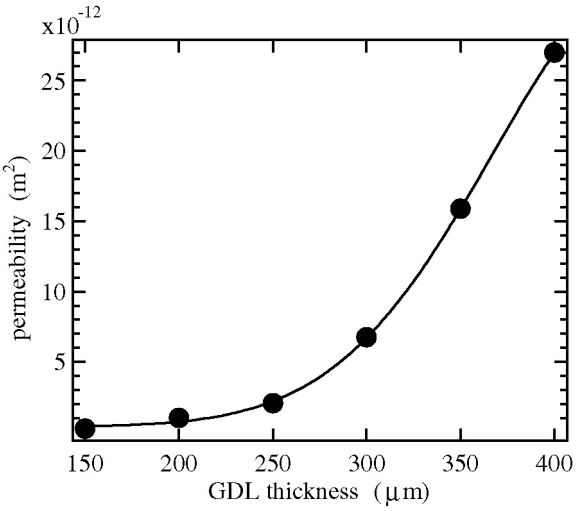

Fig. 18 In-plane gas permeability as a function of compressed thickness of GDL.

In the range where the measurements were conducted, compression of the GDL mainly leads into loss of pore volume, not compression of bulk material. Therefore, porosity can be assumed to correlate directly with compressed GDL thickness. However, most of the previous modeling studies may not directly reflect the realistic situation occurring in a fuel cell since the two above-mentioned parameters were studied separately and their combined effect was basically not considered. In fact, the compressed thickness (and thus porosity) and gas permeability of GDL are closely linked to each other, and it is the combined effect that determines the gas-phase mass transport within the GDL. Furthermore, such parameters as sensitivity to water accumulation, and mass and charge transport resistance are also closely associated with the compressed thickness of the GDL. When ones sets the mass transport parameter in their model, special attentions must be paid, noting that they are nonlinear function of the compressed thickness as shown in Fig. 18.

3.2.3. Electric conductivity of GDL

Evaluation of bulk resistance of GDL $R_{b,GDL}(z)$ separately from the measured resistance $R_{z,meas,conv}(z)$ is not easy task, and the conventional method inherently contains errors in the evaluated values since the measurements are conducted under the wrong assumption that the effect of compression on the bulk conductivity of GDL is simply disregarded. Therefore, a special effort was made, which allows investigation of the compression effect on GDL through-plane bulk conductivity $\sigma_{z,GDL}$ alone.

Two to five pieces of GDLs were placed on top of each other as illustrated in Fig. 19(a). Non-conductive tapes were pasted on graphite current collectors in order to avoid direct electrical contact between the end plates. The thickness of each GDL was controlled by steel gages having thickness from 150 to 350 μm. This means that no matter how many GDLs were used, both the contact resistance between graphite current collector and GDL $R_{c,GR/GDL}(z)$ and $R_{b,GDL}(z)$ were unchanged when the compressed thickness of GDLs was set constant. The total resistance, which is a function of number of GDLs, n, can be expressed as

$$R_{z,meas}(z,n) = 2R_{GR} + n \cdot R_{b,GDL}(z) + 2R_{c,GR/GDL}(z) + (n-1) \cdot R_{c,GDL/GDL}(z) \quad (11a)$$

Where $R_{c,GDL/GDL}$ is the contact resistance between two facing GDLs. If this $R_{c,GDL/GDL}$ can be eliminated from Eq. (11), it reduces into

$$R_{z,meas}(z,n) = 2R_{GR} + n \cdot R_{b,GDL}(z) + 2R_{c,GR/GDL}(z) \quad (11b)$$

Thus, when one plots $R_{z,meas}(n)$ as a function of number of GDLs, the slope of the graph indicates the $R_{b,GDL}(z)$. In order to eliminate $R_{c,GDL/GDL}$, highly conductive silver particles were sputtered onto GDLs. This method was previously shown to successfully reduce the contact resistance [156-158] without significant change in bulk conductivity. In sub-chapter 3.4, the errors caused by the assumptions that silver sputtering treatment reduces the $R_{c,GDL/GDL}$ is discussed.

All GDL surfaces that came into contact with other GDLs were silver coated, but GDL surfaces facing the graphite current collectors were left untreated, which allows to evaluate $R_{c,GR/GDL}(z)$ as discussed below.

The experimental setup used for investigation of in-plane conductivity as a function of compressed thickness of GDL is illustrated in Fig. 19(b). GDL was placed on the base plate and both ends were compressed by graphite current collectors clenched with two 8 mm bolts. Steel gages were inserted between graphite current collectors and base plate, and thus the GDL thickness under the graphite current collector was always fixed to the steel gage thickness of 250 μm. The separation between two current collectors was varied in the range from 1 to 32 mm. A nonconductive plastic plate was placed between the graphite current collectors. This plate allowed the accurate control of the compressed thickness of GDL underneath it and maintained the separation. The thickness of GDL under plastic plate was controlled from 150 to 350 μm with steel gages.

A current in the range from 50 mA to 1 A with 50 mA step was applied and the voltage drop was measured to calculate the total resistance. The measured total resistance $R_{x,meas}(x,z)$ consists of the bulk resistance of graphite current collector R_{GR}, bulk resistance of GDL under the graphite current collector $R_{b,GDL}(250)$ and under the plastic plate $R_{b,GDL}(x,z)$ and the contact resistances between graphite current collector and GDL $R_{c,GR/GDL}$:

$$R_{x.meas}(x,z) = 2R_{GR} + R_{b,GDL}(250) + R_{b,GDL}(x,z) + 2R_{c,GR/GDL} \tag{12}$$

In order to separate the bulk GDL resistance from the total resistance and to investigate the effect of compression, following facts and assumptions should be underlined. First, since the steel gages under graphite current collector fixed the compressed thickness of GDL to 250 μm, both $R_{c,GR/GDL}$ and $R_{b,GDL}(250)$ remained constant through the measurement series. Second, the conductivity of graphite current collector was at least one order of magnitude larger than that of GDL, and therefore the current path within graphite current collector was assumed to concentrate to the edge of the plate and R_{GR} remained constant. And third, since the separation between the graphite plates was at least an order of magnitude larger than the thickness of compressed GDL, it was assumed that the effect of current flowing in through-plane direction from the graphite plates was negligible, allowing us to study only the changes in in-plane direction.

Based on the above facts and assumptions, $R_{b,GDL}(x,z)$ can be derived by subtracting $R_{x,meas}(x)$ from the other measured values with different separations between graphite plates. For example, with two different separation, x_1 and x_2 ($x_1 < x_2$), and with same thickness z_1, the bulk GDL resistance can be calculated from the subtraction of total resistances as

$$R_{x,meas}(x_2,z_1) - R_{x,meas}(x_1,z_1) = R_{b,GDL}(x_2 - x_1, z_1) = R_{b,GDL}(\Delta x, z_1) \tag{13}$$

Then, the in-plane conductivity $\sigma_{x,GDL}(z)$ can be calculated from the bulk resistance as

$$\sigma_{x,GDL}(z) = \frac{1}{R_{x,GDL}(\Delta x, z)} \frac{\Delta x}{z \cdot w} \tag{14}$$

where Δx, z and w are the current collector separation, compressed thickness and width (10 mm in all of the measurements) of the bulk GDL underneath the plastic plate, respectively.

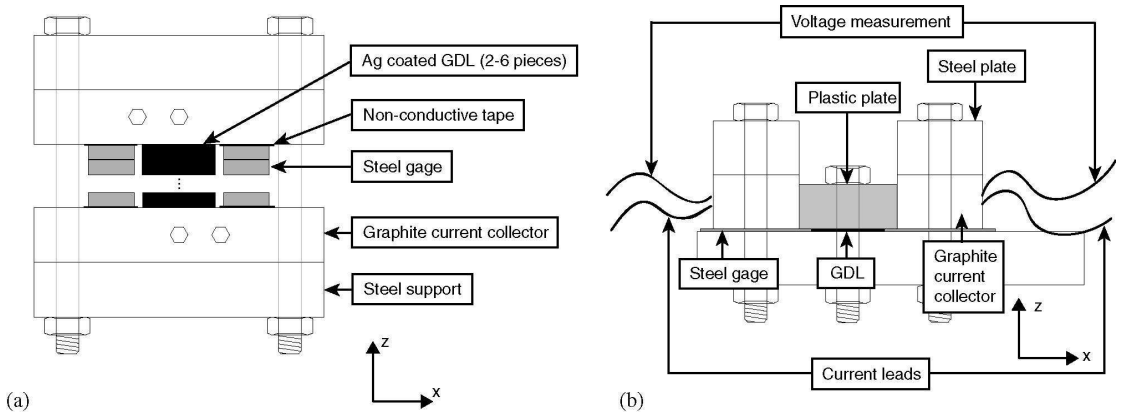

Fig. 19 Experimental setup for (a) through-plane electric conductivity and (b) in-plane electric conductivity.

Fig. 20(a) and (b) illustrate the measured total resistance in through-plane measurement setup as a function of the number of GDLs and the measured total resistance in in-plane measurement setup as a function of GDL length, i.e. the separation between current collectors, respectively. It is obvious from the results that the measured resistances are linear functions in both Fig. 20(a) and (b), and thus the in-plane and through-plane conductivity can be calculated from the linear fits.

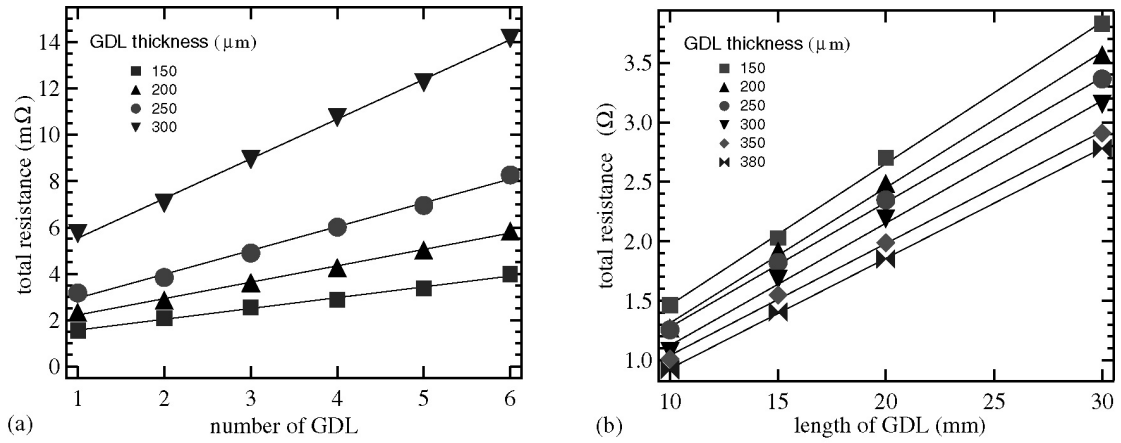

Fig. 20 Measured total resistance: (a) in through-plane direction as a function of number of GDLs, (b) in in-plane direction as a function of length of GDL.

The resulting values for the in-plane and through-plane conductivity of GDL as a function of compressed thickness are illustrated in Fig. 21. The conductivity in in-plane direction was three to four times higher than that in through-plane direction, which is not as large a difference as stated in the literature, see e.g. [65]. The previously reported data for GDL conductivity varies a lot even among paper type GDLs. The reported values range from 5000 to 23000 S/m for in-plane conductivity and from 300 to 1400 S/m for through-plane conductivity. These variations can most probably be attributed to the physical and structural properties of different GDLs such as hydrophobic agent content, fiber diameter, density, areal density and implementation of micro porous layer. Furthermore, the significant difference in the reported conductivities may arise from the drawbacks in measurement setups and inadequate consideration of contact resistance.

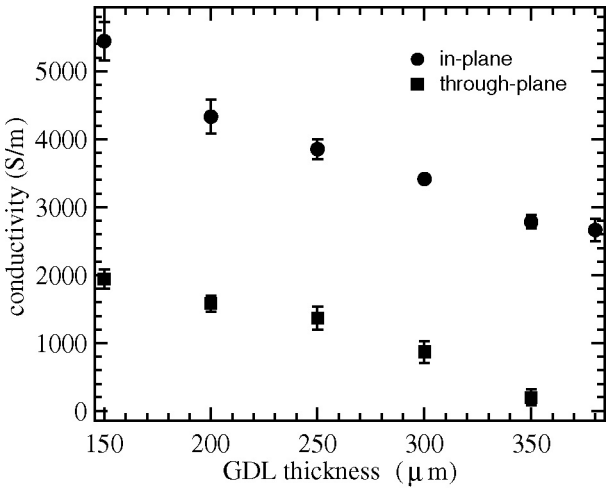

Fig. 21 In-plane and through-plane conductivities as a function of compressed GDL thickness.

Both in-plane and through-plane conductivities monotonically increase as the compressed thickness of GDL was decreased. For example, when the GDL is compressed to a thickness of 250 μm, the in-plane conductivity increased by 160% and through-plane conductivity over tenfold compared to the values of uncompressed GDL. It is interesting to note that the conductivities have practically linear dependence on the GDL compressed thickness. This is possibly because of the reduction of porosity of GDL, which leads into shorter distances between the conductive carbon fibers and also into more and better contacts between the fibers. In an assembled cell, there are significant variations in the GDL thickness between the areas under the flow channels and under the ridges. Therefore, the assumption of constant conductivity may distort modeling results significantly.

3.2.4. Electric conductivity of other components

The conductivities of graphite current collector and CL on MEA were also evaluated by applying four-point probe method. For determining the conductivity of graphite, a graphite block having dimensions of 8×14×90 mm was used. A current lead was connected to both ends of the block and current was applied in the range from 50 mA to 1 A. The potential drop was measured at various positions of the block with distances from 9 to 63 mm. The conductivity of graphite was solved from the subtraction of bulk resistances obtained with various lengths in similar fashion to the in-plane conductivity of GDL as described in Sub-chapter 3.2.3.

In the evaluation of the CL conductivity, the measurement setup was fundamentally the same as illustrated in Fig. 19(b), but the GDL was replaced with a piece of MEA (PRIMEA 5810 by W.L. Gore). The separation between two graphite current collectors was varied from 0.5 to 10 mm and the thickness of CL on MEA was assumed to be 10 μm. Then the same procedure as for the in-plane conductivity of GDL was applied to evaluate the conductivity of the CL.

The conductivities of graphite and CL were 69700 ± 300 and 320 ± 20 S/m, respectively, which were one order of magnitude higher and lower than that of GDL.

3.2.5. Electric contact resistances between GDL and graphite

Finite element method based simulation was employed to solve the contact resistance between graphite current collector and GDL using a commercially available PDE solver program COMSOL Multiphysics 3.2a, since it was believed to be difficult to separate the contact

resistance from total resistance experimentally. The actual measurement geometry was implemented as a 3D modeling domain, which was same as the experimental setup for through-plane GDL conductivity (see Fig. 19(a)). The GDL thickness was changed from 150 to 350 μm in the modeling domain corresponding to the experimental study and the evaluated bulk conductivities of GDL and graphite were embedded.

The electric potentials in graphite, φ_{GR}, and in GDL, φ_{GDL}, were solved in the model. The governing equation for current density follows from the conservation of charge:

$$\nabla^2\varphi = \nabla\cdot(-\sigma_{z,GR}\nabla\varphi_{GR}) = \nabla\cdot(-\sigma_{z,GDL}\nabla\varphi_{GDL}) = 0 \tag{15}$$

Measured potential differences were used as boundary conditions in the model where voltage leads were attached (see Fig. 19(a)).

Since there is a contact resistance between graphite current collector and GDL, the potential profile is discontinuous. This potential drop at the interface can be expressed with current density and the contact resistance. At the graphite current collector/GDL interface, Neumann boundary condition was applied,

$$-\bar{n}\cdot(-\sigma_{z,GR}\nabla\varphi_{GR}) = \frac{\varphi_{GR}-\varphi_{GDL}}{R_{c,GR/GDL}} \tag{16}$$

where $\bar{n}$ is the normal vector of the interface. After solving the potentials, the total current, I, passing through the system was calculated by integrating the local current density. $R_{c,GR/GDL}$ was evaluated by changing its value in the model until the total current corresponded to the measurement result. The same modeling procedure was applied to a system that consisted of various numbers of GDLs in order to find an error estimates for contact resistance.

The area-specific contact resistance between graphite current collector and GDL simulated by applying the conductivities presented above is given in Fig. 22. Error estimates were obtained by conducting the simulations again with considering variations in measured voltages and calculated conductivities. The contact resistance changed exponentially as a function of compressed thickness of GDL. Contact resistance values decreased by two orders of magnitude from very little compression (350 μm) to high compression (150-250 μm). This result is most probably due to the fact that the actual contact area of the GDL at the interface increased with compression pressure.

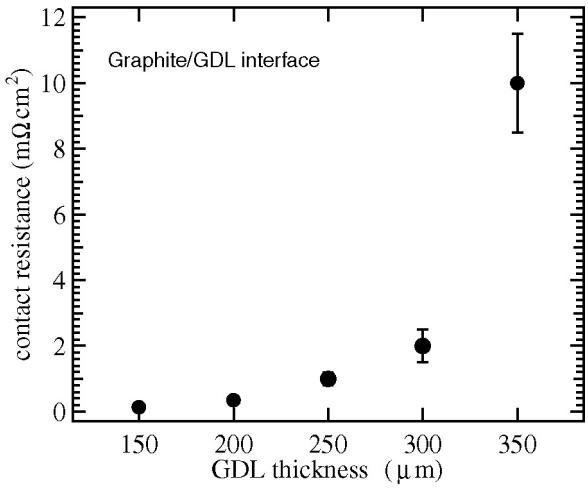

Fig. 22 Contact resistance as function of compressed thickness of GDL.

There is a vast amount of literature discussing the contact resistance values, varying a lot in the range of 1-50 mΩcm^2 with moderate compression pressure (0.5-2 MPa). This large variation and difference from the values achieved in this study may be attributed to the fact

that in the previous studies, the bulk resistance of the GDL and current collector was typically underestimated or simply disregarded, which in turn lead into overestimation of the contact resistance. The bulk resistance of current collector particularly has been assumed to be negligibly small because of its high conductivity (69700 ± 300 S/m in this case) in comparison to that of GDL materials, which also is often the case. However, the thickness of current collector is also almost one order of magnitude larger than that of GDL because of the structure of flow field, which is typically constrained to the millimeter scale. Thus, one can not doubtlessly assume that the voltage drop in graphite current collector is small enough to be neglected in these measurements. Hence, it was worth investigating how significantly the bulk resistance of graphite affected the charge transport.

The electric potential profile achieved from the simulations is plotted from top to bottom at the center of x-y plane of the modeled domain (the through-plane measurement system, see Fig. 19(a)) in longitudinal direction, as depicted in Fig. 23(a). In order to be able to distinguish the potential drop at the interfaces and in the bulk GDL, the enlarged potential profile in the region around the interface is illustrated in Fig. 23(b). According to Fig. 23(a), it is obvious that the gentle potential drop inside 1 cm thick graphite current collector at both ends ($2 \cdot \Delta\varphi_{GR}$) is comparable to that caused by contact and bulk GDL resistances. It is worth noting that especially at the highest GDL compression $2 \cdot \Delta\varphi_{GR}$ accounts for the dominant part of total potential drop. Hence, the resistance of current collector must be also taken into account properly when evaluating the contact resistance values in order not to distort the results. This is especially the case if the current collectors used in the measurements have lower conductivity than graphite, such as carbon compounds or polymer/graphite composites.

The potential drops caused by different factors and their relative significance are summarized in Table 2. The ratios of potential drop caused by two contact resistances and bulk GDL resistance to measured total resistance $\Delta\varphi_{meas}$, $2 \cdot \Delta\varphi_{Rc}/\Delta\varphi_{meas}$ and $\Delta\varphi_{GDL}/\Delta\varphi_{meas}$, respectively, are also tabulated in Table 2. Both $2 \cdot \Delta\varphi_{Rc}$ and $2 \cdot \Delta\varphi_{Rc}/\Delta\varphi_{meas}$ increased as the compressed thickness of GDL was increased. However, it should be noted that $2 \cdot \Delta\varphi_{Rc}/\Delta\varphi_{meas}$ was unexpectedly small, whereas many sources claim that the contact resistance accounts for the major part of the total resistance, see, e.g. [98,111-113]. The results presented here highlight the fact that the contact resistances cause the major contribution to the total resistance only when the GDL is very little compressed.

These results also indicate that the bulk resistance of the GDL can make a significant contribution into the total resistance, while contact resistance was found to be smaller than previously reported. Furthermore, the effect of compression on bulk resistance can not be neglected in the evaluation of the contact resistances. Since the bulk conductivities of GDL changed linearly with compressed thickness as shown in Fig. 21, the method used in previous studies, in which bulk conductivities are assumed constant may not yield proper values for contact resistance.

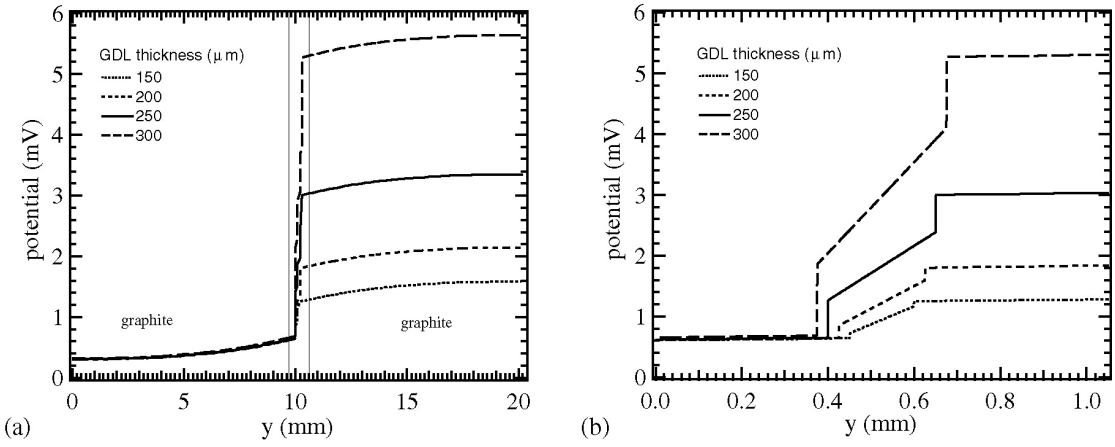

Fig. 23 Potential profiles within the model domain in longitudinal direction:
(a) whole system, (b) enlarged around the GDL.

Table 2 Predicted voltage drops at bulk and interfaces, and percentage of them from the total measured voltage drop.

Thickness (μm)	Potential drop (mV)			Ratio (%)	
	$2\cdot\Delta\varphi_{Rc}$	$\Delta\varphi_{GDL}$	$2\cdot\Delta\varphi_{GR}$	$2\cdot\Delta\varphi_{Rc}/\Delta\varphi_{meas}$	$\Delta\varphi_{GDL}/\Delta\varphi_{meas}$
150	0.17	0.44	0.67	8.8	23.3
200	0.42	0.74	0.67	17.1	30.4
250	1.23	1.12	0.67	33.6	30.7
300	2.35	2.24	0.67	39.4	37.6
350	6.90	6.04	0.67	51.2	44.9

3.2.6. Electric contact resistance between GDL and CL

Experiments were based on AC impedance spectroscopy in a symmetrical H_2/H_2 cell. The AC impedance method has been widely used for analysis of electrochemical systems and is suitable to comprehend the complicated processes involved in operation of a PEM fuel cell [39,53,159-162]. The H_2/H_2 cell can be used to study phenomena occurring in a PEM fuel cell, see e.g. [162-167]. In H_2/H_2 cell hydrogen is fed into both the anode and cathode compartments. The anode and cathode reactions of a H_2/H_2 cell are:

$$H_2 \rightarrow 2H^+ + 2e^- \text{ (anode)} \quad (17)$$

$$2H^+ + 2e^- \rightarrow H_2 \text{ (cathode)} \quad (18)$$

Since the electrochemical kinetics of the reaction in Eq. (18) is substantially faster than that of the oxygen reduction reaction, the activation overpotential is small, which makes the AC impedance measurement easier and helps in obtaining accurate results. Furthermore, since the heat production by the reaction in this system is smaller than in PEM fuel cell systems, the H_2/H_2 cell can be assumed isothermal. This is important since membrane properties such as water uptake and proton conductivity depend on temperature [51,53]. Other advantage in the H_2/H_2 cell is that because there is no water production in this system the water content of the cell can be accurately controlled by reactant humidification conditions. When membrane parameters can be assumed constant the contact resistance between the GDL and CL can be calculated by subtracting the membrane resistance and other bulk and contact resistances from the total cell resistance.

The schematic of the measurement system and the H_2/H_2 cell employed in this study are illustrated in Fig. 24(a) and (b), respectively. The H_2/H_2 cell consisted of the cell body and two cylindrical graphite current collectors, between which the MEA and circular GDLs with a diameter of 8.5 mm were placed. The current collectors could move in the cell frame, allowing separation of sealing pressure onto the gaskets and compression onto the active cell area. To achieve uniform compression on the GDLs and MEA, the current collectors were not grooved, i.e. there were no gas channels. Hydrogen was humidified in a commercial humidification unit (Fuel Cell Technologies, Inc.) and entered the cell from the inlet hole located in the center of the current collector, spread radially from the center and exited through the outlet located at its outer edge. The cell temperature was set to 40 ˚C and controlled using a West 6100 controller, four heating elements (Watlow EB) inside the cell frame and K-type thermocouples in the current collectors.

Prior to the AC impedance measurement, the cell was run in fuel cell mode to ensure gas tightness. The AC impedance spectra were recorded with an impedance spectrum analyzer (Zahner IM6 Electrochemical Workstation) and potentiostat (Zahner PP240 Power Potentiostat) by sweeping the frequency from 500 mHz to 20 kHz. The measurements were conducted in galvanostatic mode with 20 mA amplitude and 0 mA DC-level. After the AC impedance spectra were obtained, the compression pressure onto the active area was

increased stepwise from 0.66 to 4.7 MPa and the same procedure was repeated. Recording the AC spectrum was repeated five times for each compression pressure.

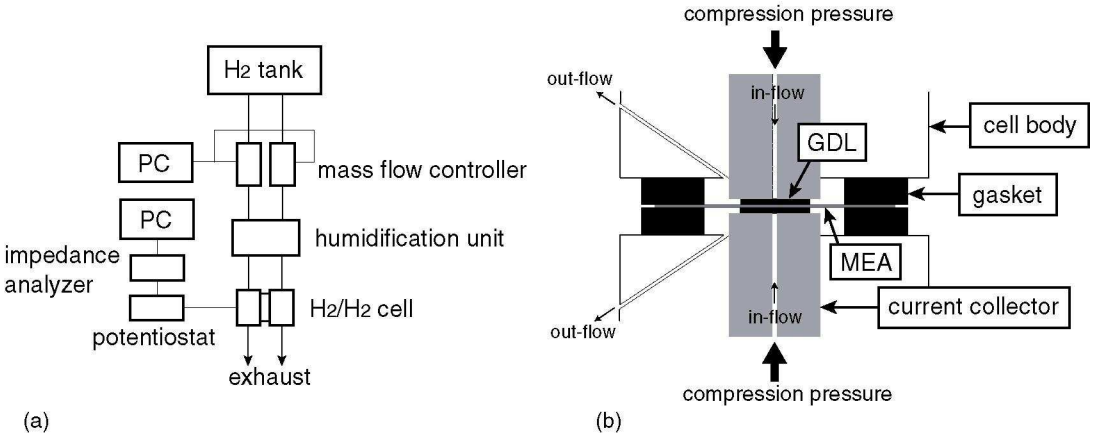

Fig. 24 Schematic of measurement system (a) whole system, and (b) enlarged H_2/H_2 cell.

Fig. 25 shows a typical example of the Nyquist plot obtained from the AC impedance measurement with various compression pressures onto the active area. The high frequency arc is associated with the charge transfer across the catalyst interface and the low frequency arc is attributed to both adsorption and desorption of hydrogen on the electrode surface and water transport in the membrane [162,165,167]. The real axis intercept of the impedance spectrum at high frequency indicates the total cell resistance, R_{cell}. Only the R_{cell}, which includes the bulk resistances of MEA, GDL and graphite current collectors, and the contact resistances between the components, is needed here. The measured impedance spectrum, as expected, shifted to the left as higher compression pressure was applied, indicating a decrease of the R_{cell}. The measurements with different inlet hydrogen humidities showed that the membrane was fully humidified and the measurements were repeatable (see Fig. 25).

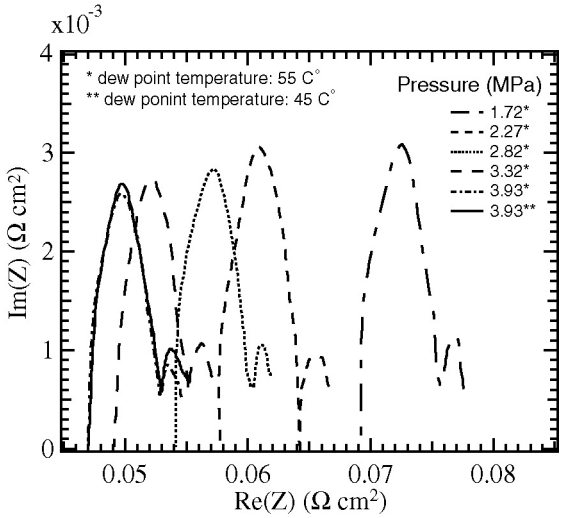

Fig. 25 Impedance curves measured with compression pressure of 1.72-3.93 MPa on the active area.

The compression pressure applied to the active area was converted to the compressed GDL thickness, based on a study of mechanical properties of the GDL (see sub-chapter 3.2.1). The obtained R_{cell} as a function of compressed GDL thickness and compression pressure on the active area is illustrated in Fig. 26. Fig. 26 also includes the negligibly small contact resistance between the GDL and graphite current collector, $R_{c,GR/GDL}$, and the bulk GDL

resistance, $R_{b,GDL}$, which were evaluated in a previous study (see sub-chapters 3.2.3 and 3.2.4), and the membrane resistances R_m calculated as described below.

The R_{cell} decreased nonlinearly as the GDL was compressed due to the reduction of contact resistances between the GDL and CL, $R_{c,GDL/CL}$. The error estimate of R_{cell} was obtained by repeating the measurement and represents the 90% confidence limit when the applied compression pressure to the active area exceeded 1 MPa. However, the error limits were larger at the lowest compression pressure of 0.66 MPa, because R_{cell} was found to be fairly susceptible to the assembling process when low compression pressures were applied.

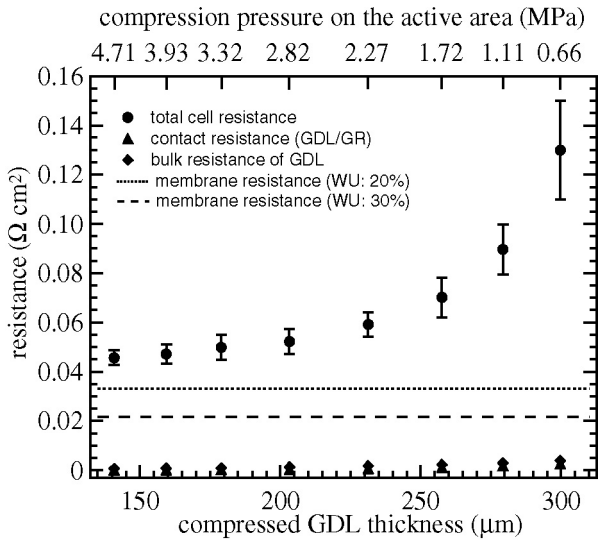

Fig. 26 Resistance as a function of compressed GDL thickness.

Since the water uptake of the membrane from saturated water vapor and liquid water are significantly different [28,52,168], values of conductivity for membrane humidified with water vapor [29] could not be used for the calculation of the R_m in this study, where severe flooding was occurred in the cell. Therefore, the membrane conductivity was calculated from the assumed water content of the membrane, λ. λ is defined as the number of water molecules per sulfonic acid group (λ = mol H_2O/ mol $SO_3^-H^+$) and can be calculated from

$$\lambda = \frac{WU \cdot EW}{M_w} \tag{19}$$

where *WU* is the water uptake of the membrane defined as the mass of water in the membrane divided by the mass of dry membrane (*WU* = kg H_2O/kg dry membrane), *EW* is the equivalent weight of the membrane defined as the weight of membrane per mole of sulfonic acid groups (*EW*= kg membrane/mol $SO_3^-H^+$) and M_w is the molar mass of water.

The published values of *WU* have considerable variation. The *WU* of 32% measured by Kolde et al. [169] may be too high compared to the case in this measurement, because their membrane was equilibrated with boiling water, which lead to higher *WU* values than those when the membrane was soaked in water at lower temperature as reported by Springer et al. [170]. Another possible reason for the high *WU* value measured in [169] is that they used a plain membrane and not a MEA as in this study. As observed by Matic et al. [163], water content in the membrane with CLs is highly uneven, which may yield substantially different *WU* values compared to the plain membrane. This is because the CL is usually hydrophobized to enhance the water removal, and therefore, the measurement may give a lower value of *WU* for a membrane with CL. On the other hand, the *WU* of 10% for the MEA measured by Himanen et al. [166] was so small that the calculated membrane resistance exceeded the total

cell resistance in Fig. 26. This was most probably due to the inaccuracies in the measurement. Based on above review of literature, the value of *WU* was assumed to be between 20 and 30%. Using these values of *WU* and the value of *EW* given by the manufacturer, 1.1 Kg mol^{-1} [169], the λ was calculated to be between 12.2 and 18.3.

The membrane conductivity, σ_{mem}, which is a function of the water content λ and the temperature, *T*, can be calculated with the empirical equation for a Nafion membrane [170] with a correlation for the Gore membrane [80],

$$\sigma_{mem} = 100(0.005139\lambda - 0.00326)\exp\left[2222\left(\frac{1}{303} - \frac{1}{T}\right)\right] \tag{20}$$

Eq. (20) yields the σ_{mem} to be 7.5 and 11.5 S m^{-1} with the *WU* value of 20 and 30%, respectively. The area-specific resistance of membrane was then calculated with fixed thickness of membrane, 25 µm. The membrane swelling due to water uptake was not considered here. Furthermore, the R_m was assumed to independent of the compression pressure. The area-specific resistance of bulk CL and graphite current collector was ascertained small enough (see sub-chapter 3.2.4.) and neglected.

The results for $R_{c,GDL/CL}$ which were obtained by subtraction of the $R_{c,GR/GDL}$, $R_{b,GDL}$ and R_m from the R_{cell} are shown in Fig. 27. The error bars of the $R_{c,GDL/CL}$ were calculated based on the error estimates of the measured total cell resistances and the variation in the membrane resistance calculated with two different *WU* values. The values of $R_{c,GDL/CL}$ changed nonlinearly from 44 to 7.8 mΩ cm^2 when the GDL was compressed from 300 to 140 µm thickness, which are approximately from 14 to 60 times larger than the $R_{c,GR/GDL}$. This is most probably due to the presence of non-conductive material in the CL and the poor contact between the GDL and CL. Compared to a value of $R_{c,GDL/CL}$ reported by Makharia et al. [171], the values obtained here are more than 10 times larger. This is most probably because they used a GDL coated with an MPL, which reduces the $R_{c,GDL/CL}$, see e.g. [65]. Fig. 27 also includes the ratio of two of $R_{c,GDL/CL}$ to R_{cell}. The $R_{c,GDL/CL}$ is the dominant part of the R_{cell} and quite comparable to the R_m, especially when the small compression pressure was applied. Even with the very high compression pressure at which the GDL was compressed to 40% of the initial thickness, the $R_{c(GDL/CL)}$ accounts for 35% of the R_{cell}. These results indicate that the $R_{c,GDL/CL}$ can not be neglected.

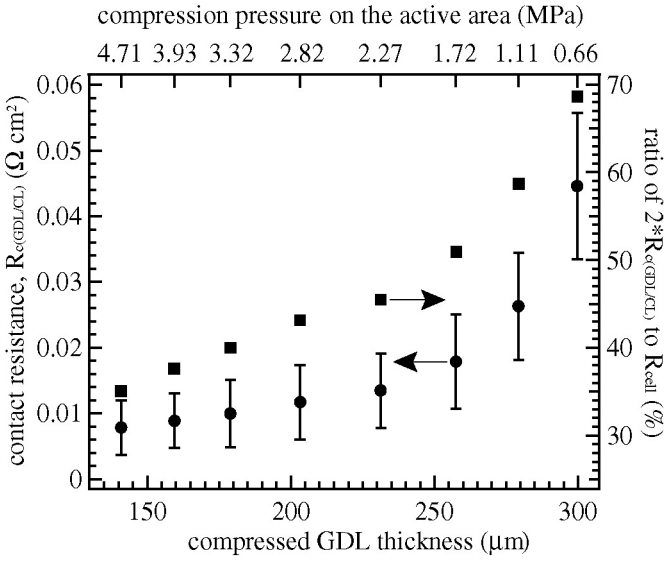

Fig. 27 Contact resistance between the GDL and CL, and ratio of two of the contact resistance to total cell resistance.

3.2.7. Thermal conductivity of GDL

Fig. 28 shows the experimental setup for measuring the thermal properties of the GDL. Heat flux from the heating element (Watlow Metric FIREROD® Cartridge) embedded in the lower graphite rod transferred from the lower rod to the upper rod through the GDL(s) between them. The graphite rods were constructed so that the end facing to the GDL had a smaller diameter of 20 mm and the rod diameter is 38 mm. The graphite rods and GDL samples were thermally insulated from the surroundings by a PVC tube and polystyrene insulator. The temperature of the upper end of the upper graphite rod was maintained at approximately 16 C° by a cooling block (Thermaltake CL-W 0087) through which coolant fluid flowed. A thermostat (Lauda RE 310 chiller with a Lauda E 300 controlled head) was used to control the coolant temperature and flow. This system allowed constraining the heat dissipation in radial direction and thus, a nearly one-dimensional heat transfer in longitudinal direction was achieved.

GDL samples having an area of 144 mm^2 were placed onto the lower graphite rod. The fixture accommodated 1 to 5 stacked GDL pieces. Measurements were conducted with various compression pressures by changing the weight loaded ranging from 4.7 to 77.8 kg. Corresponding compressed GDLs thicknesses were calculated using the measured stress-strain curve (see Fig. 16). Temperature probes (Labfacility Pt100/1528 Class A) were located at four points (‘A’, ‘B’, ‘C’ and ‘D’ in Fig. 28) in the upper and lower graphite rods. Furthermore, an additional temperature probe ‘E’ was installed in the upper graphite rod in the vicinity of the cooling block to measure the temperature at the graphite rod/cooling block interface. Temperature readings were recorded every 5 seconds with a data logger (Agilent 34970A) until steady-state conditions were achieved. That took typically more than 5 hours.

In order to accurately determine the heat flux transferred through the graphite rods, Q_{GR}, a separate measurement was conducted. The experimental system of this measurement is fundamentally similar to the one shown in Fig. 28, with the exception that the two graphite rods and the GDLs in Fig. 28 were replaced by one long graphite rod, into which temperature probes were embedded. The Q_{GR} was calculated from Fourier’s law using the known thermal conductivity of graphite, 128 W m^{-1} K^{-1}, and the temperature drop measured with the temperature probes. For quantitative analysis, two different heating powers were applied, 4.05 and 5.24 W.

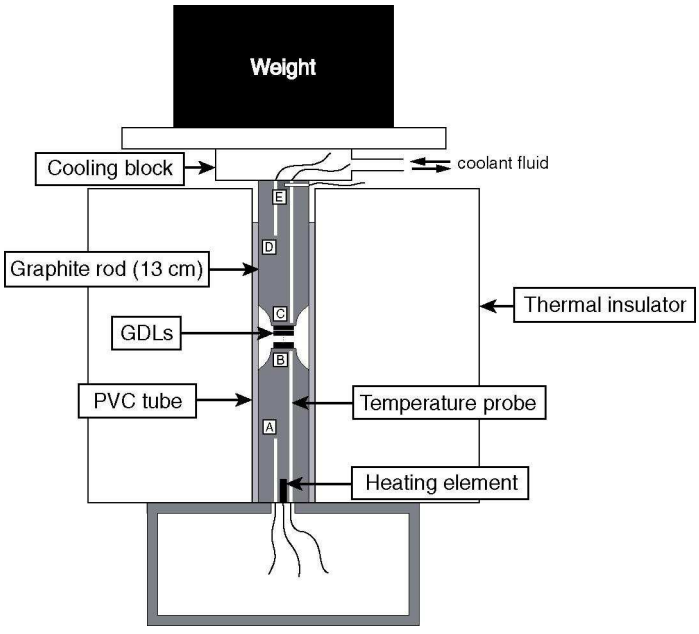

Fig. 28 Schematic of thermal properties measurement system.

As discussed previously, changing the compression pressure leads into changes in both electric contact resistance and electric bulk resistance of GDL. This correlation between compression and resistances was expected to hold true also for thermal resistances because of the analogy of electric and heat transfer. Therefore, the authors applied the experimental technique of the previous study to derive the thermal bulk conductivity and thermal contact resistance separately.

The measured temperature drop between points 'B' and 'C' (Fig. 28), $\Delta T_{B\text{-}C}$, is a function of the number of GDLs, n, and the compressed GDL thickness, h, and is expressed as

$$\Delta T_{B-C}(h,n) = \left(2\Gamma_{c,GR/GDL}(h) + (n-1)\cdot\Gamma_{c,GDL/GDL}(h) + n\cdot\Gamma_{b,GDL}(h)\right)\cdot Q_{GDL} + 2\Gamma_{b,GR}\cdot Q_{GR} \quad (21)$$

where $\Gamma_{c,GR/GDL}(h)$ denotes the thermal contact resistance between the GDL and graphite rod, $\Gamma_{c,GDL/GDL}(h)$ the thermal contact resistance between two GDLs, $\Gamma_{b,GDL}(h)$ the thermal bulk resistance of GDL, $\Gamma_{b,GR}$ the thermal bulk resistance of the graphite rod. The heat flux through the GDL, Q_{GDL}, was calculated from GDL sample area and Q_{GR} based on the assumption that heat transfer from graphite and GDL to the air gap was negligibly small.

To eliminate the thermal contact resistance between the GDLs, conductive silver particles were sputtered onto the GDL surfaces, i.e. same method as used above for electrical contact resistance elimination, with referring process in published literature [158,161]. All GDL surfaces that came into contact with other GDLs were silver coated, but GDL surfaces facing the graphite rods were left untreated to evaluate $\Gamma_{c,GR/GDL}(h)$. This procedure allowed eliminating $\Gamma_{c,GDL/GDL}(h)$ and reducing Eq. (21) into

$$\Delta T_{B-C}(h,n) = \left(2\Gamma_{c,GR/GDL}(h) + n\cdot\Gamma_{b,GDL}(h)\right)\cdot Q_{GDL} + 2\Gamma_{b,GR}\cdot Q_{GR} \quad (22)$$

Thus, plotting $\Delta T_{B\text{-}C}$ as a function of the number of GDLs, the slope of the graph, *S*, gives the value of $\Gamma_{b,GDL}(h)\cdot Q_{GDL}$. The thermal bulk conductivity of the GDL, $\kappa_{GDL}(h)$, can be expressed with $\Gamma_{b,GDL}(h)$ and the compressed GDL thickness *h* as:

$$\kappa_{GDL}(h) = \frac{h}{\Gamma_{b,GDL}(h)} = \frac{h}{S}Q_{GDL} \quad (23)$$

For the calculation of the $\kappa_{GDL}(h)$, the evaluated *h* (see Fig. 16) were used based on the assumption that the values of *h* depend on the compression pressure but not on the number of stacked GDLs.

The measured temperature drops between the points 'B' and 'C', $\Delta T_{B\text{-}C}$, as a function of the number of GDLs are shown in Fig. 29. Fig. 29 includes the $\Delta T_{B\text{-}C}$ when GDL(s) were compressed to various thicknesses, from 328 to 129 µm. When a higher compression pressure was applied and GDL thickness decreased, a lower $\Delta T_{B\text{-}C}$ was observed. This was because both thermal bulk and contact resistances of the GDL decreased with compression pressure. The $\Delta T_{B\text{-}C}$ increased linearly with the number of GDLs.

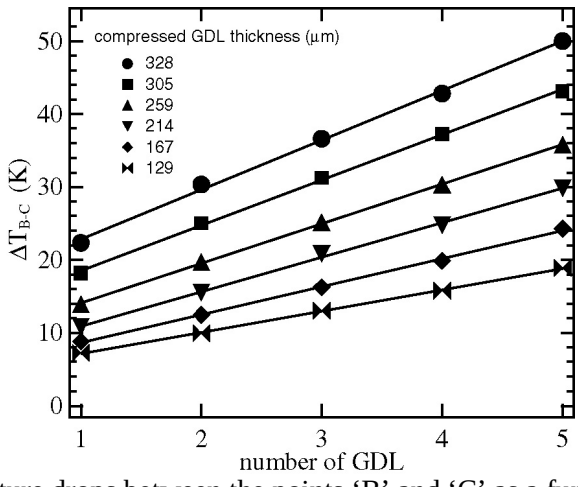

Fig. 29 Temperature drops between the points 'B' and 'C' as a function of number of stacked GDL.

The heat fluxes through the graphite, Q_{GR}, were determined to be 3.33 and 4.45 kW m^{-2} at heating powers of 4.05 and 5.24 W, respectively. The resulting thermal conductivity of the GDL, $\kappa_{GDL}(h)$, as a function compressed GDL thickness is shown in Fig. 30. The error bars shown in the Fig. 30 were estimated considering the following error sources; 1) errors of the measured temperature inside the graphite rods, i.e. the gradient of the $\Delta T_{B\text{-}C}$ in Fig. 29, 2) heat leakage in the radial direction from the system, i.e. change in heat flux passing through the graphite rods and the GDLs, 3) variation in thickness of initial and compressed GDL, and 4) fluctuation in set temperature at the end of upper graphite rod. This analysis was conducted with the method adopted in a previous study [115]. The margins of error shown in the figure represent the 90% confidence interval.

An important finding is that the $\kappa_{GDL}(h)$ does not depend on compression and was determined to be 1.18 ± 0.11 W m^{-1} K^{-1}. It was expected that higher compression pressure would reduce $\kappa_{GDL}(h)$ as observed for electric conductivity, since carbon fibers in the GDL have better contact to each other under compression, and the volume of poorly conducting air in the pores is reduced. However, this was not the case and the interrelation between compression and heat transport through the GDL was found to be different from that between compression and electric transport.

The $\kappa_{GDL}(h)$ obtained here is approximately four times higher than the reported value (0.3 W m^{-1} K^{-1} at approximately 2 MPa) [96,115,116]. This difference is probably due to the fact that in the previous study, the contribution of $\Gamma_{c,GDL/GDL}(h)$ was simply neglected in calculation of $\kappa_{GDL}(h)$ [115] or $\Gamma_{b,GDL}(h)$ was not properly derived from the measured temperature gap [96]. If the $\Gamma_{c,GDL/GDL}(h)$ is not eliminated by e.g. the process implemented in this study, the resulting $\Gamma_{b,GDL}(h)$ will contain also the contact resistances, and thus underestimate the $\kappa_{GDL}(h)$.

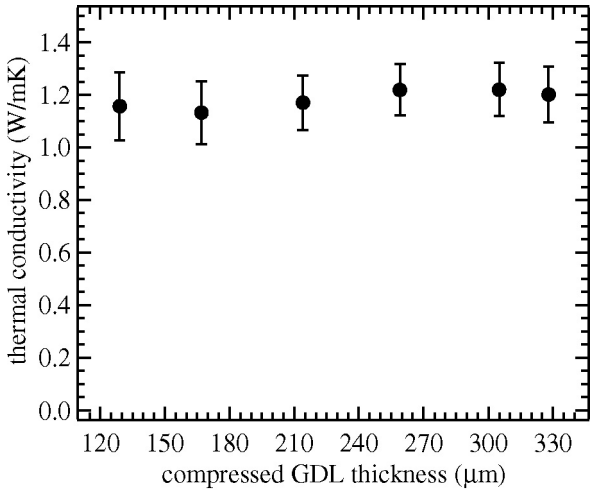

Fig. 30 Thermal conductivity of GDL as a function of compressed GDL thickness.

3.2.8. Thermal contact resistance between GDL and graphite

For determining the thermal contact resistance between the GDL and graphite rod, $\Gamma_{c,GR/GDL}(h)$, a 3D model corresponding to the experimental apparatus (Fig. 28) was constructed using a commercial finite element method solver software (COMSOL Multiphysics 3.2a).

The temperature distribution in the system was solved using the measured values for thermal conductivities and calculated heat flux and varying the GDL thickness from 129 to 328 μm corresponding to the experimental work. The unknown parameter, $\Gamma_{c,GR/GDL}(h)$, was varied until the resulting temperature profile corresponded to the measured one.

The temperature profiles in the graphite rod, T_{GR}, and the GDL, T_{GDL}, were modeled using the governing equation for heat flux which follows from the Fourier's law:

$$\nabla^2 T = \nabla \cdot \left(-\kappa_{GR} \nabla T_{GR}\right) = \nabla \cdot \left(-\kappa_{GDL} \nabla T_{GDL}\right) = 0 \tag{24}$$

It should be noted that the thermal conductivity of the GDL was assumed to be isotropic, i.e. same value in both in- and through-plane directions. Because of $\Gamma_{c,GR/GDL}(h)$, the temperature profile becomes discontinuous. At the GDL/graphite rod interface, a Neumann boundary condition was applied,

$$-\bar{n} \cdot \left(-\kappa_{GR} \nabla T_{GR}\right) = \frac{T_{GR} - T_{GDL}}{\Gamma_{c,GR/GDL}(h)} \tag{25}$$

where $\bar{n}$ is the surface normal vector.

At the boundary between the upper graphite rod and cooling block, a constant temperature boundary condition was applied, using the temperature measured by the temperature probe, 'E' (see Fig. 28). At the graphite rod/PVC tube interface, graphite rod/air interface and GDL/air interface, Neumann boundary conditions were applied for the thermal flux. The thermal contact resistances at the rod/PVC tube interface and heat transfer coefficient at the graphite rod/air and the GDL/air interfaces were based on estimations. They were varied within reasonable limits and ascertained not to affect the temperature distribution significantly. The thermal contact resistance between the PVC and insulator was not included in the model due to negligible effect on the temperature distribution inside the graphite rods.

At the boundary between heating element and graphite rod, a boundary condition for the heat flux from the heating element, Q_{HE}, was applied,

$$-\bar{n} \cdot \left(-\kappa_{GR} \nabla T_{GR}\right) = Q_{HE} \tag{26}$$

The value of Q_{HE} was set so that the temperature profile in a separate model in which one long graphite rod was used matched the experimental results. The same value of Q_{HE} was applied to the model with two graphite rods and GDL, based on the assumption that heat loss in the radial direction was the same in both cases.

The area-specific thermal contact resistance between the GDL and graphite rod, $\Gamma_{c,GR/GDL}(h)$, is shown in Fig. 31. The $\Gamma_{c,GR/GDL}(h)$ decreased nonlinearly as the GDL was compressed. Higher compression increased the actual contact area at the interface between the GDL and graphite, thus decreasing contact resistance. Error estimates were obtained by repeating the simulation with varying the modeling parameters; 1) the thermal bulk resistance of GDL, 2) the heat fluxes, and 3) the measured temperatures.

The $\Gamma_{c,GR/GDL}(h)$ at an approximate compression pressure of 2.2 MPa (compressed GDL thickness of ca. 233 μm), $0.65 \pm 0.18 \times 10^{-4}$ m^2 K W^{-1}, is smaller than the value reported in the literature [115], 1.5×10^{-4} m^2 K W^{-1}. A possible reason for this is that the material in contact with the GDL is different. Khandelwal and Mench used aluminum bronze [115], while graphite was used in this study.

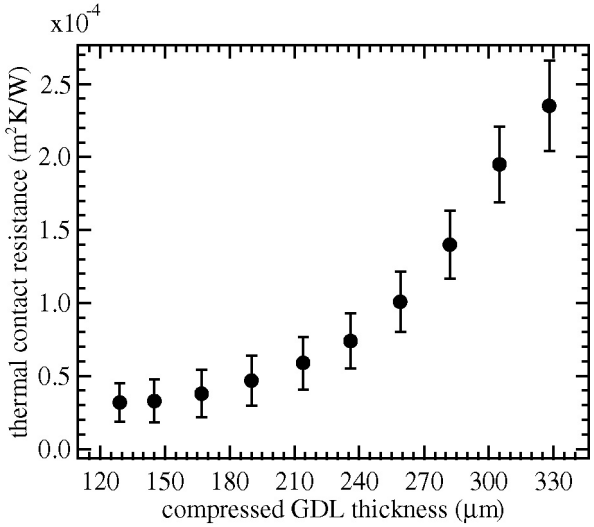

Fig. 31 Thermal contact resistance between GDL and graphite as a function of compressed GDL thickness.

The temperature profiles of the system with various compressed GDL thicknesses obtained from the simulations are plotted in Fig. 32(a), which includes also the measured temperatures at points 'A', 'B', 'C' and 'D' in the graphite rods (see Fig. 28). To clarify the contribution from $\Gamma_{c,GR/GDL}(h)$ and $\Gamma_{b,GDL}(h)$ to temperature drop, the temperature profile in the vicinity of the GDL interfaces is enlarged in Fig. 32(b). It has been often speculated that the interface is a larger source of thermal resistance than the bulk GDL. However, the $\Gamma_{b,GDL}(h)$ accounts for more than 30% of the total thermal resistance of the GDL at low compression and for more than 50% of the total thermal resistance when the GDL was compressed to less than 70% of initial thickness (below 259 μm).

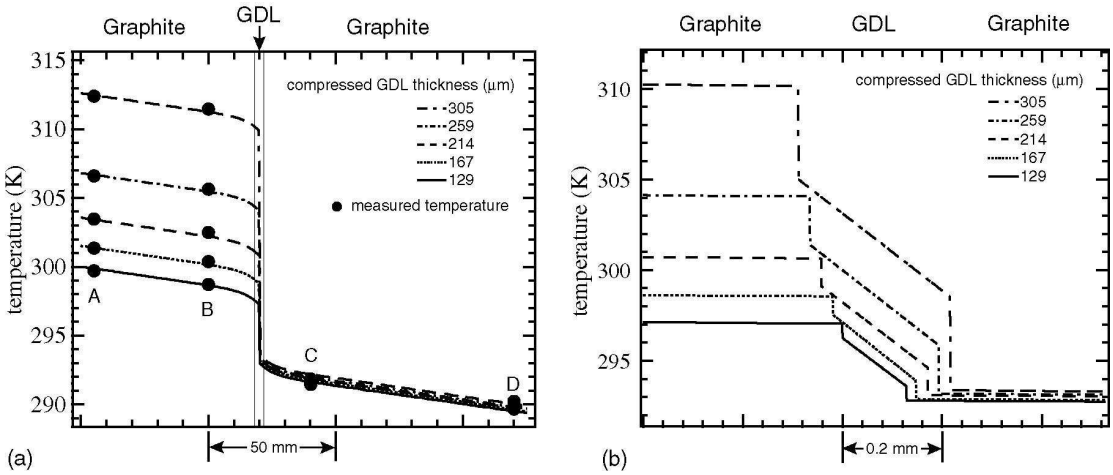

Fig. 32(a) and (b) Modeled temperature profile and measured temperature (a) region around temperature measured point, and (b) enlarged in the vicinity of GDL.

3.3. Modeling analysis

A two-dimensional, one-phase, nonisothermal model was developed to study theoretically the effects of inhomogeneous compression of GDL on the local transport phenomena in a PEM fuel cell. The modeling parameters which were experimentally evaluated and discussed in above subchapter are applied in the model.

3.3.1. Model assumption

Making a theoretically rigorous fuel cell model which reflects the micro- and macro-scale transport processes is extremely challenging because of a lack of experimentally evaluated physical parameters. Therefore, the following assumptions were employed in the model:

(1) Steady state conditions

(2) All gases obey the ideal gas law and are ideally mixed

(3) Water exists only in gaseous form

(4) Anode reaction rate is high enough and anode mass transfer is fast enough

(5) The CL and membrane are isotropic and homogeneous

(6) The membrane is fully hydrated so that ionic conductivity of membrane is constant and no water transport through the membrane are considered

(7) Physical properties of GDL under the rib are constant

(8) Electrodes are assumed to be homogeneous

Because of assumption (3), the model presented here is valid only when the partial pressure of water is below the saturation pressure. Assumption (4) implies that the conservation equations for mass, momentum and species at anode GDL and CL are not solved. Assumption (7) was made since all the experimental work to evaluate the physical properties of GDL was conducted by changing the thickness of the compressed GDL under the assumption that the compression pressure applied to the GDL was uniform.

3.3.2. Model description

The modeled domain is a two-dimensional partial cross-section of a unit cell as shown in Fig. 33, which consists of a half of both the graphite rib and the channel in the flow field plate, two GDLs and CLs, the electrolyte membrane and two thin pseudo layers TH1 and TH2 that represent the contact resistance between graphite and GDL, and GDL and CL, respectively.

The effects of inhomogeneous compression are studied by comparing two models. In the base case, Fig. 33(a), the GDL is compressed evenly and its physical properties are assumed constant. The alternative model, Fig. 33(b), considers the inhomogeneous compression of GDL and the GDL partially intrudes into the flow channel. The deformation curve of GDL observed in the photomicrograph taken with an optical microscope (see Fig. 12(a)) was fitted with a third order polynomial (fitting accuracy: $R^2 = 0.947$) and its dimensionless thickness can be expressed as:

$$h(x) = \begin{cases} h_c \left[\times \mathrm{m}^{-1}\right], & x \le 500\times10^{-6}\,[\mathrm{m}] \\ -1.047\,x^3\times10^6\left[\times \mathrm{m}^{-3}\right] + 2.105x^2\times10^3\left[\times \mathrm{m}^{-2}\right] - 1.070\,x\left[\times \mathrm{m}^{-1}\right] + 3.894\times10^{-4}, & x > 500\times10^{-6}\,[\mathrm{m}] \end{cases} \quad (27)$$

for the case where the compressed GDL thickness, h_c, is 250 μm. The same process was used to obtain expressions for the thickness of the GDL when the h_c was varied from 150 to 300 μm. The dependence of physical properties of GDL on the local thickness is described in the following sub-chapter 3.3.2.3.

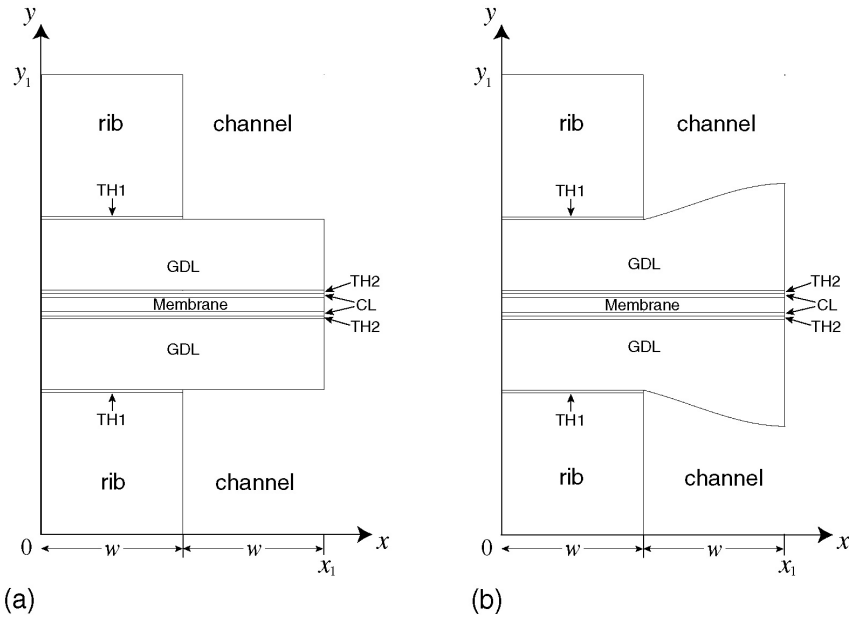

Fig. 33 Modeled domain (a) base case, (b) inhomogeneous compression

3.3.2.1. Governing equations and source terms

The transport phenomena occurring within the cell are modeled with conservation equations for mass, momentum, species, charge and energy. All the governing equations are listed in Table 3. Table 3 also includes the subdomains where the equations are solved.

The Navier-Stokes equation that describes momentum conservation was reduced to Darcy's law since the Reynolds number is less than one and thus the inertia and viscous terms can be neglected in the GDL and CL. Darcy's law was combined with the mass conservation equation which gives Eq. (28) in Table 3. The species conservation equation Eq. (29) is the Maxwell-Stefan diffusion equation and takes into account the convective and diffusive molar fluxes. Since air is fed to the cathode, the multicomponent mass transfer involves a ternary gas mixture (oxygen, water vapor and nitrogen). The charge conservation equations Eqs. (30 and 31) describe the electric current in electrically conductive components and ionic current in ionic conductive components. The energy conservation Eq. (32) takes into account both conductive and convective heat fluxes. Note that on the anode only the charge and energy conservation equations were solved.

Table 3 Governing equations.

	Conservation equation		Subdomains
Mass	$\nabla\cdot\left(-\rho_t\frac{k_{sd}}{\mu_t}\nabla p\right)=S_c$	(28)	cathode (GDL, TH2, CL)
Species	$\nabla\cdot\mathbf{N}_i=\nabla\cdot\left(c_t\mathbf{v}X_i\right)-\nabla\cdot\left(c_t\overline{D}_{eff}\nabla X_i\right)=S_i$	(29)	cathode (GDL, TH2, CL)
Charge (electric)	$\nabla\cdot\left(-\sigma_{s,sd}\nabla\phi_s\right)=S_s$	(30)	rib, TH1, GDL, TH2, CL
(ionic)	$\nabla\cdot\left(-\sigma_{m,sd}\nabla\phi_m\right)=S_m$	(31)	CL, membrane
Energy	$\nabla\cdot\left(\sum_i\rho_i C_{p,i}\mathbf{v}T\right)-\nabla\cdot\left(\kappa_{sd}\nabla T\right)=S_T$	(32)	all

The source terms for the governing equations are listed in Table 4. The source terms of the mass and species conservation equation represent the consumption of oxygen and production of water in the cathode CL. The number of electrons involved in the reaction (4 for oxygen consumption, 2 for water production) appears in the equations. The source terms in the charge conservation equation describe the charge transfer current density between the electric and ionic phases inside the anode and cathode CLs. The transfer current densities are expressed with the Butler-Volmer relation as follows:

$$j_a = -a_v j_a^{ref}\left[\frac{\left(\alpha_a^a + \alpha_c^a\right)F}{\Re T}\eta_a\right] \quad \text{for anode} \tag{33}$$

$$j_c = a_v j_c^{ref,T}\left(\frac{c_{O_2}}{c_{O_2}^{ref}}\right)\exp\left(-\frac{\alpha_c^c F}{\Re T}\eta_c\right) \quad \text{for cathode} \tag{34}$$

Anode side has fast reaction kinetics and low overpotential compared to the cathode, and thus anode transfer current density can be linearized as in Eq. (33). The reference concentration $c_{O_2}^{ref}$ is equal to the concentration of oxygen in air at STP conditions and c_{O_2} is the concentration of oxygen in the CL. In the model, the ratio of c_{O_2} to $c_{O_2}^{ref}$ in Eq. (34), was replaced by the molar fraction of oxygen, X_{O_2}. η_a and η_c are the overpotentials at anode and cathode, respectively:

$$\eta_a = \phi_m - \phi_{s,a} \tag{35}$$

$$\eta_c = \phi_{s,c} - \phi_m - E_0 \tag{36}$$

where E_0 is open circuit voltage.

The source terms in the energy conservation equation correspond to Joule heating, irreversible heat of electrochemical reactions and entropic heat of reactions in CLs but only Joule heating in other subdomains.

Table 4 Source terms in each modeling subdomain.

Region	Mass	Species	Charge	Energy
GDL	0	0	0	$S_T = \sigma_{GDL}(\nabla\phi_s)^2$
CL				
(Anode)	0	0	$S_{s,a} = -j_a$ $S_{m,a} = j_a$	$S_T = \sigma_s^{CL}(\nabla\phi_s)^2 + \sigma_m^{CL}(\nabla\phi_m)^2 + j_a\eta_a + \frac{j_a T\Delta S_a}{2F}$
(Cathode)	$S_c = -\frac{j_c M_{O_2}}{4F} + \frac{j_c M_{H_2O}}{2F}$	$S_{O_2} = -\frac{j_c}{4F}$ $S_{H_2O} = \frac{j_c}{2F}$	$S_{s,c} = j_c$ $S_{m,c} = -j_c$	$S_T = \sigma_s^{CL}(\nabla\phi_s)^2 + \sigma_m^{CL}(\nabla\phi_m)^2 - j_c\eta_c - \frac{j_c T\Delta S_c}{4F}$
TH1, TH2	0	0	0	$S_T = \sigma_{s,sd}(\nabla\phi_s)^2$
Membrane	0	0	0	$S_T = \sigma_m(\nabla\phi_m)^2$

The constitutive relations used for the governing equations are listed in Table 5. The molar density can be calculated from ideal gas law as in Eq. (37). The molar fraction of nitrogen is calculated from the fact that the sum of molar fractions is equal to unity Eq. (38). The effective Maxwell-Stefan diffusion coefficient tensor, $\overline{D}_{eff}$, is related to the non-porous diffusion coefficient, $\overline{D}$, through the Bruggeman correlation as in Eq. (39). The elements of the $\overline{D}$ for a ternary system are calculated from the Maxwell-Stefan binary diffusion coefficients as in Eq. (40). The temperature and pressure dependence of the binary diffusion coefficients was taken into account with Eq. (41). Also, the temperature dependence of exchange current density was taken into account with Eq. (42).

Table 5 Constitutive relations.

Expression		
Ideal gas law	$\rho_t = M_t c_t = \frac{M_t p}{\Re T}$	(37)
Molar mass of gas mixture	$M_t = \sum_i X_i M_i$	(38)
Effective diffusion coefficient tensor	$\overline{D}_{eff} = \varepsilon_{sd}^{1.5} \overline{D}$	(39)
Elements of $\overline{D}$	$D_{11} = D_{O_2,N_2} \frac{X_{O_2} D_{H_2O,N_2} + (1 - X_{O_2}) D_{O_2,H_2O}}{S}$ $D_{12} = X_{O_2} D_{H_2O,N_2} \frac{D_{O_2,N_2} - D_{O_2,H_2O}}{S}$ $D_{21} = X_{H_2O} D_{O_2,N_2} \frac{D_{H_2O,N_2} - D_{O_2,H_2O}}{S}$ $D_{22} = D_{H_2O,N_2} \frac{X_{H_2O} D_{O_2,N_2} + (1 - X_{H_2O}) D_{O_2,H_2O}}{S}$ $S = X_{O_2} D_{H_2O,N_2} + X_{H_2O} D_{O_2,N_2} + X_{N_2} D_{O_2,H_2O}$	(40)
Temperature and pressure dependence of binary diffusion coefficients	$D_{i,j} = \frac{p_0}{p} \left(\frac{T}{T_0} \right)^{1.5} D_{i,j}(p_0, T_0)$	(41)
Temperature dependence of exchange current density	$j_c^{ref,T} = j_c^{ref,T_0} \exp\left[-\frac{\Delta E_{exc}}{\Re} \left(\frac{1}{T} - \frac{1}{T_0} \right) \right]$	(42)

3.3.2.2. Boundary conditions

Symmetry boundary conditions were applied at $x = 0$ and $x = x_1$ in Fig. 33, i.e. all the fluxes were set to zero. No electric current passes through the interface between the GDL/channel and CL/membrane. It was assumed that there is no ionic contact resistance at the CL/membrane interface, and thus the ionic potential and temperature are continuous. On the other hand, ionic current does not pass through the GDL/CL interface since the GDL is not ionically conductive.

The concentrations and pressure are continuous through GDL, TH2 and CL, and no boundary conditions are required at the interfaces. However, there is no mass flux across the rib/GDL and CL/membrane interfaces.

At the cathode gas channel/GDL interface, the pressure was set equal to ambient pressure. The molar fractions of the species at the channel/GDL interface were calculated based on the following assumptions

(1) The modeled cross-section is in the middle of cell and produced current is constant along the channel.

(2) The stoichiometry of air is 2

(3) The air temperature is 325 K and the relative humidity or the air is 40%.

(4) There is no water transport through the membrane

Thus the molar fractions of oxygen and water vapor were fixed to 0.143 and 0.149, respectively.

Furthermore, heat transfer from the GDL to air in the channel is calculated via:

$$-\mathbf{n}\cdot\mathbf{Q} = \kappa_h\left(T_{GDL} - T_{air}\right) \tag{43}$$

where **Q** denotes the heat flux calculated from Eq. (43), κ_h is the heat transfer coefficient, T_{GDL} the temperature of GDL and T_{air} the temperature of air. The temperature of the graphite ribs at $y = 0$ and $y = y_1$ was set to 330 K.

The electric and thermal contact resistances at graphite/GDL and GDL/CL interfaces were converted to corresponding electric and thermal conductivities of TH1 and TH2. Therefore, the electric potential and temperature through cathode rib, GDL and CL are continuous through the TH1 and TH2 and no boundary conditions have to be prescribed.

3.3.2.3. Model input parameters

Table 6 lists the cell design parameters and material, kinetic and electrochemical parameters. When the GDL deformation is taken into account (see Fig. 33(b)), the properties of GDL are varied according to the shape. These changes in GDL physical properties were fitted as a function of compressed GDL thickness as described below and the fitted values were implemented into the model.

Porosity and gas permeability

The reduction of the GDL thickness was assumed to be caused by the reduction of GDL porosity. Therefore, the porosity of the compressed GDL, ε_c, is calculated from the equation, see, e.g [69]

$$\varepsilon_c = \frac{h(x) - h_s}{h(x)} = 1 - \left(1 - \varepsilon_0\right)\frac{h_0}{h(x)} \tag{44}$$

where ε_0 denotes the initial porosity of GDL and h_0 the initial thickness of GDL. h_s is the thickness of the GDL when all the pores are lost:

$$h_s = (1 - \varepsilon_0)h_0 \tag{45}$$

The reduction of GDL porosity leads into a decrease in gas permeability. The experimentally evaluated in-plane gas permeability of the compressed GDL, $k(x)$, was fitted with the curve (fitting accuracy: $R^2 = 0.997$):

$$k(x) = 0.806h(x)^3 - 6.464\times10^{-5}h(x)^2 - 5.305\times10^{-8}h(x) + 7.164\times10^{-12} \tag{46}$$

The gas permeability was assumed isotropic and Eq. (46) was also used for the permeability of TH2. The porosity of CL, ε_{CL}, adopted by Bernardi et al. [172] and permeability of CL, k_{CL}, reported by Himanen et al. [166] were assumed to be not affected by compression.

Electric properties

The electric conductivity was found to be anisotropic and fitted with a straight line (fitting accuracy: $R^2 = 0.964$ for in-plane and $R^2 = 0.975$ for through-plane):

$$\sigma_{\mathrm{GDL,x}} = -1.159\times10^{7}\,h(x) + 6.896\times10^{3}\ [\mathrm{S\ m^{-1}}] \quad \text{for in-plane conductivity} \tag{47}$$

$$\sigma_{\mathrm{GDL,y}} = -8.385\times10^{6}\,h(x) + 3.285\times10^{3}\ [\mathrm{S\ m^{-1}}] \quad \text{for through-plane conductivity} \tag{48}$$

The electric contact resistance between GDL and graphite current collector, $R_{\mathrm{c,GDL/GR}}(h_{\mathrm{c}})$ was converted into through-plane electric conductivity of TH1, $\sigma_{\mathrm{TH1,y}}(x)$. The $\sigma_{\mathrm{TH1,y}}(x)$ was calculated as a function of compressed GDL thickness, and exponential curve was fitted into the data (fitting accuracy: $R^2 = 0.983$), yielding:

$$\sigma_{TH1,y}(x) = 1.714\times10^{4}\exp\left[-2.056\times10^{4}\,h(x)\right]\ [\mathrm{S\ m^{-1}}] \tag{49}$$

The electric contact resistance between the GDL and CL, $R_{\mathrm{c,GDL/CL}}(h_{\mathrm{c}})$, was also converted to the through-plane electric conductivity of TH2, $\sigma_{\mathrm{TH2,y}}(x)$, which was fitted with a third degree polynomial (fitting accuracy: $R^2 = 0.996$), giving

$$\sigma_{TH2,y}(x) = 7.726\times10^{11}\,h(x)^3 - 4.943\times10^{8}\,h(x)^2 + 2.664\times10^{4}\,h(x) + 18.911\ [\mathrm{S\ m^{-1}}] \tag{50}$$

Accurate experimental evaluation of the $R_{\mathrm{c,GDL/CL}}(h_{\mathrm{c}})$ was found difficult as the compression pressure decreased. Therefore, in sub-chapter 3.2.5, the lowest compression pressure at which the $R_{\mathrm{c,GDL/CL}}(h_{\mathrm{c}})$ could be evaluated was 0.664 MPa. This corresponds to a GDL thickness of approximately 300 μm, above which the accuracy of Eq. (50) diminishes. However, the trend is clear – the lower the compression, the higher the contact resistance.

The values used for the in-plane electric conductivity of TH1 and TH2, $\sigma_{\mathrm{TH1,x}}$ and $\sigma_{\mathrm{TH2,x}}$, were set equal to the in-plane electric conductivity of GDL and CL, respectively. These values were adopted because the lateral current flow in the TH1 and TH2 can be expected to follow to that in the neighboring more conductive components, the GDL and CL. On the other hand, the conductivity of CL evaluated previously (see, sub-chapter 3.2.4.) was assumed to be isotropic since no reliable experimental data on its anisotropy was found.

Thermal properties

The through-plane thermal conductivity of GDL was not affected by the compression pressure (see sub-chapter 3.2.7.) and a constant value was used in this model. The in-plane thermal conductivity of GDL was assumed to be the same as the through-plane thermal conductivity.

The evaluated thermal contact resistance between the graphite current collector and GDL (see sub-chapter 3.2.8.) was converted to the through-plane thermal conductivity of TH1, $\kappa_{\mathrm{TH1,y}}(\mathrm{x})$. The calculated $\kappa_{\mathrm{TH1,y}}(x)$ as a function of compressed GDL thickness was fitted with a fourth degree polynomial (fitting accuracy: $R^2 = 0.993$), giving

$$\kappa_{TH1,y}(x) = -2.912\times10^{14}\,h(x)^4 + 3.133\times10^{11}\,h(x)^3 - 1.170\times10^{8}\,h(x)^2 + 1.639\times10^{4}\,h(x) - 0.438\ [\mathrm{W\ m^{-1}\ K^{-1}}] \tag{51}$$

The thermal contact resistance between the GDL and CL was assumed to be same as the thermal contact resistance between graphite and GDL. Therefore, Eq. (51) was used also for the through-plane thermal conductivity of TH2, $\kappa_{\mathrm{TH2,y}}(\mathrm{x})$. The in-plane thermal conductivities of TH1 and TH2, $\kappa_{\mathrm{TH1,x}}$ and $\kappa_{\mathrm{TH2,x}}$, were set equal to the in-plane thermal conductivity of GDL and CL, respectively, based on the same assumption of charge transport at the interface.

The thermal conductivity of CL was calculated from the data reported by Khandelwal et al. [115]. In their study, the combined thermal resistance, i.e. thermal bulk resistance of the CL plus thermal contact resistance between GDL and CL, was determined to be 1.25×10^4 m^2 K W^{-1} at a compression pressure of 1.83 MPa (compressed GDL thickness of ca. 250 µm, see sub-chapter 3.2.1.). By subtracting the thermal contact resistance between GDL and CL, which can be calculated from Eq. (51), from the combined thermal resistance, the thermal bulk resistance of CL was determined. The thermal conductivity of CL, κ_{CL}, calculated using the measured thermal bulk resistance of CL was assumed to be isotropic and independent of compression.

Table 6 Cell design parameters and material properties for base case.

Symbol	Description	Value
Geometrical parameters		
w	Channel and rib width	
h_c	Compressed GDL thickness under rib	
h_0	Uncompressed GDL thickness	380 µm
	CL thickness	25 µm
	Membrane thickness	50 µm
	TH1, TH2 thickness	10 µm
Material parameters		
$D_{O_2,H_2O}(p_0,T_0)$	diffusion coefficient O_2,H_2O	3.98×10^{-5} m^2 s^{-1} [128]
$D_{O_2,N_2}(p_0,T_0)$	Binary diffusion coefficient O_2,N_2	2.95×10^{-5} m^2 s^{-1} [128]
$D_{H_2O,N_2}(p_0,T_0)$	Binary diffusion coefficient H_2O,N_2	4.16×10^{-5} m^2 s^{-1} [128]
σ_s^{CL}	CL electric conductivity	320 S m^{-1}
σ_m^{CL}	CL ionic conductivity	5.09 S m^{-1}
κ_{CL}	CL thermal conductivity	0.476 W m^{-1} K^{-1} [115]
κ_{GDL}	GDL thermal conductivity	1.18 [subchapter 3.2.6]
σ_{GR}	Graphite plate electric conductivity	69700 S m^{-1} [173]
κ_{GR}	Graphite plate thermal conductivity	128 W m^{-1} K^{-1} [173]
σ_m	Membrane ionic conductivity	5.09 S m^{-1} [29]
κ_m	Membrane thermal conductivity	0.12 W m^{-1} K^{-1} [115]
κ_h	Heat transfer coefficient from GDL to air	5 W m^{-2} K^{-1}
k_{CL}	Permeability of CL	1.26×10^{-13} m^2 [166]
ε_0	Porosity of uncompressed GDL	0.83 [174]
ε_{CL}	Porosity of CL	0.4 [172]
Kinetic and electrochemical and other parameters		
ΔE_{exc}	Activation energy ($E_{cell} \geq 0.8$V)	76.5 kJ mol^{-1} [175]
	($E_{cell} < 0.8$V)	27.7 kJ mol^{-1} [175]
p_0	Ambient pressure	101 325 Pa
$\alpha_a^a + \alpha_c^a$	Anodic and cathodic transfer coefficients in Eq. (33)	1 [131]
α_c^c	Cathodic transfer coefficient in Eq. (34)	1 [131]
ΔS_a	Entropy change of anode	0.104 J mol^{-1} K^{-1}
ΔS_c	Entropy change of cathode	-326.36 J mol^{-1} K^{-1}
$a_v j_a^{ref}$	Exchange current density × ratio of reaction surface to CL volume, anode	1.7×10^9 A m^{-3} [128]
$a_v j_c^{ref,T_0}$	Exchange current density × ratio of reaction surface to CL volume, cathode	2×10^4 A m^{-3} [128]
C_{p,O_2}	Heat capacity of oxygen	923 J kg^{-1} K^{-1}
C_{p,H_2O}	Heat capacity of water vapor	1996 J kg^{-1} K^{-1}
E_0	Open circuit voltage	1.23 V
T_0	Reference temperature	273 K

3.3.3. Polarization behavior and species distribution

In the following discussion of modeling results, the compressed GDL thickness under the rib is 250 µm for the both cases, i.e. base case and case considering inhomogeneous compression, unless stated otherwise. The polarization curves for the two modeled cases, presented in Fig. 34, were obtained by changing the cell voltage from 1 to 0.45 V. The voltage drop at low current density region is steep possibly because the adopted values of exchange current density are smaller than those of state of the art experimental results. The curves are almost identical for both the cases except at lower voltages. Since two-phase flow is not taken into account here, the model is valid only when partial pressure of water, p_{H_2O}, does not exceed the saturation pressure, p_{sat}. The lowest limit for voltage was determined by calculating the relative humidity under the rib where flooding usually starts, see e.g. [12,13,35]. Fig. 35 shows the relative humidity of gas (p_{H_2O} / p_{sat}) at the GDL/CL interface at cell voltages of 0.45 and 0.5 V. In both modeled cases, water starts to condense when the cell voltage is below 0.5 V and thus in the following the cell voltage is fixed 0.5 V.

Fig. 36 shows the molar fraction of oxygen at the GDL/CL interface for both the modeled cases. Only slight difference in molar fraction of oxygen is observed between the two cases as discussed in previous work, which suggests that the mass transfer is not significantly affected by GDL deformation as long as no flooding occurs.

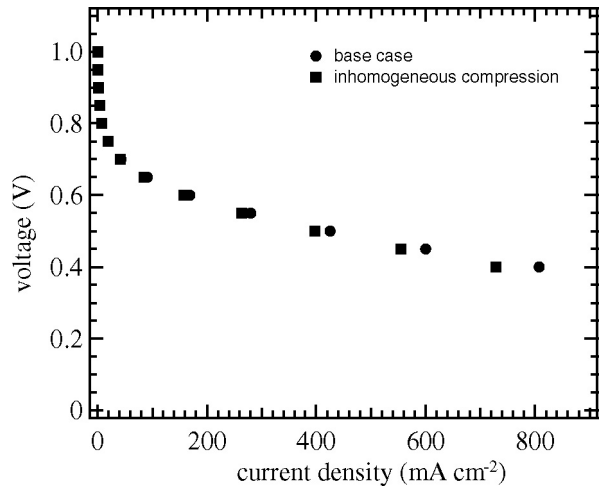

Fig. 34 Polarization curves for the base case and case considering the inhomogeneous compression.

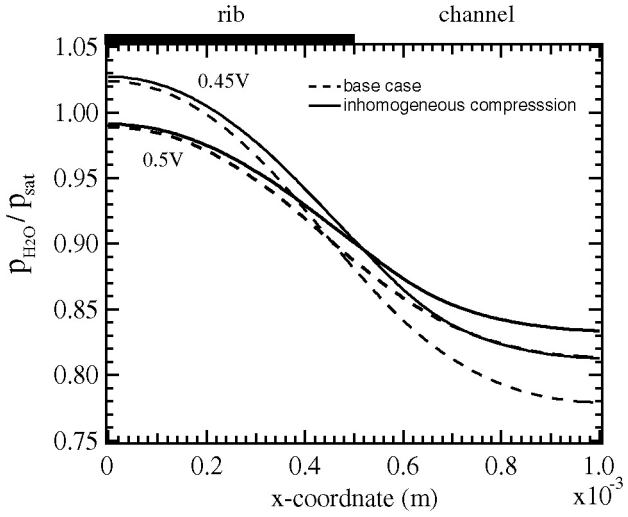

Fig. 35 Relative humidity (p_{H2O}/p_{sat}) at the GDL/CL interface at the cell voltage of 0.45 (thin line) and 0.5 V (bold line) for the base case and case considering the inhomogeneous compression.

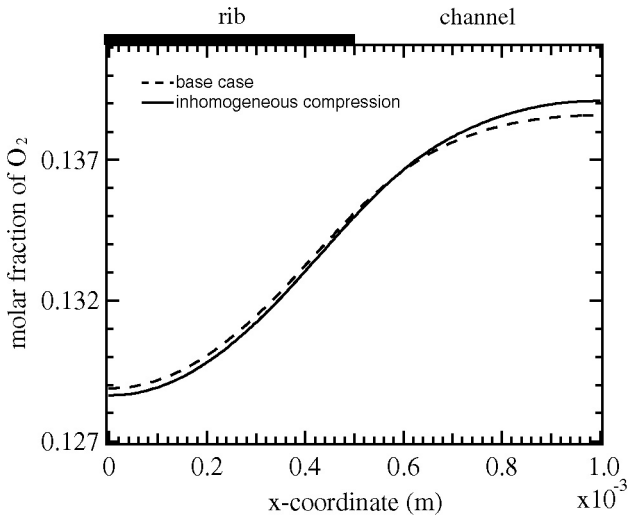

Fig. 36 Oxygen molar fraction at the GDL/CL interface at cell voltage of 0.5 V.

3.3.4. Current density distribution

Fig. 37 shows the current density distribution at the GDL/CL interface. For the base case, the current density distribution is fairly uniform over the active area. However, a notably uneven distribution is seen when inhomogeneous compression is taken into account. In this case the local current density is significantly lower in the middle of the channel and increases in the region close to the edge of the rib. This is because of changes in the selective current path, which is largely determined by the electric contact resistance between the GDL and CL, i.e. $\sigma_{TH2,y}(x)$ in Eq. (50), and electric conductivities of GDL in Eqs. (47 and 48). A large portion of the produced current flows laterally under the channel where the contact resistance is high and crosses over to the GDL near the rib edge (see Fig. 38).

The shape of the current density distribution is different from that observed in the previous study [128]. The difference mainly arises from the estimates used for the contact resistance between the GDL and CL, and the shape of the deformed GDL, which both differed significantly from the experimentally evaluated values used here. As a result, the current density was overestimated at the edge of the rib and under the channel in the previous study.

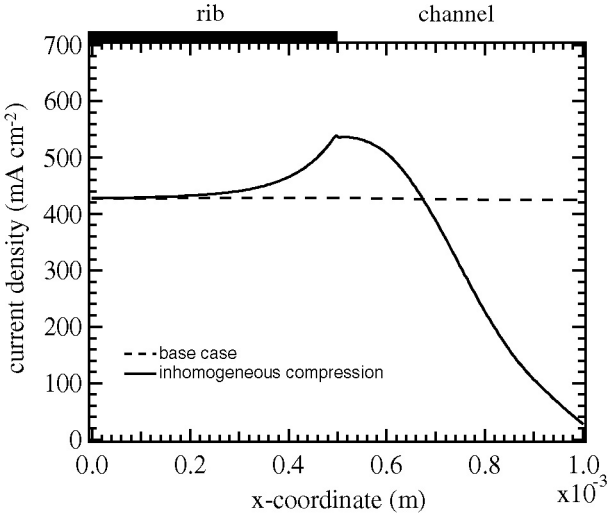

Fig. 37 Current density distribution at the GDL/CL interface at cell voltage of 0.5 V.

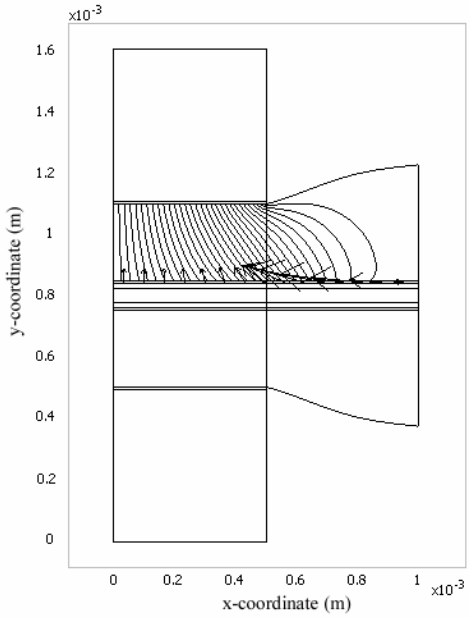

Fig. 38 Current density profile at TH2/CL interface (arrow plot) and at cathode GDL (streamline plot). Note that the magnitudes of arrow and streamline plots are not in scale.

3.3.5. Temperature profile

Fig. 39 shows the temperature profile at the GDL/CL interface. It is interesting to note that when inhomogeneous compression is taken into account the temperature profile is more uniform than that of the base case. A possible reason for this is that the current density under the channel is substantially smaller when inhomogeneous compression is taken into account than in the base case (see Fig. 37). All the terms of the heat source equation include current density, and thus the current density distribution directly affects the temperature profile. Among the heat sources, the irreversible heat of electrochemical reactions accounts for a major part of heat production.

The temperature difference across the active area for the case considering inhomogeneous compression, less than 1 ˚C, is much smaller than the value, more than 10 ˚C, predicted in a previous study [176]. There, the values for the thermal contact and thermal bulk resistances were overestimated and the values of electric contact resistance between GDL and CL were underestimated, leading into larger temperature differences across the components.

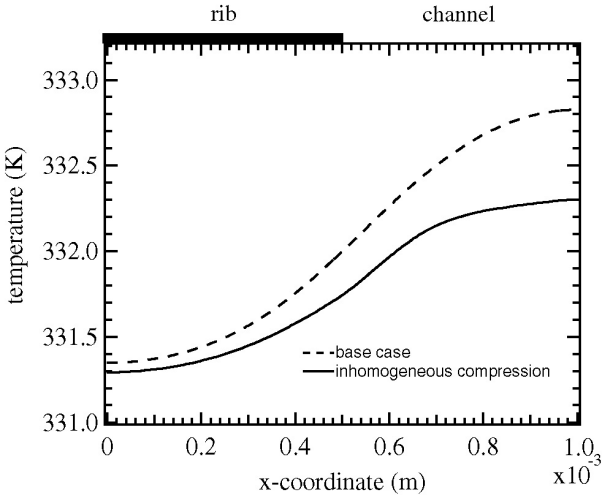

Fig. 39 Temperature distribution at the GDL/CL interface with cell voltage of 0.5 V.

3.3.6. Effect of the compressed GDL thickness

Applying the simulation technique described above, the effects of compressed GDL thickness on charge and heat transport were investigated. The thickness of the compressed GDL under the rib was varied from 300 to 150 μm, and a corresponding expression for the shape of the GDL intruding into the channel was used. The physical properties of the GDL were changed correspondingly.

Fig. 40(a) shows the current density distribution at the GDL/CL interface for various compressed GDL thicknesses under the rib. The total current integrated over the active area increases as the GDL is compressed more, since both the electric contact and bulk resistances of GDL are reduced. For example, the case in which the GDL is compressed to 150 μm produces ca. 25% more current than the case of 300 μm at the same cell voltage of 0.5 V. The shape of the current density distribution also changes when the compressed GDL thickness is changed. A current density peak is observed at the edge of the rib when the GDL is compressed to 300 μm. On the other hand, when the GDL under the rib is compressed to 150 μm the current density has a maximum at around x = 0.61 mm. In this case, the contact resistance between GDL and CL is small enough even under the channel so that lateral current flows in the CL change the direction and enter into the GDL. The shape of current density distribution is largely determined by the profile of the deformed GDL, on which the contact resistance between the GDL and CL depends.

Fig. 40(b) shows the temperature profile at the GDL/CL interface for various compressed GDL thicknesses under the rib. As predicted in the previous study [see publication IV], the temperature under the rib increases with decreasing compression because of an increase in both thermal bulk and contact resistance. However, the temperature profile becomes more uniform over the active area when the GDL under the rib is less compressed. This is due to the lower heat production under the channel in such a case. Since the value of oxygen molar fraction depends on the porosity of GDL, i.e. the shape of GDL, lower compression of GDL leads into relatively higher value of oxygen molar fraction compared to the case of higher compression, which in turn results in a lower value of overpotential in CL. Even though the differences in their values are fairly small (ca. less than 2% for both oxygen molar fraction and overpotential), changes in heat production are notable. For example, the irreversible heat of electrochemical reactions when the compressed GDL thickness is 200 μm is ca. 23% higher than that for the case of 300 μm on an average over the active area.

The minor irregularities in the shape of the current density distribution under the channel (Fig. 40(a)) stems from the difficulty of determining the profile of the GDL intrusion into the channel $h(x)$, i.e. the equivalent of Eq. (27) for each compressed GDL thickness under the rib. Due to the structurally complex architecture of GDL, the profile of the deformed GDL under the channel varied from sample to sample in the photomicrographs taken at the same compressed thickness under the rib. Therefore, the expressions for $h(x)$ are unique for each sample and compressed thickness, which is in turn reflected in the current density profiles.

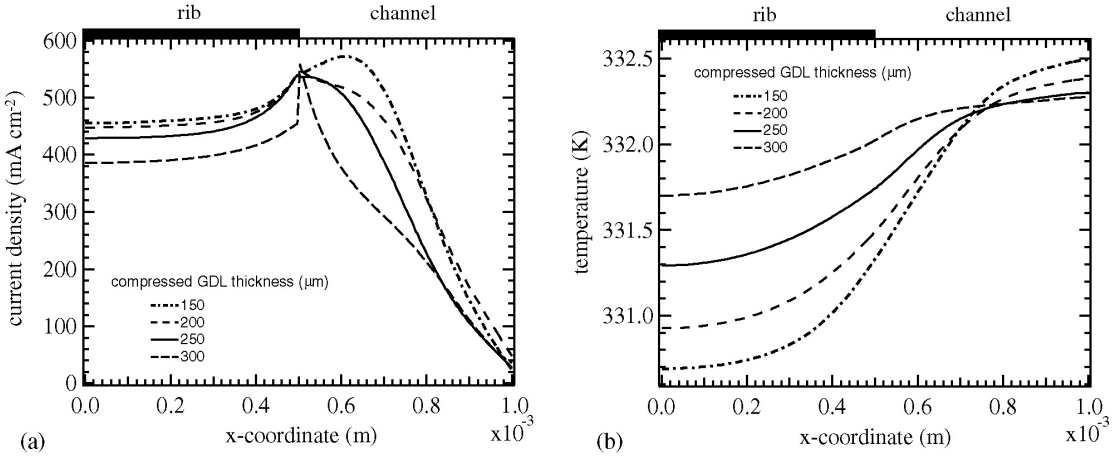

Fig. 40(a) Current density distribution and (b) temperature profile at the GDL/CL interface at cell voltage of 0.5 V with various compressed GDL thickness under the rib.

3.4. Unpublished results

Compressive behavior of wet GDL (for sub-chapter *3.2.1.*): In the measurement, the GDL sample was immersed into cold and hot water for 24 hours and 1 hour, respectively, and the procedure described in the sub-chapter 3.2.1. was carried out. The reason for using hot water also here was that the surface tension depends on temperature and generally decreases with increasing temperature due to the larger amount of stored energy within the molecules, leading to an increase in wettability characteristics of pore network [26]. The obtained stress-strain curves for wet GDL samples were found almost identical to those for dry sample.

Process of reducing the contact resistance between facing GDLs (for sub-chapter *3.2.3.*): In order to eliminate the contact resistance between facing GDLs for the evaluation of electric GDL conductivities, at first author considered pasting highly conductive silver glue onto the surface of GDL. However, this method was not adopted since the silver glue was too viscous in order to spread out on the GDL evenly and thinly, and once strong force was applied to spread it out some portion penetrated into the pore of GDL, resulting in a change of GDL bulk conductivity.

Effect of silver sputtering (for sub-chapter *3.2.3.,3.2.5.,3.3*): The effect of silver sputtering treatment on the reduction of contact resistance was studied by the comparison of the measured results obtained from the system (see Fig. 19(a)) with silver sputtered and non-sputtered GDLs. Fig. 41 shows the measured resistance as a function of the number of stacked GDLs for various compressed GDL thicknesses ranging from 150 to 300 μm. Figures clearly show the silver sputtering treatment reduces the total resistances ranging from 14 to 17% when each GDL was compressed to less than 250 μm. With very low compression pressure, which compressed each GDL to 300 μm, the magnitude of reduction in the measured resistance is found relatively large, more than 25%.

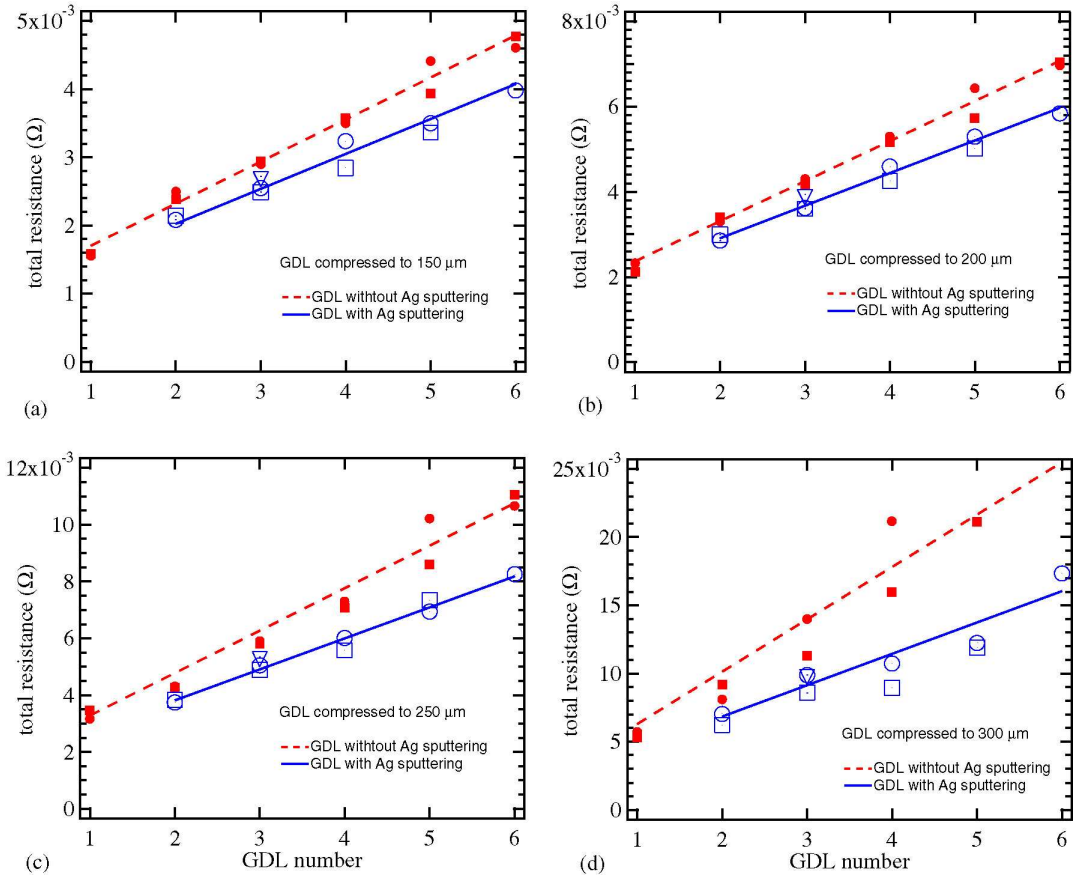

Fig. 41 Measured total resistances of stacked GDLs with and without Ag sputtering for the GDLs compressed to (a) 150, (b) 200, (c) 250 and (d) 300 μm.

To study the effects of silver sputtering on the contact resistance between two facing GDLs, the following three standard assumptions were made including that described in sub-chapter 3.2.3, and through-plane GDL conductivities and contact resistance between GDL and graphite were calculated and compared.

The assumptions made here are namely:

· *Assumption A*: the contact resistances between two facing GDLs are reduced to zero by the silver sputtering treatment (presented in sub-chapter 3.2.3.)

· *Assumption B*: the contact resistances between two facing GDLs are intentionally neglected although the GDL surfaces are not silver sputtered

· *Assumption C*: the contact resistances between two facing GDLs are reduced by 50% by the silver sputtering treatment

Assumption B:

The through-plane GDL conductivities for the measurement system where the sputtering treatment is not given are derived using Eq. (11a). The Eq. (11a) is now in an unwrapped form rewritten as follows:

$$\begin{aligned} R_{z,meas}^{non-Ag}(z,n) &= 2R_{GR} + n \cdot R_{b,GDL}(z) + 2R_{c,GR/GDL}(z) + (n-1) \cdot R_{c,GDL/GDL}(z) \\ &= n \cdot \left(R_{b,GDL}(z) + R_{c,GDL/GDL}(z)\right) + 2R_{GR} + 2R_{c,GR/GDL}(z) - R_{c,GDL/GDL}(z) \end{aligned} \tag{11c}$$

If the contact resistances between two facing GDLs, $R_{c,GDL/GDL}(z)$, are reduced to zero by the silver sputtering treatment on the GDL surfaces (*Assumption A*), the slope of the plot of $R_{z,meas}(z,n)$ as a function of number of GDLs, n, in Fig. 41 indicates the bulk GDL resistance, $R_{b,GDL}(z)$, as described in sub-chapter 3.2.3. However, without the silver sputtering treatment, the slope becomes larger because of the existence of $R_{c,GDL/GDL}(z)$, which is clearly seen as a deviation in slope between the red broken lines and the blue line in Fig. 41. Here if one assumes the pseudo bulk GDL resistance, $R_b^{non-Ag}(z)$, which is a sum of $R_{b,GDL}(z)$ and $R_{c,GDL/GDL}(z)$, the pseudo though-plane GDL conductivity obtained from the system without silver sputtering treatment, $\sigma_{GDL}^{non-Ag}(z)$, can be calculated from it. Note that the $\sigma_{GDL}^{non-Ag}(z)$ for GDL compressed to 350 μm is not included in Fig. 42 since the accurate measurement of total resistance for the system without silver sputtering treatment was extremely difficult especially when the GDL was very little compressed (30 μm) and thus the measured results are unreliable. However, the trend that lower compression pressure yields lower through-plane GDL conductivity was verified.

Assumption C:

If the $R_{c,GDL/GDL}(z)$ are reduced to half from original values by the silver sputtering treatment, the Eq. (11a) can be rewritten as:

$$\begin{aligned} R_{z,meas}^{half}(z,n) &= 2R_{GR} + n \cdot R_{b,GDL}^{half}(z) + 2R_{c,GR/GDL}(z) + 0.5(n-1) \cdot R_{c,GDL/GDL}(z) \\ &= n \cdot \left(R_{b,GDL}^{half}(z) + 0.5R_{c,GDL/GDL}(z)\right) + 2R_{GR} + 2R_{c,GR/GDL}(z) - 0.5R_{c,GDL/GDL}(z) \end{aligned} \tag{11d}$$

By the subtraction of Eq. (11d) from the equation representing the electrical resistances of the system without silver sputtering treatment, i.e. Eq. (11c), the $R_{c,GDL/GDL}(z)$ can be expressed as:

$$R_{c,GDL/GDL} = \frac{R_{z,meas}^{non-Ag}(z,n) - R_{z,meas}^{half}(z,n)}{0.5(n-1)} \tag{11e}$$

where n is a number of stacked GDL and larger than 2.

The calculated $R_{c,GDL/GDL}(z)$ for each compressed GDL thickness are then substituted to Eq. (11d), and with the slopes of blue line in Fig. 41 the bulk GDL resistance for *Assumption C*, $R_{b,GDL}^{half}(z)$, can be determined. Finally, the through-plane GDL conductivities, $\sigma_{GDL}^{half}(z)$, can be obtained from the $R_{b,GDL}^{half}(z)$. For the same reason mentioned above, the $\sigma_{GDL}^{half}(z)$ for the GDL compressed to 350 μm is not included in Fig. 42.

The comparison of the $\sigma_{GDL}^{Ag}(z)$ shown in Fig. 21 with $\sigma_{GDL}^{non-Ag}(z)$ and $\sigma_{GDL}^{half}(z)$ provides the insight of the effect of silver sputtering on the reduction of $R_{c,GDL/GDL}(z)$. Fig. 42 illustrates the calculated conductivities $\sigma_{GDL}^{Ag}(z)$, $\sigma_{GDL}^{non-Ag}(z)$ and $\sigma_{GDL}^{half}(z)$ for *Assumption A*, *B* and *C*, respectively. The error estimates of the conductivities are obtained from the error sources including the deviations of slopes in Fig. 41, measured total resistances of the systems and the compressed GDL thickness.

As expected, the stacked GDLs without the silver sputtering treatment yield lower conductivities since the $R_b^{non-Ag}(z)$ inherently includes the $R_{c,GDL/GDL}(z)$, and the subtraction of the contribution of $R_{c,GDL/GDL}(z)$ with the *Assumption C* yields higher conductivities. Whatever the assumptions, the through-plane GDL conductivities are expected to be in between two extreme cases: *Assumption B* and *C*.

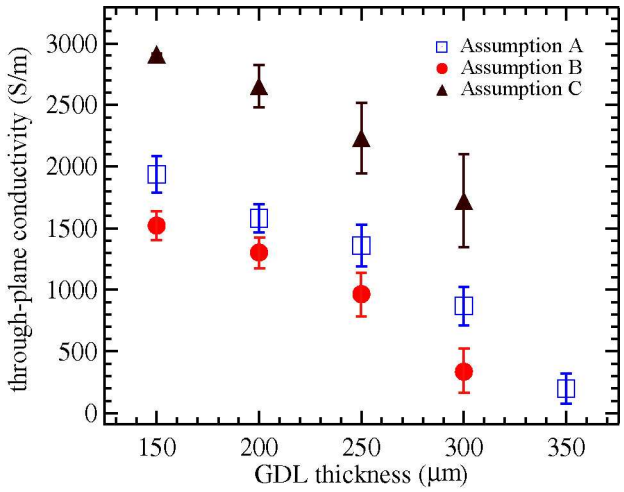

Fig. 42 Through-plane conductivities of GDL calculated with three assumptions.

The contact resistances between GDL and graphite are then calculated using the model described in sub-chapter 3.2.5 with the evaluated through-plane GDL conductivities. The errors are estimated from the major error sources, the value of through-plane conductivities and measured voltage drop.

Since the bulk GDL resistances are larger with *Assumption B*, and smaller with *Assumption C* than those with *Assumption A*, the calculated contact resistances are smaller and lager, respectively, than those seen in Fig. 22.

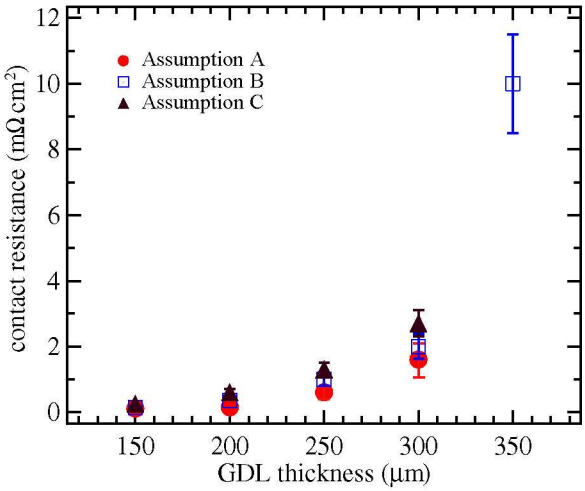

Fig. 43 Contact resistance between GDL and graphite calculated using the evaluated through-plane conductivities based on three assumptions.

The magnitude of bulk GDL resistance is negligibly small compared to the membrane and cell resistance as seen in Fig. 26. Therefore, the effect of error in the through-plane GDL conductivity was thought trivial and simply neglected for the derivation of contact resistance between GDL and CL.

The effects of silver sputtering are further studies using the model presented in sub-chapter 3.3. As applied in sub-chapter 3.3.2.3, the contact resistances between GDL and graphite are converted to the through-plane conductivities of pseudo thin layer, TH1 (see Fig. 33), and the $\sigma_{GDL}^{non-Ag}(z)$ and $\sigma_{GDL}^{half}(z)$ which are linearly fitted as a function of compressed GDL thickness are embedded in the model. Fig. 44(a) and (b) show the modeled current density distribution and temperature profile at the interface between GDL and CL, respectively, with the parameters obtained based on the three assumptions. It is obvious from Fig. 44(a) and (b) that the slight difference in the values of through-plane GDL conductivities and contact resistance between GDL and graphite causes only minor effect to the modeled results and negligible. In fact, there are much more essential contributors such as contact resistance between GDL and CL, thermal contact resistances, and water transport properties that determine the modeled outcome and consequent cell performance than the electrical through-plane GDL conductivity. Thus, the author suggests future studies devoting to investigate those parameters more thoroughly.

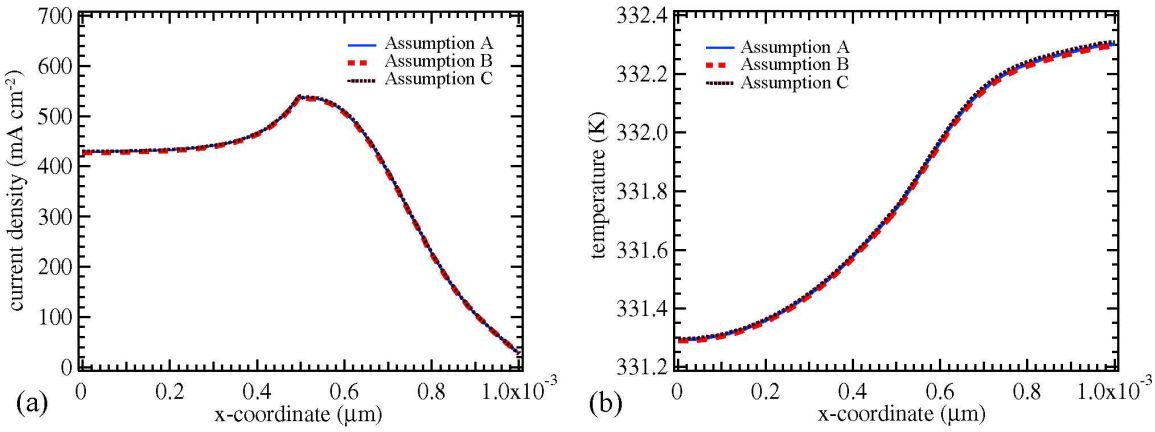

Fig. 44 (a) Current density distribution, (b) temperature profile at the GDL/CL interface at cell voltage of 0.5 V for the GDL compressed to 250 μm under the rib.

Comparison of in-plane conductivity of different GDLs: (for sub-chapter *3.2.3.*): The electric in-plane conductivities of GDL with MPL (SGL SIGRACET® 10 BC) were measured as a function of compressed thickness for the comparison with those of GDL without MPL (SGL SIGRACET® 10 BA). Fig. 45 shows the measured in-plane conductivity of the GDLs.

The in-plane conductivities of GDL 10BC were found slightly higher than those of GDL 10BA. This is most probably because the uncompressed thickness of GDL 10BC is thicker (415 μm) than that of GDL 10BA (380 μm) due to the coating of MPL on one surface, and thus the compressed ratio for GDL 10BC at the certain compressed thickness becomes larger than that for the GDL 10BA. However, since the bulk part of the both GDLs is hydrophobized with same amount of PTFE (5 wt%), the electric properties of both GDLs are expected almost identical.

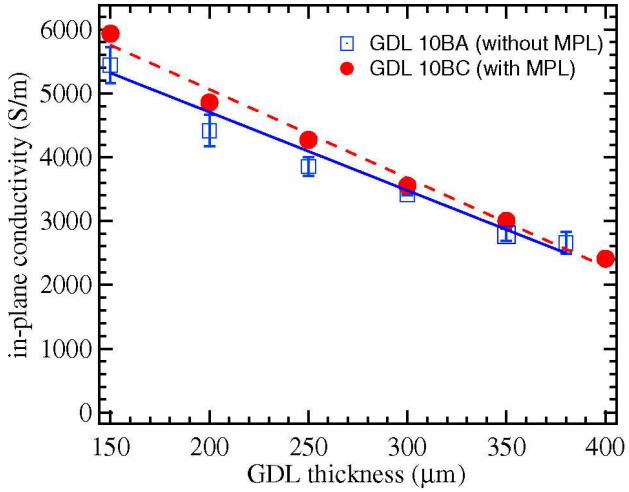

Fig. 45 In-plane conductivities of different GDLs.

Evaluation of contact resistance between GDL and CL: (for sub-chapter *3.2.6.*): The evaluation of contact resistance between GDL and CL on the electrolyte membrane, $R_{c,GDL/CL}$, was attempted using the experimental setup shown in Fig. 19(b). The measurement was conducted fundamentally similar approach for the evaluation of electric contact resistance between GDL and graphite. The difference was that the GDL was replaced with MEA and there were GDLs between the graphite current collectors and MEA. The potential profile was modeled with a similar domain as in in-plane experimental setup (see Fig. 19(b)) by applying previously evaluated parameters. The $R_{c,GDL/CL}$ obtained here by simulation was in the range of 1-7 Ω cm^2 for GDL thicknesses from 150 to 350 μm, which are far too high and unreliable. If the contact resistance really was that high, the voltage of a unit cell would drop to zero due to resistive losses only at the current density of approximately 500 mA/cm^2. A possible explanation for these unrealistic results is that the current profile through the electrode and GDL interface was significantly uneven. Practically all of the current concentrated to the very edge of GDL since the graphite and GDL conductivities were significantly higher than the measured conductivity of the electrode (320 ± 20 S/m). This may have caused numerical problems in the simulations and distorted the results.

In order to adjust the compression pressure to the active area and separate the anode and cathode compartments in H_2/H_2 cell (see Fig. 24), a plastic wrap was used. A circular MEA with a diameter of 10 mm was mounted on the hole of the plastic wrap with diameter of 8.5 mm in a concentric fashion and pasted with double-faced tape. Then circular GDLs with diameter of 8.5 mm were also mounted to the MEA.

Effect of silver sputtering (for sub-chapter *3.2.7.*): Fig. 46 shows the measured total temperature drop of the system (see Fig. 28) as a function of each compressed GDL thickness. The figure includes the results for two and four stacked GDLs with and without silver sputtering treatment on the GDL surfaces. The silver sputtering treatment slightly reduced the measured temperature drop, although the difference is found only less than 4%, which is by far smaller than that of electric total resistances (see Fig. 41).

Since the differences in the measured temperature drop of the system between with and without silver sputtered samples are so small, the calculated thermal contact resistances between two facing GDLs are quite small even though the calculation was conducted based on the assumption that only 10% of the contact resistance between GDLs were reduced by the sputtering treatment. In general the evaluation of thermal properties is far more difficult than that of electric counterpart because of, for example, the difficulty of proper heat insulation and the determination of transferred heat flux, and thus obtaining a reliable parameter is difficult. Thus the evaluated values of thermal GDL conductivity in this work may contain a large error and further study is necessary.

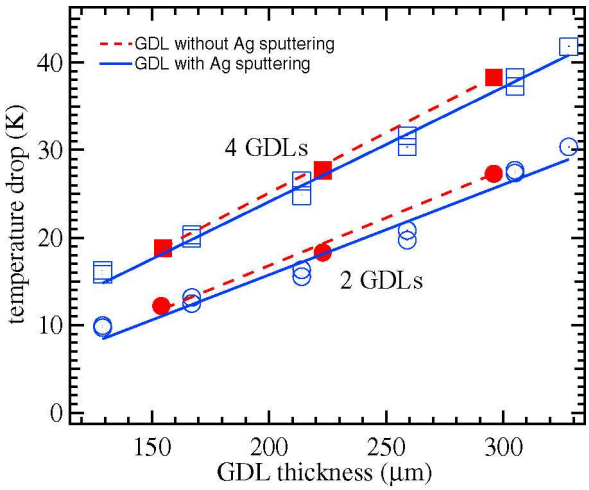

Fig. 46 The measured total temperature drop of stacked GDLs with and without Ag sputtering.

Comparison of modeled results (for sub-chapter *3.3.*): A number of notable differences are found in modeled results presented in publication II and V. They are mainly arisen from physical assumptions in publication II:

1. Porosity expression

2. Water saturation expression

3. Geometry of deformed GDL under the channel

4. Contact resistance between GDL and CL

The equation (42) for porosity expression in publication II yields significantly lower porosity values. For example, when the GDL is compressed to 250 μm the calculated porosity with Eq. (42) is 0.49, which is in fact 0.74 with right equation (18) in publication V. The low values in porosity in turn result in significantly low oxygen molar fraction as shown in Fig. 47 (black broken line). The reason why the calculated molar fraction in publication II is lower than that seen in Fig. 47 is that the water filling of pores (expressed with an equation (10)) was also taken into account in the publication II. As a consequence of the significant depression in oxygen molar fraction under the rib, the current density profile is quite uneven even for the base case in publication II.

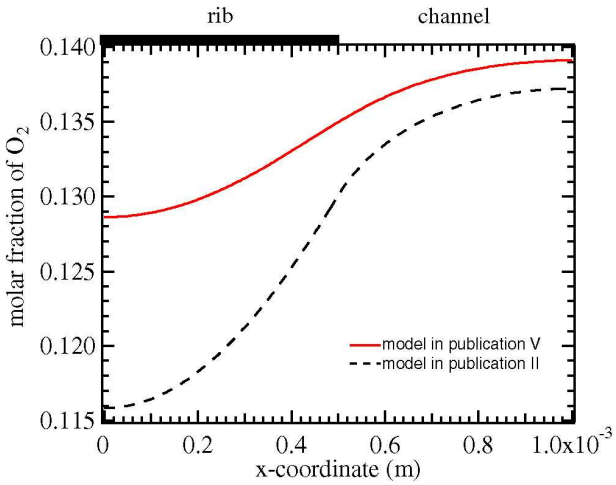

Fig. 47 Molar fraction of oxygen at the GDL/CL interface at the cell voltage of 0.5V where inhomogeneous compression is taken into account in the models.

The magnitude of peak in current density at the edge of rib for the models where inhomogeneous compression is taken into account is highly dependent on the interrelation of the equation representing the contact resistance between GDL and CL (i.e. equivalent conductivity of TH2 in publication V) and the geometry of intruded GDL into the channel. Fig. 48 shows an example. The curves in Fig. 48 illustrate the current density profile of:

· *Black broken line*: roughly estimated GDL deformation under the channel expressed with logarithmic curve (adopted in publication II) with roughly assumed contact resistance between GDL and CL (adopted in publication II)
· *Black dotted line*: roughly estimated GDL deformation expressed under the channel with logarithmic curve (adopted in publication II) with measured contact resistance between GDL and CL (adopted in publication V)
· *Red line*: experimentally observed geometry of GDL deformation under the channel (adopted in publication V) with measured contact resistance between GDL and CL (adopted in publication V)

A current density profile has a high peak at the edge of rib as discussed in publication II when the wrong assumptions were made for contact resistance and GDL geometry. Furthermore, the current density under the channel is somewhat overestimated, which in turn yields unrealistically high temperature region as shown in ref. [176].

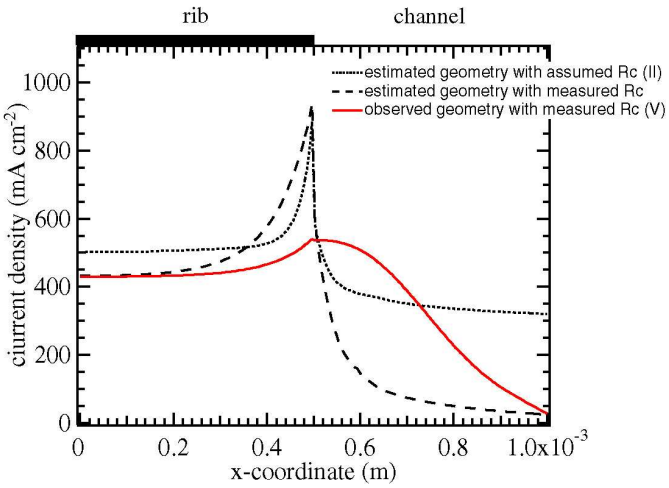

Fig. 48 Current density distribution at GDL/CL interface at cell voltage of 0.5 V with different GDL geometries and assumptions of contact resistance between GDL and CL for the GDL compressed to 250 μm under the rib.

Another example is shown in Fig. 49(a) and (b), representing the two different fitted curves of equivalent conductivity of TH2 and the modeled current density profile with the fitted conductivities. The Fig. 49(b) clearly shows that the slight difference in the fitting equation of equivalent TH2 conductivity (i.e. the expression of contact resistances between GDL and CL) significantly affects the current density distribution.

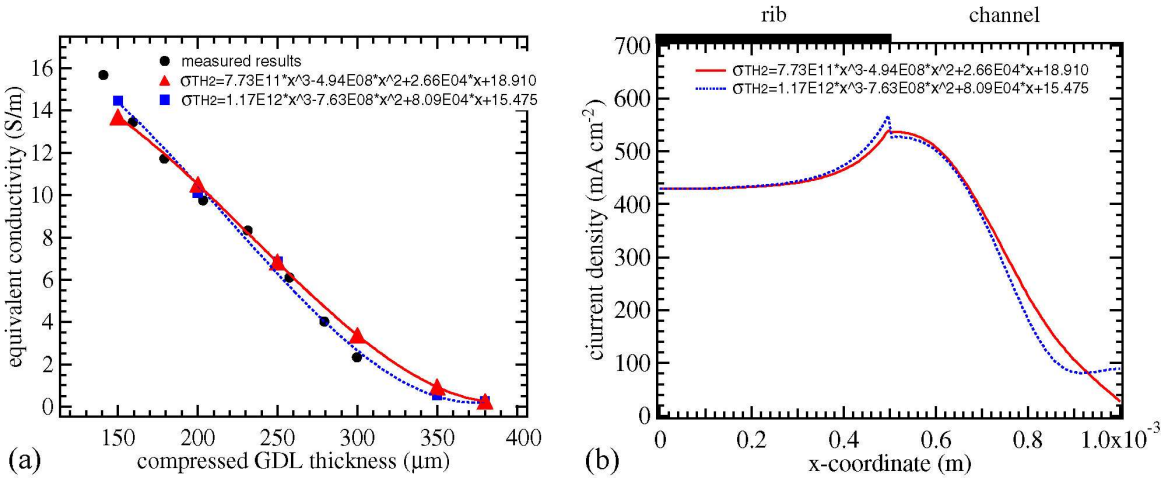

Fig. 49 (a) Fitting curves of equivalent conductivity of TH2, and (b) current density distribution at GDL/CL interface at the cell voltage of 0.5V with different expression for equivalent conductivity of TH2.

Observation of GDL deformation (for sub-chapter *3.3.2.*): In order to make qualitative analysis of GDL deformation under the channel, the channel width was changed from 0.5 to 2 mm for various compressed GDL thicknesses (see Fig. 12(a)). Because of the structurally complex internal architecture of GDL, it was somewhat difficult to obtain the identical deformation curves for each compressed GDL thickness, however the channel width was ascertained not to affect the deformation curves significantly.

3.5. Suggestion for future studies

There is a continued interest in understanding the transport phenomena inside GDLs. It is often claimed that the liquid water transport mechanism is the slowest and most dominant in influencing the performance of the cathode [10,13]. This is due to the fact that when the cell is flooded by the condensed water, gas transport is significantly hindered, which in turn affects the electrode kinetics and heat production since all of the type of transport (gas, liquid, electric and heat) are highly interrelated.

The physical properties of GDLs are the key to determining the water transport through GDL, CL and even membrane and amount of liquid water accumulated in GDL, MPL, CL and flow field channel [27,65,194]. However, at present, fundamental information on water transport parameters in GDL is scarce because of the complicated bimodal pore distribution and nonuniform wettability characteristics, and many of the necessary relationships and parameters embedded in typical two-phase models are questionable. To the author's knowledge, GDL-specific experimental data on water transport properties have been published only recently, see, e.g. [68,69] or estimated from numerical models, see, e.g. [20,138]. Therefore, further effort is necessary to elucidate the reliable correlations for two-phase transport properties directly relevant to GDL, such as effective gas permeability, effective porosity and effective diffusivity as well as their dependence on liquid water saturation or local liquid water content, the functional dependence of capillary pressure on saturation and condensation and evaporation rate of water.

Of particular importance is fact that the water transport within the GDL is strongly coupled with the compression [25], since any change in the pore structure can cause a substantial change in the multiphase transport characteristics. Bazylak et al. visualized the water transport through the GDL using fluorescent microscope and the preferential pathway for liquid water transport was found in the compressed part of the GDL [118]. Zhang et al. also observed the liquid accumulation under the rib [41]. This was most probably because these broken fibers act as hydrophilic defects and thus decrease water removal [97], expansion of the hydrophilic sites due to the breakage of hydrophobic agent coating by compression [25,27] or degrading the hydrophobicity during the operation [191,192]. In a common fuel cell, which uses carbon-paper type GDL and rib/channel grooved bipolar plate, partial deformation of GDL is unavoidable, and thus spots where water is prone to condense must be created especially at compressed GDL sites under the rib. Previous modeling studies have also argued that flooding starts under the rib, but their logic stems from the longer diffusion length, i.e. difficulty of water vapor to escape, and relatively lower temperature because of better heat conduction under the rib, see, e.g. [11-13,35,191], but not from the changes in GDL physical properties as a result of the compression.

In the following, suggestions for future studies on water transport properties are listed. In addition, subjects on which further discussions are needed in terms of the validity of our assumptions or uncertainty in the results are also stated.

Total pore size distribution and capillary pressure under compression

A detailed investigation of the change in the total (both hydrophobic and hydrophilic) pore size, its distribution and the pore structure of GDL as a function of compression is critical to establishing the accurate multiphase transport characteristics of the GDL, since they are directly relevant to both gas and liquid water permeability. According to Wilde et al. [122], the collapsing of the microstructure of GDL by compression pressure forms locally larger pores. Although their discussion contained uncertainty since they did not provide any information on the properties of their working fluid (most probably wetting fluid), a probable

reason for their finding that large local pores were generated by the compression due to the hydrophilic defects forming a virtual pore network. In typical models, it has been assumed that the reduction of the thickness of GDL under the compression leads to a loss of porosity by uniform reduction of pore size. However, the relation between compression and pore size distribution may not be that simple and thorough experimental assessment is necessary.

The measurement can be performed by applying the method of standard porosimetry (MSP). MSP is a reliable and established technique used for acquiring the necessary data regarding the capillary pressure-saturation behavior of porous materials. Since the MSP technique is based on the natural capillary equilibrium concept, measurements with this technique does not require any external pressure to let the working fluid intrude into the GDL like in mercury intrusion porosimetry (MIP). In the experiments, the GDL is brought into contact (maybe soaked) with a low surface tension liquid as intrusion fluid, e.g. octane or silicone oil, which wicks into the sample. By applying a gas pressure across the flooded sample, the liquid can be forced out of the pores. The pressure at which gas begins to flow due to the clearing of the first pore (reflecting onset of flow occurring) is called the bubble point, and this point can be used to calculate the maximum pore size D with the Washburn equation, see, e.g. [177-179]:

$$D = \frac{4\gamma_{l/g}\cos\theta}{p_c} \tag{52}$$

where $\gamma_{l/g}$ is the surface tension of the liquid, θ the contact angle and p_c the capillary pressure.

The pressure is then further increased and a ***wet curve*** is traced as the sample is being cleared of liquid until the sample is fully dried. A ***dry curve*** where only dry gas is fed is also taken in a subsequent scan. The smallest detectable pore diameter is obtained from the pressure at which the ***wet curve*** meets the ***dry curve***. The pressure at which ***wet*** and ***half-dry curves*** (calculated from dry curve to yield half of the flow rate through the sample at a given differential pressure) intersect gives the mean flow pore diameter. An example of flow rate vs. pressure drop data from a through-plane MSP experiment with carbon fiber paper is shown in Fig. 50 [65].

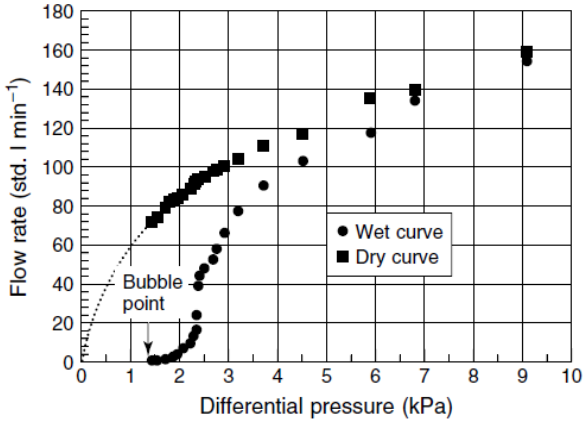

Fig. 50 Flow vs. pressure curves [65]

From the difference between the ***dry***, the ***half-dry*** and the ***wet curves***, one can calculate the pore size distribution. The pore size distribution determined from the data in Fig. 50 is shown in Fig. 51 where the cumulative flow is plotted against pore size. By design of a sample holder that passes flow in the plane of the sample, the in-plane flow-based pore size distribution can be determined. In this case, the compressed GDL thickness can be varied and an interrelation between compressed thickness and pore size distribution may be studied.

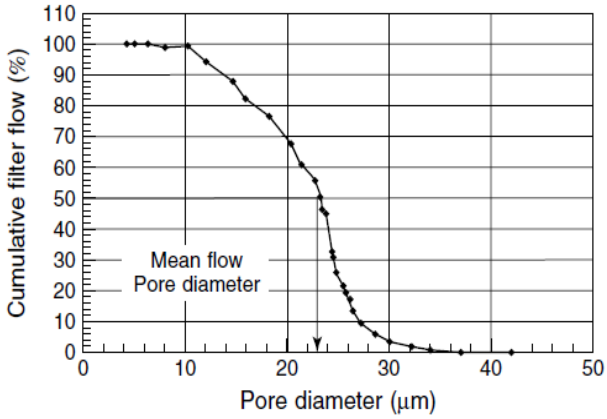

Fig. 51 Cumulative-filter-flow pore size distribution [65]

In reality, it would be very difficult to define distinct pore bodies and to identify pore structure, consisting of hydrophobic, hydrophilic, blind and throat pores [155] (see Fig. 52). Therefore, studying the pore network (or pore connectivity) of GDL is in fact far more important than pore size and the distribution when discussing the reactant and product transport. Obviously, the best way to construct the pore network would be to extract its geometric and topological properties from experimental 3D volume data of the GDL materials. However, this may be extremely challenging because of the complex random microstructures of GDLs. Therefore, in addition to MSP, other methods such as MIP are also worth trying when evaluating the pore structures. As discussed by Gigova and Lee et al. [180,181], different fluids provide information on different pore characteristics, e.g. MIP measures the wider parts of the pore as large pores of considerable volume and the narrowest part as a small pore of small volume, on the other hand MSP detects pores with constricted part and wide mouth as a single pore of small diameter, disregarding their complex shape and cross-section. A combination of different methods may provide detailed information of pore structure.

Furthermore, several models have recently been proposed to express the pore structure, such as Weibul cumulative distribution adopted by Gostick et al. [138] with spatial correlation of pore sizes using experimental data, or stacks of continuously interwoven (overlapping) fiber screens with regular, square pore spaces adopted by Nam et al. [20]. Comparisons of experimental data with mathematically constructed pore structure may yield useful information.

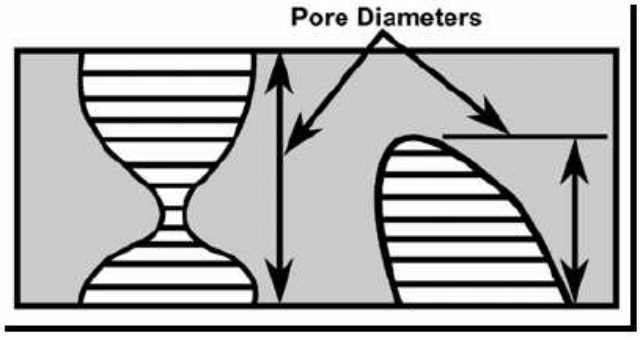

Fig. 52 Possible pore structures of GDL [155]

According to the theoretical description given in Eq. (52), applying compression on the GDL reduces the available pore volume and consequently decreases the pore radius, therefore leading to a higher capillary pressure. On the other hand, excessively high compression may

create hydrophilic sites in GDL and thus, the capillary pressure may decrease. Consequently, water distribution in the GDL should be affected by local compression pressure and experimental evaluation of compression effects on capillary pressure should be carried out.

The measured capillary pressure data can be analyzed in terms of the commonly used p_c–s_{wp}(or s_{nwp}) curves obtained using MIP and MSP as shown in Fig. 53.

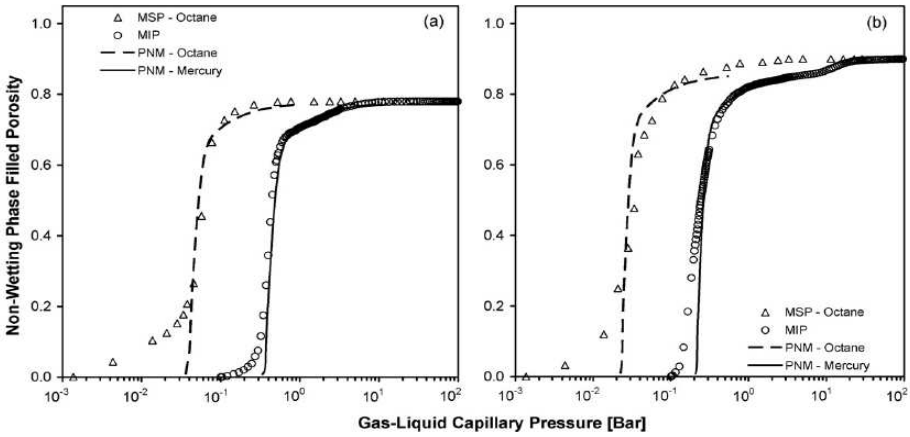

Fig. 53 Example of p_c–s_{wp} curves from MSP and MIP [138]

The experimentally evaluated $p_{c,exp}$ of a certain working fluid can be converted to that of water according to the following equation [69,182,191]:

$$p_{c,water} = \frac{\gamma_{2-air}\cos\theta_{2-air}}{\gamma_{1-air}\cos\theta_{1-air}} p_{c,\exp} \tag{53}$$

Measurement can be conducted with various compressed GDL thicknesses, various amount of hydrophobic agent and different temperature. Quite recently, Kumber et al. conducted this kind of measurements and provided good correlation equations for the capillary pressure [24-27]. There, they used GDLs coated with a MPL. The rigid and compact structure of the MPL and thus, almost exclusively hydrophobic in nature, may restrict the water retention within the GDLs, and therefore the effects of temperature and compression on the capillary pressure for the GDLs with a MPL may be different from the ones for GDLs without a MPL. Therefore, the author is not convinced that the p_c–s_{wp} curves for a plane GDL (without the MPL) can be expressed with correlation equations discovered by Kumber et al. by simply eliminating the MPL region. Comparison of measured data for the GDLs without a MPL with data reported by Kumber et al. may provide interesting insight on the effect of MPL on water transport. Furthermore, they correlated the compression effect on the capillary pressure only in terms of the porosity change but not of changes in the hydrophobicity. This contradicts to their experimental data [25] and other reported discussion [41,118]. In fact the hydrophobicity of GDL is affected by the compression and should be also properly correlated. It would be extremely useful toward developing an accurate two-phase model if further studies can elucidate these complicated interrelations.

Contact angle of liquid water in GDL pores

A question still remains concerning the adopted value of contact angle, θ, in Eq. (52) and whether it reflects realistic values for GDL. This question arises because the hydrophobic agent is localized more in the surface region than the interior, since the hydrophobic agent migrates to the surface region during the drying process [22].

In general, the surface contact angle of liquid water on GDL is measured with e.g. the sessile drop method, the Wilhelmy method [65] or the capillary rise method [22]. In the modeling, the contact angles evaluated with these methods are often assumed to be equal to the internal contact angles in the GDL pores. However, the properties of the surface and pores of GDL must be different, especially when the GDL is compressed and the operation temperature is changed [16], and proper experimental evaluation is be needed. A solution was proposed by Gurau et al. [68]. There, various working fluids were used to evaluate θ. The same kind of measurements could be done under the various compression pressures and in various temperatures.

On the other hand, recently Kumber et al. [24-27] introduced empirical Leverett-type functions (capillary pressure vs. saturation relation) without the any representative value of the internal contact angle as an input parameter. If they can be applied to any type of GDL, the contact angle evaluation measurements are not needed any more.

Hydrophobic and hydrophilic pore volume

Once the total pore distribution of GDL under compression is successfully determined, the next step is to distinguish the hydrophilic and hydrophobic pores from total pores in a compressed GDL. The latter are sometimes called effective pores in literature, and represent the part of the porous network of the GDL free of liquid water.

The consequences of partial flooding could be significant not only in lowering the limiting current, but also in affecting the slope of the polarization curve in the medium current density domain [56]. Furthermore, partial flooding may affect the uniformity of flow distribution and affects the relative permeability of gases and liquid water. Therefore, detailed knowledge of effective porosity is important in the two-phase modeling. According to a study by Benziger [119], only a few percent of void fraction of the GDL is necessary for liquid water transport driven by capillary action, whereas a large portion of pores is occupied by ‘disconnected’ water. Only the rest of small pores is for gas transport and thus, diffusive gas transport is significantly confined by water, although Jena et al. [183] asserted that the largest pores have a close link to the gas permeability.

According to the study by Jena [155], hydrophobic pores are relatively small compared to primary hydrophilic pores although many small hydrophilic pores are also contained in the GDL (see, Fig. 54). When the GDL is compressed and a carbon fiber is damaged, the hydrophilic properties of GDL may change as suggested above, which may be observed as a change in hydrophilic pore volume. The dependence of the effective porosity on the combination of external humidification conditions, physical properties of the GDL, cell current and cell dimensions is probably very difficult to predict. Therefore, in this measurement, the water content in the GDL is controlled only by external humidification.

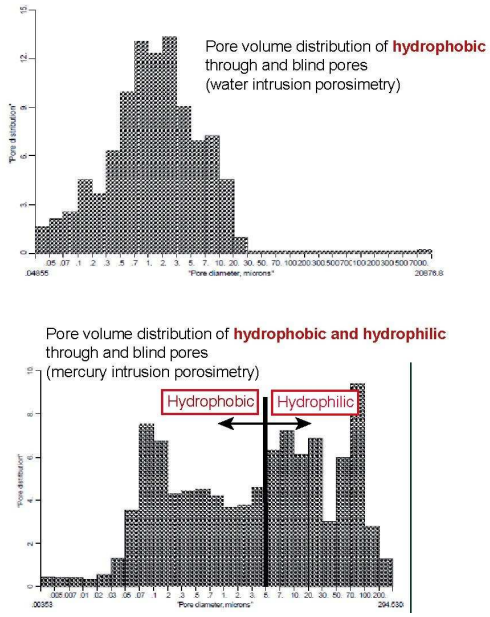

Fig. 54 Pore size distribution (modified from [155]).

Since GDL is given a hydrophobic treatment, it may be difficult for the pores to imbibe the water droplet spontaneously although in some studies deionized water was used as a working fluid [25,27]. Therefore, in the measurements, highly humidified air (relative humidity fully exceeds 100% inside the GDL) is fed into GDL to let water droplets condense and fill hopefully only the hydrophilic pores (see Fig. 55). For quantitative analysis, the humidity level of inlet gas and temperature inside the measurement system can be varied, for example, by changing the dew point temperature of the inlet gas humidifier and inserting heating elements and temperature probes.

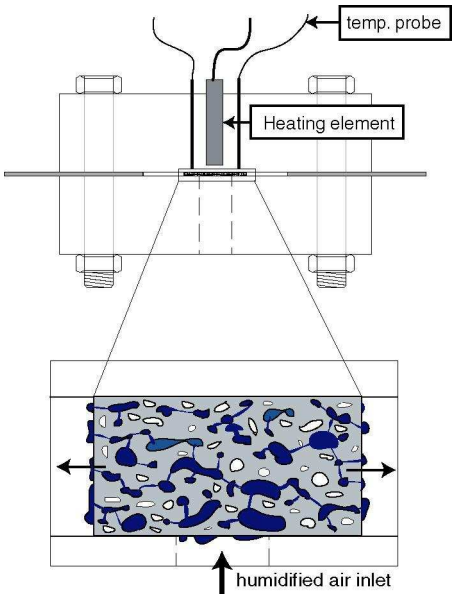

Fig. 55 A schematic of water accumulation inside GDL.

If the measurement is successful, the mass gain of GDL sample by liquid water accumulation gives information of hydrophilic pore volume. Comparing this data to the results of total pore volume (characterized with wetting fluid), the hydrophobic pore volume can be evaluated. To

study the effect of effective porosity on the compression, the measurements should be conducted with various compressed GDL thicknesses.

Relative gas-phase permeability:

Although the permeability is a geometric property, an experimental study by Dohle et al. [102] showed the permeabilities of GDL for air and water were different (see Table 7). A possible explanation is that the pores of GDL were partially filled by water due to its surface tension, which changes the pore geometry.

Table 7 Permeability of GDL [102] (Gap width indicates the compressed thickness of GDL).

Gap width s (mm)	Permeability k (m^2)	
	Air	Water
0.2	1.05E−11	–
0.3	1.41E−11	3.34E−12
0.4	1.62E−11	6.60E−12
0.5	3.33E−11	2.34E−11

This is most probably the case during normal operation of fuel cell, where humidified gas is used and water is produced in the electrochemical reaction, and thus the components are partially flooded. Therefore, the relative gas permeability, i.e. the gas permeability of partly saturated GDL, must be measured. This is a far more important parameter in two-phase modeling than the often used absolute permeability. However, no successfully evaluated values are reported, possibly because of the complexity of mechanisms involved and only computed values are reported, see e.g., [138]. There are several expressions for relative gas permeability found in the literature, see e.g., [69,143,147,191] but none of them are based on the proper assumptions. Therefore, an experimental evaluation of this parameter is worth a try.

The in-plane relative permeability may be measured by the same process employed for the absolute gas permeability measurements (see sub-chapter 3.2.2.): pressure drop is measured as a function of gas flow rate, then permeability is calculated using Darcy's law. The essential modification from the previous system is that fully humidified gas instead of dry gas will be fed to achieve two-phase conditions. Furthermore, heating elements and temperature probes must be equipped in the system to keep the humidity level constant as depicted in Fig. 55.

Challenges of this method may be that water may condense on the surface of GDL and form the water film blockage, which then causes an additional and undesirable increase in pressure drop. Special treatments to avoid or alleviate this problem must be applied, for example, having the gas inlet face down in order to remove liquid water gravitationally with hydrophilic treatment employed on the inward surface of hole. Heating elements can be inserted to the inlet so that the temperature inside the inlet is high enough to vaporize any condensed water. The relative permeability should be affected also by compression pressure since it reduces the porosity. Therefore, the measurements should be conducted with various levels of compression.

Minimization of contact resistance between GDLs

The sputtering process on the GDL surface successfully reduces the electric resistance of the measurement system (see Fig. 41). However, a question still remains if the assumption that the contact resistance between facing GDLs can be completely neglected was right. Therefore,

it is worth studying the effect of sputtering parameters, e.g. the thickness of sputtered layer or other sputtered metal, on the total resistance.

Alternatively, if the GDLs having same physical properties and different uncompressed thickness such as Toray carbon paper series are available, the sputtering process is not needed any more since contact resistances of the measurement system can be subtracted by the comparison of measured resistances with GDLs having different thicknesses, i.e. same contact resistance but different bulk resistance under the certain compression pressure, and bulk resistances can be separately calculated.

Evaluation of in-plane thermal conductivity of GDL

In the modeling study presented in sub-chapter 3.3., the in-plane thermal conductivity was assumed to be same as the through-plane conductivity. However, since carbon paper-type GDL typically consists of laterally aligned carbon fibers, the in-plane thermal conductivity can be expected to be larger than the through-plane counterpart and should be evaluated.

The measurements can be done using a fundamentally similar experimental system as in the in-plane electric conductivity measurements (see Fig. 19(b)) but replacing current leads with heating elements and coolant, and inserting temperature probes into the plastic plates which compress the GDL. The difficulty of this measurement may lie in proper thermal insulation.

Evaluation of physical properties of Gore membrane

MEA used in this study was Gore Primea series 5510. The Gore membrane is slightly different from Nafion, as it has a polymer matrix for additional structural integrity. To date, the properties of the Gore membrane are not well published compared to Nafion membrane, therefore a simple correlation was applied to estimate the membrane conductivity in the sub-chapter 3.2.6.

Experimental assessment of the Gore membrane properties, such as water uptake, ionic conductivity and thermal conductivity, would be beneficial for studying the validity of the measurement results and will be helpful for the further studies.

Effect of membrane swelling

For the evaluation of electric contact resistance between GDL and CL, the effect of membrane swelling was neglected. However, the membrane should swell when it uptakes water, and consequently the contact resistance between GDL and CL may be relatively lower than with a dry membrane, even though the compression pressure is same. Therefore, the measurements presented in sub-chapter 3.2.6 with various membrane humidity conditions are worth to be conducted.

Detailed analysis of electrode kinetics and water transport through the membrane

Thorough discussion on the electrode kinetics and water transport behavior in membrane interpreted with the AC impedance spectrum is certainly important to study the rate-limiting process, electrode structure and operating conditions. The high frequency arc in Nyquist-plot of H_2/H_2 cell (see Fig. 25) is reported to associate to the adsorption and desorption processes of hydrogen on the electrode. Also according to Meland et al. [167], the high frequency arc can be pressure dependent because the adsorption/desorption step is pressure dependent, and thus this arc can be fitted to a Gerrischer impedance. It would be interesting if the insight obtained from the Nyquist-plot presented in sub-chapter 3.2.6 supports or deviates from that reported by Meland et al. For the argument, a theoretical model as introduced, e.g. in [167],

should be developed to compare the fitted parameters such as admittance of arc and relaxation time.

Also, discussion on how water transport in the membrane can be rate-limiting is also interesting. The measurements can be done by the same procedure as described in chapter 3.2.6 by taking the DC current from the system, and changing the humidity levels and pressure of entering hydrogen at anode and cathode, and then studying how the low frequency arc of the Nyquist-plot and the fitted parameters change.

Effect of MPL and hot press on $R_{c,GDL/CL}$

In order to study the function of the MPL, the plain GDL is replaced by the GDL with MPL and the same measurement presented in publication III can be conducted. It is expected that the characterized contact resistances between GDL with MPL and CL would be smaller than those shown in Fig. 27.

Furthermore, it is fairly reasonable to presume that hot pressing process reduces the contact resistances. Comparison of the presented results in publication III with the one obtained using hot pressed sample will provide valuable insight into the role of hot pressing and the effect of compression on the contact resistance, although direct comparison might be slightly difficult because of irreversible damage of GDL during the hot pressing process.

Consideration of ionic resistance of CLs for the evaluation of $R_{c,GDL/CL}$

It may be of interest that the CL ionic resistances could be taken into account for the evaluation of contact resistance between GDL and CL in publication III. This is because the CL ionic conductivity is believed lower than that of electrolyte membrane since a CL contains ionically non-conductive substance and the volume fraction of ionomer is always lower than 1. In fact, the reported values of effective CL ionic conductivities were found to be by far lower than that of membrane [171,193]. In addition, the thickness of two CLs can be quite comparable to the membrane thickness of 25 μm for Gore Primea series 5510, although the exact thickness of CL is not found. If the thickness and ionic conductivity of CL are assumed 10 μm and 5 S/m (approximately half of membrane resistance), respectively, the sum of ionic resistance of two CLs becomes higher than the calculated membrane resistance. Furthermore, with the above assumptions, the sum of the membrane and CL resistance exceeds the measured total cell resistance.
Therefore, the discussion in publication III that the contact resistance between GDL and CL accounts for 30–70% of the total resistance may slightly overestimate the contribution of the contact resistance between GDL and CL, although the magnitude of percentage is correct.

Development of new GDL

As discussed in sub-chapter 3.3.4, local deformation of GDL causes a severe current density distribution and may affect the cell durability. Therefore, development of GDLs which are mechanically rigid and not deformed under the clamping pressure is probably needed. A MPL coating on the GDL may make the GDL more rigid [25], but typically reduces the through-plane gas permeability. Metal type GDLs such that proposed by Fushinobu et al. [63] may solve the problem of deformation, however, problems of such GDLs may be the very poor in-plane gas permeability and corrosion under acidic condition. Then metal mesh can be thought as an alternative, however with such GDL, poor contact may be a problem. Furthermore, the metal mesh may damage the CL and membrane. One possible solution of them is a coating of the metal mesh GDL with MPL to achieve intimate contact with neighboring components, although coating of metal mesh may be difficult without losing the porosity.

As discussed by Gostick et al. [138], higher in-plane relative permeability creates preferential spreading of liquid water in plane of material, which significantly reduces the gas transport in the through-plane direction. Therefore, in fact, reversed anisotropy of GDL fiber is preferred, i.e. higher through-plane permeability. In really, however development such GDL architecture with carbon fiber would be extremely difficult, thereby metal mesh GDL is again promising. The mesh structures can be designed by changing mesh diameter or the volumetric density and through-plane preferential GDL may be developed.

The metal mesh GDLs may also be useful to facilitate the water management especially at subzero temperature. According to the Ge et al. [17], the hydrophilic metal mesh wire wicks and effectively removes the liquid water from the CLs and thus to create a more favorable condition during the cold start.

Effect of GDL intrusion on flow-field pressure drop

Partial intrusion of GDL into the channel reduces the cross-section area of flow field and may increase the reactant flow-field pressure drop [70], which is of course not favorable for auxiliary power requirements. It is worth studying how much the pressure drop would be changed by the GDL intrusion into the channel. In the measurement, the combination of GDL's compressed and uncompressed thickness, gasket thickness and height of channel should be systematically studied.

Observation of GDL under extreme compression

Excessive compression pressure on soft GDLs, such as carbon cloth, may significantly deform and result in local delamination of GDL under the channel as illustrated in Fig. 56, because of cantilever mechanism as discussed by Lim et al. [97]. If this happens, current and temperature distribution over the active area would be extremely uneven because of significant variation of contact resistance between the GDL and CL. Such a situation must certainly be avoided. Visualization of such GDL deformation using optical microscope is worth a try. Careful attention should be paid to the gasket and GDL thickness and width of channel and rib, considering GDL rigidity and tensile strength during the measurement.

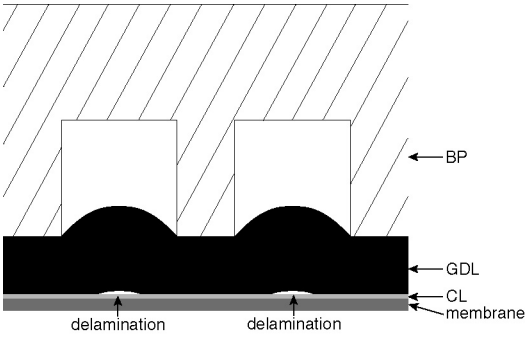

Fig. 56 Schematic of delamination of GDL.

Updating the mathematical model

To more accurately predict the temperature and current distribution, models should take into account liquid water accumulation and transport while considering the changes in physical properties of GDL by compression, reactant depletion along the channel, and water transport thought the membrane by electro-osmotic force and back-diffusion as studied in [184,185]. Furthermore, the phase change of water should also be taken into account since the local temperature is cooled by evaporation of liquid water. Recently, research on liquid water

transport especially inside the GDL and CL has become increasingly active, and therefore, a careful review of literature would be recommended.

4. Summary and Conclusions

Experimental and theoretical study of transport phenomena in a polymer electrolyte membrane (PEM) fuel cell is performed to study the effects of inhomogeneous compression of gas diffusion layers (GDLs) within the cell. The inhomogeneous compression caused by the rib/channel structure of the flow field plate leads into partial deformation of the GDLs and significantly affects material parameters.

Several physical property parameters of a commercial GDL material were experimentally evaluated. These include GDL intrusion into the channel, stress-strain behavior of GDL, gas permeability, in-plane and through-plane electric conductivities, electric contact resistances between GDL and graphite, electric contact resistance between GDL and catalyst layer (CL), through-plane thermal conductivity and thermal contact resistance between GDL and graphite as a function of compressed GDL thickness. From the experimental study, the following conclusions were drawn:

· GDL is compressed very little under the channel.

· Stress-strain curve of GDL shows one nonlinear and two linear regions

· Gas permeability decreases nonlinearly as GDL is compressed

· Electric conductivity of GDL decreases linearly as GDL is compressed

· Thermal conductivity of GDL is not affected by the compression pressure

· Both electric and thermal contact resistance between components nonlinearly decreased as GDL is compressed

· The electric contact resistance between GDL and CL is an order of magnitude larger than that between GDL and graphite

It is also worth mentioned that the magnitude of both electric and thermal bulk resistances of GDL is quite comparable to the contact resistance, contrary to the discussions in previous studies.

The results of the modeling study suggest that inhomogeneous compression does not significantly affect the polarization behavior and gas-phase mass transport. However, the effect of inhomogeneous compression on the current density distribution is evident. This is because of selective current path, which is determined by the combinations of conductivities of components and contact resistance between them. Local current density under the channel was substantially smaller than under the rib when inhomogeneous compression was taken into account, while such high current distribution was not observed with the model which excluded the effect of inhomogeneous compression. An abnormally high current density distribution may accelerate the deterioration of the membrane and is critical in terms of cell durability of fuel cell. Therefore, further effort should be devoted to mitigate the detrimental effects of inhomogeneous compression of GDL [186].

Despite the highly uneven current distribution and variation in material parameters as a function of GDL thickness, the temperature profile was fairly even over the active area for both modeled cases, contrary to the predictions in previous studies. This difference stems from the adopted modeling parameters such as contact resistance and conductivity, and the geometry of the deformed GDL. Especially the local current density distribution, which significantly affects the temperature profile, was found to be very sensitive to the value and variation of contact resistance between GDL and CL.

It is certain that the each GDL has unique physical properties and the modeling parameters adopted here can be applied only to the GDL that the authors used. However, the methods applied in this study should be valid for testing most materials. The right choice of modeling parameters is essential for accurate prediction of local phenomena which can not be easily

interpreted by the modeled polarization curves only, as discussed in literature [187-190] and shown also in this thesis. This is because the overall polarization curve is a synthesized outcome of many influencing modeling parameters, among which some have a positive effect while others have a negative effect. This finding highlights the importance of detailed knowledge of the cell component properties in realistic operating conditions.

The insight obtained from this study is highly beneficial for development and construction of fuel cells, as well as predicting their performance and life time. In future studies, liquid water transport should also be taken into account to obtain the accurate picture of local phenomena in the fuel cells.

Nomenclature

a_v	ratio of reaction surface to CL volume (m^{-1})
c	molar concentration (mol m^{-3})
C_p	Heat capacity (J kg^{-1} K^{-1})
D	diffusion coefficient (m^2 s^{-1})
n	unit vector
F	Faraday constant, 96487 (As mol^{-1})
h	thickness (m)
j	transfer current density (A m^{-3})
j^{ref}	exchange current density (A m^{-2})
k	permeability (m^2)
M	molar mass (kg mol^{-1})
N	molar flux (mol $m^{-2}s^{-1}$)
p	pressure (Pa)
Q	heat flux (W m^{-2})
r	radius (m)
R	electric resistance (Ω m^2)
S	Source term
T	temperature (K)
v	velocity (m s^{-1})
w	channel and rib width (m)
X	molar fraction

Greek letters

α	transfer coefficient
γ	surface tension
ε	porosity
η	overpotential (V)
κ	thermal conductivity (W m^{-1} K^{-1})
θ	contact angle
μ	viscosity of air, 1.9×10^{-5} (kg m^{-1} s^{-1})
ρ	density (kg m^{-3})
σ	electric conductivity (Ω^{-1} m^{-1})
ϕ_s	electric potential (V)
ϕ_m	ionic potential (V)
Γ	thermal resistance (m^2 K W^{-1})
λ	water content in membrane
$\Re$	gas constant, 8.314 (J mol^{-1} K^{-1})

Subscripts

a	anode
b	bulk
c	cathode
c,GR/GDL	interface between graphite and GDL
c,GDL/CL	interface between GDL and CL
CL	catalyst layer
g	gas phase
GDL	gas diffusion layer
GR	graphite
H_2	hydrogen
H_2O	water
HE	heating element
i	species of gas

l	liquid phase
m	ionic phase
mem	membrane
N_2	nitrogen
O_2	oxygen
s	electric phase
sat	saturation
sd	subdomain
t	mixture of gas
T	temperature
TH1	thin layer 1
TH2	thin layer 2
x	x-direction, in-plane
y	y-direction, through-plane

References

1 MPR Associates, Inc., MPR-WP-0001, Revision 0, (2005), Hydrogen Production Methods

2 A. Ersoz, H. Olgun, S.Ozdogan, J. Power Sources 154 (2006) 67–73. Reforming options for hydrogen production from fossil fuels for PEM fuel cells

3 S. Saito, Atomic Energy Commission of Japan, Policy Debate of The Potential Contribution of Nuclear Energy to Production of Hydrogen, (2004)

4 Frano Barbir, PEM Fuel Cells - Theory and Practice, Academic Press July 2005

5 M.A.J. Cropper, S. Geiger, D.M. Jollie, J. Power Sources 131 (2004) 57–61. Fuel cells: a survey of current developments

6 Japanese Economy Division, JETRO Japan Economic Report, April-May 2006, Japan's Fuel Cell Industry

7 EG&G Services. Fuel Cell Handbook. Parsons, Inc., Morgantown,West Virginiak, 2000.

8 M.M. Mench, C. Y. Wang, J. Electrochem. Soc. 150 (1) A79–A85 (2003). An In Situ Method for Determination of Current Distribution in PEM Fuel Cells Applied to a Direct Methanol Fuel Cell

9 J. Ge, H. Liu, J. Power Sources 163 (2007) 907–915. A three-dimensional two-phase flow model for a liquid-fed direct methanol fuel cell

10 G. Lin, W. He, T.V. Nguyen, J. Electrochem. Soc. 151 (2004) A1999–A2006. Modeling liquid water effects in the gas diffusion and catalyst layers of the cathode of PEM fuel cell

11 G. Lin, T.V.Nguyen, J. Electrochem. Soc. 152 (2005) A1942–A1948. Effect of Thickness and Hydrophobic Polymer Content of the Gas Diffusion Layer on Electrode Flooding Level in a PEMFC

12 D. Natarajan, T.V. Nguyen, J. Electrochem. Soc. 148 (2001) A1324–A1335. A Two-Dimensional, Two-Phase, Multicomponent, Transient Model for the Cathode of a Proton Exchange Membrane Fuel Cell Using Conventional Gas Distributors

13 D. Natarajan, T.V. Nguyen, J. Power Sources 115 (2003) 66–80. Three-dimensional effects of liquid water flooding in the cathode of a PEM fuel cell

14 N.P. Siegel, M.W. Ellis, D.J. Nelson, M.R. Spakovsky, J. Power Sources 128 (2004) 173–184. A two-dimensional computational model of a PEMFC with liquid water transport

15 Z.H. Wang, C.Y. Wang, K.S. Chen, J. Power Sources 94 (2001) 40–50. Two-phase flow and transport in the air cathode of proton exchange membrane fuel cells

16 M. Oszcipok, D. Riemann, U. Kronenwett, M. Kreideweis, M. Zedda, J. Power Sources, 145 (2005) 407–415. Statistic analysis of operational influences on the cold start behaviour of PEM fuel cells

17 S. Ge. C-Y. Wang, Electrochem. Solid-State Lett., 9 (11) (2006) A499–A503. In Situ Imaging of Liquid Water and Ice Formation in an Operating PEFC during Cold Start

18 X. G. Yang, F. Y. Zhang, A. L. Lubawy, and C. Y. Wang, Electrochemical and Solid-State Letters, 7 A408–A411 (2004). Visualization of Liquid Water Transport in a PEFC

19 F. Y. Zhang, X. G. Yang, and C. Y. Wang, J. Electrochem. Soc., 153, A225–A232 (2006). Liquid Water Removal from a Polymer Electrolyte Fuel Cell

20 J.H. Nam, M. Kaviany, Int. J. Heat Mass Transfer 46 (2003) 4595–4611. Effective diffusivity and water-saturation distribution in single- and two-layer PEMFC diffusion medium

21 D. Bevers, R. Rogers, M.V. Bradke, J. Power Sources 63 (1996) 193–201. Examination of the influence of PTFE coating on the properties of carbon paper in PEFCs

22 C. Lim, C.Y. Wang, Electrochim. Acta 49 (2004) 4149–4156. Effects of hydrophobic polymer content in GDL on power performance of a PEM fuel cell

23 L. Giorgi, E. Antolini, A. Pozio, E. Passalacqua, Electrochimi. Acta, 43 (1998) 3675–3680. Influence of the PTFE content in the diffusion layer of low-Pt loading electrodes for polymer electrolyte fuel cells

24 E.C. Kumbur, K.V. Sharp, M.M. Mench, J. Electrochem. Soc. 154 (12) B1295–B1304 (2007). Validated Leverett Approach for Multiphase Flow in PEFC Diffusion Media I. Hydrophobicity Effect

25 E.C. Kumbur, K.V. Sharp, M.M. Mench, J. Electrochem. Soc. 154 (12) B1305–B1314 (2007). Validated Leverett Approach for Multiphase Flow in PEFC Diffusion Media II. Compression Effect

26 E.C. Kumbur, K.V. Sharp, M.M. Mench, J. Electrochem. Soc. 154 (12) B1315–B1324 (2007). Validated Leverett Approach for Multiphase Flow in PEFC Diffusion Media III. Temperature Effect and Unified Approach
27 E.C. Kumbur, K.V. Sharp and M.M. Mench, J. Power Sources, In Press, Accepted Manuscript, (2007), A Design tool for predicting the capillary transport characteristics of fuel cell diffusion media using an artificial neural network
28 T.A. Zawodzinski, C. Derouin, S. Radzinski, R.J. Sherman, V.T. Smith, T.E. Springer, S. Gottesfeld, J. Electrochem. Soc. 140 (4) (1993) 1041–1047. Water Uptake by and Transport Through Nation 117 Membranes
29 S. Cleghorn, J. Kolde, W. Liu, Handbook of Fuel Cells – Fundamentals, Technology and Applications, Edited by Wolf Vielstich, Hubert A. Gasteiger, Arnold Lamm. Volume 3: Fuel Cell Technology and Applications. 2003 John Wiley & Sons, Ltd.
30 L. Mao, K. Tajiri, S. Ge, X. G. Yang, and C. Y. Wang, Abstract 998, The Electrochemical Society Meeting Abstracts, Vol. 2005-2, Los Angeles, CA, Oct. 16-21, 2005.
31 K. Wiezell, P. Gode, G. Lindbergh, J. Electrochem. Soc. 153 (4) (2006) A759–A764. Steady-State and EIS Investigations of Hydrogen Electrodes and Membranes in Polymer Electrolyte Fuel Cells II. Experimental
32 M. Grujicic, K.M. Chittajallu, Chem. Eng. Sci. 59 (2004) 5883–5895. Optimization of the cathode geometry in polymer electrolyte membrane (PEM) fuel cells
33 F.Y. Zhang, X. G. Yang, and C. Y. Wang, J. Electrochem. Soc. 153 (2006) A225–A232. Liquid Water Removal from a Polymer Electrolyte Fuel Cell
34 U. Pasaogullari, C.Y. Wang, J. Electrochem. Soc. 151 (2004) A399–A406. Liquid Water Transport in Gas Diffusion Layer of Polymer Electrolyte Fuel Cells
35 J.J. Baschuk, Xianguo Li, J. Power Sources 142 (2004) 134–153. A general formulation for a mathematical PEM fuel cell model
36 S. Mazumder, J.V. Cole, J. Electrochem. Soc. 150 (11) (2003) A1510–A1517. Rigorous 3-D Mathematical Modeling of PEM Fuel Cells II. Model Predictions with Liquid Water Transport, J. Electrochemical Society
37 T. Berning, N. Djilaliz, J. Electrochem. Soc., 150 (12) A1589–A1598 (2003). A 3D, Multiphase, Multicomponent Model of the Cathode and Anode of a PEM Fuel Cell
38 F. Barbir, H. Gorgon, X. Wang, J. Power Sources 141 (2005) 96–101. Relationship between pressure and cell resistance as diagnostic tool for PEM fuel cells
39 J.M. Canut, R.M. Abouatallah, D.A. Harrington, J. Electrochem. Soc. 153 (5) A857–A864 (2006). Detection of Membrane Drying, Fuel Cell Flooding, and Anode catalyst poisoning
40 I.A. Schneider, D. Kramer, A. Wokaun, G.G. Scherer, Electrochemistry Communications 7 (2005) 1393–1397. Spatially resolved characterization of PEFCs using simultaneously neutron radiography and locally resolved impedance spectroscopy
41 J. Zhang, D. Kramer, R. Shimoi, Y. Ono, E. Lehmann, A. Wokaun, K. Shinohara, G.G. Scherer, Electrochim. Acta 51 (2006) 2715–2727. In situ diagnostic of two-phase flow phenomena in polymer electrolyte fuel cells by neutron imaging Part B. Material variations
42 P.K. Sinha, P. Halleck, C.Y. Wang, Electrochem. Solid-State Lett 9 (7) A344–A348 (2006). Quantification of Liquid Water Saturation in a PEM Fuel Cell Diffusion Medium Using X-ray Microtomography
43 M. Coppo, N.P. Siegel, M.R. Spakovsky, J. Power Sources 159 (2006) 560–569. On the influence of temperature on PEM fuel cell operation
44 K.Z Yao, K. Kran, K.B. McAuley, P. Oosthuizen, B. Peppley, T. Xie, Fuel Cell 4 (1) (2004) 3–29., A Review of Mathematical Models for Hydrogen and Direct Methanol Polymer Electrolyte Membrane.
45 M. Noponen, E. Birgersson, J. Ihonen, M. Vynnycky, A. Lundblad, G. Lindbergh, Fuel Cells 4 (4) (2004) 365–377. A Two phase non isothermal PEFC model Theory and validation
46 H. Ju, C.Y. Wang, S. Cleghorn, U. Beuscher, J. Electrochem. Soc. 152 (8) (2005) A1645–A1653. Nonisothermal Modeling of Polymer Electrolyte Fuel Cells I. Experimental Validation
47 J. Ihonen, Ph.D thesis 2003, KTH, Sweden.
48 M. Cai, M.S. Ruthkosky, B. Merzougui, S. Swathirajan, M.P. Balogh, S.H. Oh, J. Power Sources 160 (2006) 977–986., Investigation of thermal and electrochemical degradation of fuel cell catalysts
49 R. Shimoi, M. Masuda, K. Fushinobu, Y. Kozawa, K. Okazaki, J. Fuel Cell Sci. Technol. 126 2004) 258–261.Visualization of the Membrane Temperature Field of a Polymer Electrolyte Fuel Cell

50 S. Haufe, U. Stimming, J. Membrane Science 185 (2001) 95–103. Proton conducting membranes based on electrolyte filled microporous matrices
51 R.W. Kopitzke, C.A. Linkous, H.R. Anderson, G.L. Nelson, J. Electrochem. Soc. 147 (2000) 1677–1681. Conductivity and Water Uptake of Aromatic-Based Proton Exchange Membrane
52 T.A. Zawodzinski, T.E. Springer, J. Davey, R. Jestel, C. Lopez, J. Valeria, S. Gottesfeld, J. Electrochem. Soc. 140 (7) (1993) 1981–1985. A Comparative Study of Water Uptake By and Transport Through Ionomeric Fuel Cell Membranes
53 Y. Sone, P. Ekdunge, D. Simonsson, J Electrochem. Soc. 143 (4) (1996) 1254–1259. Proton Conductivily of Nafion 117 as Measured by a Four-Electrode AC Impedance Method
54 Nafion product sheet, Dupont NAE101, 2004
55 R. Fern´andez, P.F. Aparicio, L. Daza, J. Power Sources 151 (2005) 18–24. PEMFC electrode preparation: Influence of the solvent composition and evaporation rate on the catalytic layer microstructure
56 T.E. Springer, M.S. Wilson, S. Gottesfeld, J. Electrochem. Soc. 140 (1993) 3513–3526. Modeling and Experimental Diagnostics in Polymer Electrolyte Fuel Cells
57 X. Yu, S. Ye, J. Power Sources 172 (2007) 145–154. Recent advances in activity and durability enhancement of Pt/C catalytic cathode in PEMFC: Part II: Degradation mechanism and durability enhancement of carbon supported platinum catalyst
58 W. Li, C. Liang, W. Zhou, J. Qiu, Z. Zhou, G. Sun, Q.Xin, J. Phys. Chem. B 2003, 107, 6292–6299. Preparation and Characterization of Multiwalled Carbon Nanotube-Supported Platinum for Cathode Catalysts of Direct Methanol Fuel Cells
59 U.A. Paulus 1, Z. Veziridis 2, B. Schnyder, M. Kuhnke, G.G. Scherer, A. Wokaun, J. Electroanal. Chem. 541 (2003) 77. Fundamental investigation of catalyst utilization at the electrode/solid polymer electrolyte interface
60 M. Watanabe, Handbook of Fuel Cells – Fundamentals, Technology and Applications Vol.2 Chap.28 (2003) –New CO-tolerant catalyst concepts
61 R. Bashyam, P. Zelenay, Nature 443 (7107) (2006) 63–66. A class of non-precious metal composite catalysts for fuel cells
62 C. Ziegler, H.M. Yu, J.O. Schumacher, J. Electrochem. Soc. 152 (8) (2005) A1555–A1567. Two-Phase Dynamic Modeling of PEMFCs and Simulation of Cyclo-Voltammograms
63 K. Fushinobu, D. Takahashi, K. Okazaki, J. Power Sources 158 (2006) 1240–1245. Micromachined metallic thin films for the gas diffusion layer of PEFCs
64 E. Antolini, R.R. Passos, E.A. Ticianelli, J. Power Sources 109 (2002) 477–482. Effects of the carbon powder characteristics in the cathode gas diffusion layer on the performance of polymer electrolyte fuel cells
65 M. Mathias, J. Roth, J. Fleming, W. Lehnert, Handbook of Fuel Cells Fundamentals, Technology and Applications, Volume 3 Chap. 46 2003 517–537, John Wiley & Sons, Ltd.
66 U. Pasaogullari, C.Yang Wang, Electrochim. Acta 49 (2004) 4359–4369. Two-phase transport and the role of micro-porous layer in polymer electrolyte fuel cells
67 N. Holmström, J. Ihonen, A. Lundblad, G. Lindbergh, Fuel Cells 7 (4) (2007) 306–313. The influence of the Gas Diffusion Layer on Water Management in Polymer Electrolyte Fuel Cells
68 V. Gurau, M.J. Bluemle, E.S.D. Castro, Y-M. Tsou, J.A.Mann, T.A. Zawodzinski, J. Power Sources 160 (2006) 1156–1162. Characterization of transport properties in gas diffusion layers for proton exchange membrane fuel cells 1. Wettability (internal contact angle to water and surface energy of GDL fibers)
69 J.T. Gostick, M.W. Fowler, M.A. Ioannidis, M.D. Pritzker, Y.M. Volfkovich, A. Sakars, J. Power Sources 156 (2006) 375–387. Capillary pressure and hydrophilic porosity in gas diffusion layers for polymer electrolyte fuel cells
70 E.C. Kumbur, K.V. Sharp, M.M. Mench, J. Power Sources 161 (2006) 333–345. Liquid droplet behavior and instability in a polymer electrolyte fuel cell flow channel
71 Atul Kumara, Ramana G. Reddy, J. Power Sources 129 (2004) 62–67. Materials and design development for bipolar/end plates in fuel cells
72 H. Wang, M.A. Sweikart, J.A. Turner, Journal of Power Sources 115 (2003) 243–251. Stainless steel as bipolar plate material for polymer electrolyte membrane fuel cells
73 C.H.B. Steele, A. Heinzel, Nature 414 (2001) 345–352. Materials for fuel cell technologies
74 R.C. Makkus, A.H.H. Janssen, F.A. Bruijn, R.K.A.M. Mallant, J. Power Sources 86 (2000) 274–282. Use of stainless steel for cost competitive bipolar plates in the SPFC
75 P.L. Hentall, J.B. Lakeman, G.O. Mepsted, P.L. Adcock, J.M. Moore, J. Power Sources 80 (1999) 235- New materials for polymer electrolyte membrane fuel cell current collectors
76 Honda press information (2004)

77 Robert Rose, www.fuelcells.org
78 International Partnership for the Hydrogen Economy, Fuel Cells: A Hydrogen Enabling Technology
79 R.V. Helmolt, U. Eberle, J. Power Sources 165 (2007) 833–843. Fuel cell vehicles: Status 2007
80 L. Mao, C-Y Wang, Y. Tabuchi, J. Electrochem. Soc. 154 (3) B341–B351 (2007). A Multiphase Model for Cold Start of Polymer Electrolyte Fuel Cells
81 K. Tajiri, Y.o Tabuchi,a C.Y. Wang, J. Electrochem. Soc., 154 (2) B147–B152 (2007). Isothermal Cold Start of Polymer Electrolyte Fuel Cells
82 K. Tajiri, Y. Tabuchi, F. Kagami, S. Takahashi, K. Yoshizawa, C.Y. Wang, J. Power Sources 165 (2007) 279–286. Effects of operating and design parameters on PEFC cold start
83 T. Takaichi, P2005–166596A written in Japanese
84 X. Cheng, Z. Shi, N. Glass, L. Zhang, J. Zhang, D. Song, Z.S. Liu, H. Wang, J. Shen, J. Power Sources 165 (2007) 739–756. A review of PEM hydrogen fuel cell contamination: Impacts, mechanisms, and mitigation
85 Fuel Cell Today, K-A. Adamson, (2006). Infrastructure Survey
86 W. Iwasaki, T. Kaneko, Y. Sakata, Toshiba review, 62, 2 (2007). Large-Scale Stationary Fuel Cell Demonstration Project and Hydrogen-Fuel PEFC
87 T. Omata, New Energy Foundation Japan, Current Status of Stationary Fuel Cell Demonstration Study in Japan (2005).
88 M. Uzunoglu, O.C. Onar, M.S. Alam, J. Power Sources 168 (2007) 240–250. Dynamic behavior of PEM FCPPs under various load conditions and voltage stability analysis for stand-alone residential applications
89 S.J.C. Cleghorn, D.K. Mayfield, D.A. Moore, J.C. Moore, G. Rusch, T.W. Sherman, N.T. Sisofo, U. Beuscher, J. Power Sources 158 (2006) 446–454.
90 Fuel Cell Today, K-A. Adamson, (2006). Portable Survey
91 A. Kundu, J.H. Jang, J.H. Gil, C.R. Jung, H.R. Lee, S.-H. Kim, B. Ku, Y.S. Oh, J. Power Sources 67–78. Micro-fuel cells-Current development and applications
92 Y. Zhang, A. Mawardi, R. Pitchumani, J. Power Sources 173 (2007) 264–276. Numerical studies on an air-breathing proton exchange membrane (PEM) fuel cell stack
93 A.S. Patil, T.G. Dubois, N. Sifer, E. Bostic, K. Gardner, M. Quah, C. Bolton, J. Power Sources 136 (2004) 220–225. Portable fuel cell systems for America's army: technology transition to the field
94 W.K. Lee, C.H. Ho, J.W.V. Zee, M. Murthy, J. Power Sources 84 (1999) 45–51. The effects of compression and gas diffusion layers on the performance of a PEM fuel cell
95 J. Ge, A. Higier, H. Liu, J. Power Sources 159 (2006) 922–927. Effect of gas diffusion layer compression on PEM fuel cell performance
96 J. Ihonen, M. Mikkola, G. Lindbergh, J. Electrochem. Soc. 151 (8) (2004) A1152–A1161. Flooding of Gas Diffusion Backing in PEFCs Physical and Electrochemical Characterization
97 C. Lim, C.Y. Wang, J. Power Sources 113 (2003) 145–150. Development of high-power electrodes for liquid-feed direct methanol fuel cell
98 W.R. Chang, J.J. Hwang, F.B. Weng, S.H. Chan, J. Power Sources 166 (2007) 149–154. Effect of clamping pressure on the performance of a PEM fuel cell
99 L.R. Jordan, A.K. Shukla, T. Behrsing, N.R. Avery, B.C. Muddle, M. Forsyth, J. Power Sources 86 (2000) 250–254. Diffusion layer parameters influencing optimal fuel cell performance
100 H.K. Lee, J.H. Park, D.Y. Kim, T.H. Lee, J. Power Sources 131 (2004) 200–206. A study on the characteristics of the diffusion layer thickness and porosity of the PEMFC
101 M. Prasanna, H.Y. Ha, E.A. Cho, S.A. Hong, I.H. Oh, J. Power Sources 131 (2004) 147–154. Influence of cathode gas diffusion media on the performance of the PEMFCs
102 H. Dohle, R. Jung, N. Kimiaie, J. Mergel, M. Müller, J. Power Sources 124 (2003) 371–384. Interaction between the diffusion layer and the flow field of polymer electrolyte fuel cells—experiments and simulation studies
103 V. Gurau, M.J. Bluemle, E.S. De Castro, Y-M Tsou, T.A. Zawodzinski, J.A. Mann., J. Power Sources 165 (2007) 793–802. Characterization of transport properties in gas diffusion layers for proton exchange membrane fuel cells 2. Absolute permeability
104 J.T. Gostick, M.W. Fowler, M.D. Pritzker, M.A. Ioannidis, L.M. Behra, J. Power Sources 162 (2006) 228–238. In-plane and through-plane gas permeability of carbon fiber electrode backing layers

105 J.P. Feser, A.K. Prasad, S.G. Advani, J. Power Sources, 162 (2006) 1226–1231. Experimental characterization of in-plane permeability of gas diffusion layers
106 C. Lee, W. Mérida, J. Power Sources 164 (2007) 141–153. Gas diffusion layer durability under steady-state and freezing conditions
107 M.V. Williams, E. Begg, L. Bonville, H.R. Kunz, J.M. Fenton, J. Electrochem. Soc. 151 (8) (2004) A1173–A1180. Characterization of Gas Diffusion Layers for PEMFC
108 C. Xu, T.S. Zhao, Q. Ye, Electrochim. Acta 51 (2006) 5524–5531. Effect of anode backing layer on the cell performance of a direct methanol fuel cell
109 J. Soler, E. Hontanon, L. Daza, J. Power Sources 118 (2003) 172–178. Electrode permeability and flow-field configuration: influence on the performance of a PEMFC
110 S.A. Freunberger, M. Reum, J. Evertz, A. Wokaun F.N. Büchia, J. Electrochem. Soc. 153 (2006) A2158–A2165. Measuring the Current Distribution in PEFCs with Sub-Millimeter Resolution I. Methodology
111 T. Tomimura, S. Nakamura, H. Nonami, H. Saito, 2001 IEEE 7th International Conference on Solid Dielectrics, (2001) 101–104. Resistivity of Elastic Separator used in PEFC and Evaluation of Contact Resistance between Separator and Electrode Sheet
112 V. Mishra, F. Yang, R. Pitchumani, J. Fuel Cell Sci. Technol. 1 (2004) 2–9. Measurement and prediction of electrical contact resistance between gas diffusion layers and bipolar plate for applications to PEM fuel cells
113 J. Ihonen, F. Jaouen, G. Lindbergh, G. Sundholm, Electrochim. Acta 46 (2001) 2899–2911. A novel polymer electrolyte fuel cell for laboratory investigations and in-situ contact resistance measurements
114 N. Cunningham, M. Lefévre, G. Lebrun, J.P. Dodelet, J. Power Sources 143 (2005) 93–102. Measuring the through-plane electrical resistivity of bipolar plates (apparatus and methods)
115 M. Khandelwal, M.M. Mench, J. Power Sources 161 (2006) 1106–1115. Direct measurement of through-plane thermal conductivity and contact resistance in fuel cell materials
116 P.J.S. Vie, S. Kjelstrup, Electrochim. Acta 49 (2004) 1069–1077. Thermal conductivities from temperature profiles in the polymer electrolyte fuel cell
117 S. Lister, D. Sinton, N. Djilali, J. Power Sources 154 (2006) 95–105. Ex situ visualization of liquid water transport in PEM fuel cell gas diffusion layers
118 A. Bazylak, D. Sinton, Z.S. Liu, N. Djilali, J. Power Sources 163 (2007) 784–792. Effect of compression on liquid water transport and microstructure of PEMFC gas diffusion layers
119 J. Benziger, J. Nehlsen, D. Blackwell, T. Brennan, J. Itescu, J. Membr. Sci. 261 (2005) 98–106. Water flow in the gas diffusion layer of PEM fuel cells
120 D. Natarajan, T.V. Nguyen, J. Power Sources 135 (2004) 95–109. Effect of electrode configuration and electronic conductivity on current density distribution measurements in PEM fuel cells
121 H. Wang, J.A. Turner, J. Power Sources 128 (2004) 193–200. Ferritic stainless steels as bipolar plate material for polymer electrolyte membrane fuel cell
122 P. M. Wilde, M. Mandle, M. Murata, N. Berg, Fuel Cells 4 (3) (2004) 180–184. Structural and Physical Properties of GDL and GDL/BPP Combinations and Their Influence on PEMFC Performance
123 Y. Zhou, G. Lin, A.J. Shih, S.J. Hu, J. Power Sources 163 (2007) 777–783. A micro-scale model for predicting contact resistance between bipolar plate and gas diffusion layer in PEM fuel cells
124 F. Barbir, J. Braun, J. Neutzler, J. New Mat. Elect. Syst. 2 (1999) 197–200. Properties of Molded Graphite Bi-Polar for PEM Fuel Cell stacks
125 S. Miachon, P. Aldebert, J. Power Sources 56 (1995) 31–36. Internal hydration Hz/O2 100 cm2 polymer electrolyte membrane fuel cell
126 S. Escribano, J.F. Blachot, J. Etheve, A. Morin, R. Mosdale, J. Power Sources 156 (2006) 8–13. Characterization of PEMFCs gas diffusion layers
127 T. Matsuura, M. Kato, M. Hori, J. Power Sources 161 (2006) 74–78. Study on metallic bipolar plate for proton exchange membrane fuel cell
128 T. Hottinen, O. Himanen, S. Karvonen, I. Nitta, J. Power Sources 171 (2007) 113–121.
129 P. Zhou, C.W. Wu, J. Power Sources 170 (2007) 93–100. Numerical study on the compression effect of gas diffusion layer on PEMFC performance
130 J.G. Pharoah, K. Karan, W. Sun, J. Power Sources 161 (2006) 214–224. On effective transport coefficients in PEM fuel cell electrodes: Anisotropy of the porous transport layers
131 T. Zhou, H. Liu, J. Power Sources 161 (2006) 444–453. Effects of the electrical resistances of the GDL in a PEM fuel cell

132 H. Meng, C.Y. Wang, J. Electrochem. Soc. 151 (2004) A358–A367. Electron Transport in PEFCs
133 J.H. Jang, W.M. Yan, C.C. Shih, J. Power Sources 156 (2006) 244–252. Numerical study of reactant gas transport phenomena and cell performance of proton exchange membrane fuel cells
134 G. Inoue, Y. Matsukuma, M. Minemoto, J. Power Sources 154 (2006) 8–17. Evaluation of the thickness of membrane and gas diffusion layer with simplified two-dimensional reaction and flow analysis of polymer electrolyte fuel cell
135 J.H. Jang, W.M. Yan, C.C. Shih, J. Power Sources 161 (2006) 323–332. Effects of the gas diffusion-layer parameters on cell performance of PEM fuel cells
136 Z. Liu, Z. Mao, C. Wang, J. Power Sources 158 (2006) 1229–1239. A two dimensional partial flooding model for PEMFC
137 H.S. Chu, C. Yeh, F. Chen, J. Power Sources. 123 (2003) 1–9. Effects of porosity change of gas diffuser on performance of proton exchange membrane fuel cell
138 J.T. Gostick, M.A. Ioannidis, M.W. Fowler, M.D. Pritzker, J. Power Sources, in press, Pore network modeling of fibrous gas diffusion layers for polymer electrolyte membrane fuel cells
139 J.G. Pharoah, J. Power Sources 144 (2005) 77–82. On the permeability of gas diffusion media used in PEM fuel cells
140 A.S. Rawool, S.K. Mitra, J.G. Pharoah, J. Power Sources 162 (2006) 985–991. An investigation of convective transport in micro proton-exchange membrane fuel cells
141 X. Zhu, P.C. Sui, N. Djilali, J. Power Sources 172 (2007) 287–295. Dynamic behaviour of liquid water emerging from a GDL pore into a PEMFC gas flow channel
142 X.D. Niu, T. Munekata, S.A. Hyodoa, K. Suga, J. Power Sources, in press. An investigation of water-gas transport processes in the gas-diffusion-layer of a PEM fuel cell by a multiphase multiple-relaxation-time lattice Boltzmann model
143 W. He, J.S. Yi T.V. Nguyen, AIChE 46 (10) (2000) 2053–2064. Two-Phase Flow Model of the Cathode of PEM Fuel Cells Using Interdigitated Flow Fields
144 P.C. Sui, N. Djilali, J. Power Source 161 (2006) 294–300. Analysis of coupled electron and mass transport in the gas diffusion layer of a PEM fuel cell
145 G. Hu, J. Fan, S. Chen, Y. Liu, K. Cen, J. Power Sources 136 (2004) 1–9. Three-dimensional numerical analysis of proton exchange membrane fuel cells (PEMFCs) with conventional and interdigitated flow fields-
146 T. Berning, N. Djilali, J. Power Sources 124 (2003) 440–452. Three-dimensional computational analysis of transport phenomena in a PEM fuel cell—a parametric study
147 L. You, H. Liu, Int. J. Heat Mass Transfer, 45 (2002) 2277–2287. A two-phase flow and transport model for the cathode of PEM fuel cells
148 S S.J. Lee, C.D. Hsu, C.H. Huang, J. Power Sources 145 (2005) 353–361. Analyses of the fuel cell stack assembly pressure
149 P. Zhou, C.W. Wu, G.J. Ma, J. Power Sources 159 (2006) 1115–1122. Contact resistance prediction and structure optimization of bipolar plates
150 V.P. Schulz, J. Becker, A. Wiegmann, P.P. Mukherjee, C.Y Wang, J. Electrochem. Soc. 154 (2007) B419–B426. Modeling of Two-Phase Behavior in the Gas Diffusion Medium of PEFCs via Full Morphology Approach
151 L. Zhang, Y. Liu, H. Song, S. Wang, Y. Zhou, S.J. Hu, J. Power Sources 162 (2006) 1165–1171. Estimation of contact resistance in proton exchange membrane fuel cells.
152 P. Zhou, C.W. Wu, G.J. Ma, J. Power Sources 163 (2007) 874–881. Influence of clamping force on the performance of PEMFCs
153 W. Sun, B.A. Peppley, K. Karan, J. Power Sources 144 (2005) 42–53. Modeling the influence of GDL and flow-field plate parameters on the reaction distribution in the PEMFC cathode catalyst layer
154 Manufacturer's data sheet for ®Sigracet GDL 10 BA by SGL Carbon AG
155 A. Jena, K. Gupta, Characterization of Pore Structure of Fuel Cell Components Containing Hydrophobic and Hydrophilic Pores, 41st Power Sources Conference, 2005.
156 M. Yamaguchi, N. Matsuo, S. Uozumi, Japanese patent H6–84529 (in Japanese)
157 K. Kodama, Japanese patent P2004–178893A (in Japanese)
158 A. Caillard, P. Brault, J. Mathias, C. Charlesb, R.W. Boswellb, T. Sauvage, Surf. Coat. Tech. 200 (2005) 391–394. Deposition and diffusion of platinum nanoparticles in porous carbon assisted by plasma sputtering

159 X. Yuan, J.C. Sun, M. Blanco, H. Wang, J. Zhang, D.P. Wilkinson, J. Power Sources 161 (2006) 920–928. AC impedance diagnosis of a 500W PEM fuel cell stack Part I: Stack impedance
160 W.H. Zhu, R.U. Payne, B.J. Tatarchuk, J. Power Sources 168 (2007) 211–217. PEM stack test and analysis in a power system at operational load via ac impedance
161 K.L. Huang, Y.C Lai, C.H Tsai, Journal of Power Sources 156 (2006) 224–231. Effects of sputtering parameters on the performance of electrodes fabricated for proton exchange membrane fuel cells
162 M. Ciureanu, S.D. Mikhailenko, S. Kaliaguine, Catal. Today 82 (2003) 195–206. PEM fuel cells as membrane reactors: kinetic analysis by impedance spectroscopy
163 H. Matic, A. Lundblad, G. Lindbergh, P. Jacobsson, Electrochem. Solid-State Lett. (2005) A5–A7. In Situ Micro-Raman on the Membrane in a Working PEM Cell
164 N. Wagner, W. Schnurnberger, B. MuÈ ller, M. Lang, Electrochim. Acta, 43 (1998) 3785–3793. Electrochemical impedance spectra of solid-oxide fuel cells and polymer membrane fuel cells
165 K. Wiezell, P. Gode, G. Lindbergh, J. Electrochem. Soc. 153 (2006) A759–A764. Steady-State and EIS Investigations of Hydrogen Electrodes and Membranes in Polymer Electrolyte Fuel Cells II. Experimental
166 O. Himanen, T. Hottinen, M. Mikkola, V. Saarinen, Electrochimica Acta 52 (2006) 206–214. Characterization of membrane electrode assembly with hydrogen–hydrogen cell and ac-impedance spectroscopy Part I. Experimental
167 A.K. Meland, D. Bedeaux, S. Kjelstrup, J. Phys. Chem. B 2005, 109, 21380–21388, A Gerischer Phase Element in the Impedance Diagram of the Polymer Electrolyte Membrane Fuel Cell Anode†
168 T. Thampan, S. Malhotra, H. Tang, R. Datta, J. Electrochem. Soc. 147 (9) 3242–3250 (2000). Modeling of Conductive Transport in Proton-Exchange Membranes for Fuel Cells
169 J. Kolde, B. Bahar, M.Wilson, T. Zawodzinski, S. Gottesfeld, Proc. 1st International Symp on Proton Conducting Membrane Fuel Cells. Proc. – Electrochem. Soc., 95, 1995, p. 193.
170 T.E. Springer, T.A. Zawodzinski, S. Gottesfeld, J. Electrochem. Soc.138 (8) (1991) 2334–2342. Polymer Electrolyte Fuel Cell Model
171 R. Makharia, M.F. Mathias, D.R. Baker, J. Electrochem. Soc. 152 (5) A970–A977 (2005). Measurement of Catalyst Layer Electrolyte Resistance in PEFCs Using Electrochemical Impedance Spectroscopy
172 D.M. Bernardi, M.W. Verbrugge, J. Electrochem. Soc. 139 (1992) 2477–2491. A Mathematical Model of the Solid-Polymer-Electrolyte Fuel Cell
173 Manufacture's data sheet for ISEM-3 graphite by Svenska Tanso AB.
174 Manufacturer's Data Sheet for ®Sigracet GDL 10 BA by SGL Carbon AG.
175 W. Sun, B.A. Peppley, K. Karan, Electrochim. Acta 50 (2005) 3359–3374. An improved two-dimensional agglomerate cathode model to study the influence of catalyst layer structural parameters
176 T. Hottinen, O. Himanen, Electrochem. Commun. 9 (2007) 1047–1052. PEMFC temperature distribution caused by inhomogeneous compression of GDL
177 A. Jena, K. Gupta, J. Power Sources 96 (2001) 214–219. An Innovative technique for pore structure analysis of fuel cell and battery components using flow porometry
178 A. Jena, K. Gupta, CHARACTERIZATION OF THE PORE STRUCTURE OF COMPLETE FILTER CARTRIDGES USING HIGH FLOW POROMETRY
179 A. Jena, K. Gupta, Characterization of Porosity of Electrodes and Separators in Fuel Cell Industry
180 A. Gigova, J. Power Sources 158 (2006) 1054–1061. Investigation of the porous structure of battery separators using various porometric methods
181 W-k. Lee, J.W.V. Zee, Characterization of Permeability Changes and Hydrophobic Nature of GDL, and Correlation with PEMFC Performance, Fuel Cell Seminar, 2004
182 A.K. Jena, K.M. Gupta, J. Power Sources 80 (1999) 46–52. In-plane compression porometry of battery separators
183 A. Jena, K. Gupta, Effect of Cyclic Compression on Pore Structure of Battery Materials
184 T. Berning, D.M. Lu, N. Djilali, J. Power Sources 106 (2002) 284–294. Three-dimensional analysis of transport phenomena in a PEM fuel cell
185 H. Ju, H. Meng, C-Y. Wang, J. Heat Mass Transfer 48 (2005) 1303–1315. A single-phase, non-isothermal model for PEM fuel cells
186 H. Ichikawa, Japanese patent P2006–179236A written in Japanese

187 W.Q. Tao, C.H. Min, X.L. Liu, Y.L. He, B.H. Yin, W. Jiang, J. Power Sources 160 (2006) 359–373. Parameter sensitivity examination and discussion of PEM fuel cell simulation model validation Part I. Current status of modeling research and model development
188 C.H. Min, Y.L. He, X.L. Liu, B.H. Yin, W. Jiang, W.Q. Tao, J. Power Sources 160 (2006) 374–385. Parameter sensitivity examination and discussion of PEM fuel cell simulation model validation: Part II: Results of sensitivity analysis and validation of the model
189 A. Hakenjos, K. Tüber, J.O. Schumacher, C. Hebling, Fuel Cells 4 (3) (2004) 185–189. Characterising PEM Fuel Cell Performance Using a Current Distribution Measurement in Comparison with a CFD Model
190 H. Ju, C.Y.Wang, J. Electrochem. Soc. 151, A1954–A1960 (2004). Experimental Validation of a PEM Fuel Cell Model by Current Distribution Data
191 M. Acosta, C. Merten, G. Eigenberger, H. Class, R. Helmig, B. Thoben, H.M. Steinhagen, J. Power Sources 159 (2006) 1123–1141. Modeling non-isothermal two-phase multicomponent flow in the cathode of PEM fuel cells
192 R. Reissner, B. Thoben, T. Kaz, M. Schulze, E. G¨ulzow, Proceedings of the Eighth UECT, Ulm, Germany, June 20–21, 2002. Degradation of the hydrophobicity of fuel cell electrodes
193 P. Gode, F. Jaouen, G. Lindbergh, Anders Lundblad and Göran Sundholm, Electrochimica Acta 48 (2003) 4175–4187. Influence of the composition on the structure and electrochemical characteristics of the PEFC cathode
194 T. Murahashi, M. Naiki, E. Nishiyama, J. Power Sources 162 (2006) 1130–1136. Water transport in the proton exchange-membrane fuel cell: Comparison of model computation and measurements of effective drag
195 V. Mehta, J.S. Cooper, J. Power Sources 114 (2003) 32–53. Review and analysis of PEM fuel cell design and manufacturing

ISBN 978-951-22-9232-5
ISBN 978-951-22-9233-2 (PDF)
ISSN 1795-2239
ISSN 1795-4584 (PDF)